Imaging Ferromagnetism on the Micrometre Scale

A Scanning SQUID Microscopy Study

Master Thesis

Pim Reith

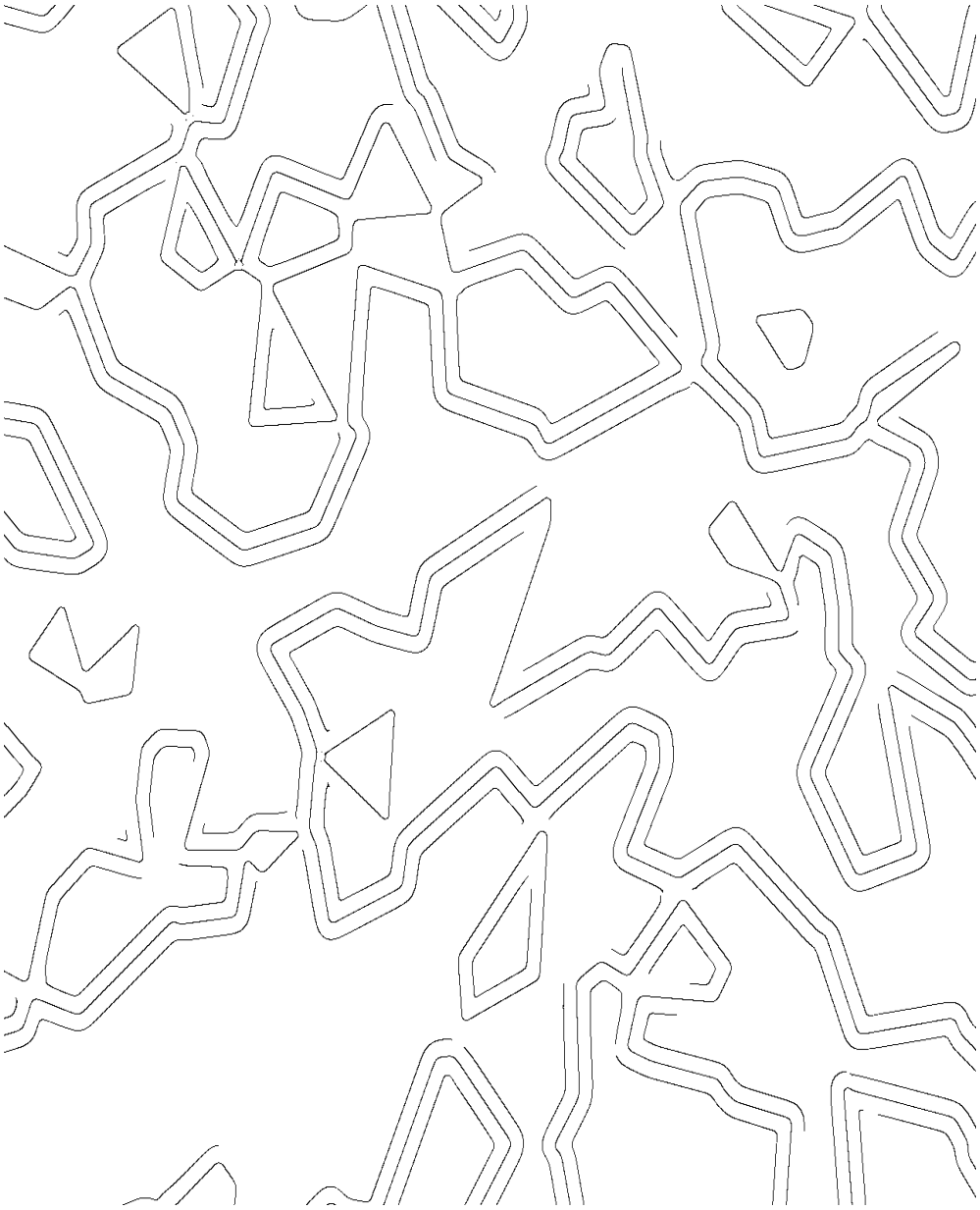

Interfaces and Correlated Electron Systems (ICE)
Supervisor: Prof. Dr. Ir. H. Hilgenkamp
Faculty of Science and Technology
University of Twente

April 17, 2015

Abstract

Superconducting quantum interference devices (SQUIDs) are currently the single most accurate magnetometers. Scanning SQUID microscopy (SSM) combines the field resolution of SQUIDs with scanning techniques from scanning probe microscopy to image magnetic flux on the surface of samples. This thesis describes experimental applications of SSM, as well as discussing the possibilities and limitations the technology has.

Part of this work is a discussion on the spatial resolution of SSM, looking at different factors affecting it and visualising these through simulations of different magnetic phenomena. This is supplemented by an analysis of deconvolution methods that can aid SSM by reversing the effects of the finitely-sized pickup loop.

In addition, SSM is applied to image the ferromagnetism on the surface of $LaMnO_3$ thin films deposited on $SrTiO_3$ substrates deposited at oxygen pressures between 10^{-7} and 10^{-1} Torr. We observe that with increasing oxygen deposition pressure leads to a monotonically increasing root-mean-square field value B_{RMS}. On the other hand, vibrating sample magnetometer measurements shows a local minimum in the magnetic moment at 10^{-4} Torr. This is explained as the anisotropy energy changing as a result of changing out-of-plane lattice parameter observed with X-ray diffraction, which causes the spins to align differently with increasing pressure. This can cause an increase in B_{RMS} even though the magnetic moment decreases, which is supported by simulations.

SSM was also used to study the influence of an Au-capping layer on $LaMnO_3$ thin films. We see that the Au-layer suppresses the ferromagnetic state, by imaging the border between a capped and an uncapped region. This is most likely due to damage done to the $LaMnO_3$ film during the Au sputtering process, though other scenarios are suggested.

Finally, we touch on some initial results from a collaboration between the University of Twente and the Paleomagnetic Laboratory of the Utrecht University. The goal is to develop a new way to measure geological rock samples to determine the magnitude and direction of Earth's magnetic field throughout history. This method will involve a combination of X-ray tomography, to determine the location of the magnetic grains in the samples, and SSM, to measure the field emanating from these samples. Combining these measurements should allow us to model the magnetic field that was present during the formation of the sample. From a first set of measurements on custom-made samples, we found that the measured field is at the upper limit of what our SSM setup can handle. Apart from that, the noise levels can possibly cause the model to not be able to fit the data properly. Some solutions for this are discussed.

Contents

1. Introduction

Discovered just over 100 years ago by Kamerlingh Onnes in Leiden, superconductivity has since found applications in many areas of technology. Superconductors can be found in Nuclear Magnetic Resonance (NMR) and Magnetic Resonance Imaging (MRI), which have made large impacts in chemistry and medicine respectively; in confinement magnets in nuclear fusion reactors and particle accelerators; even in maglev trains and military applications such as railguns.

One such application is a Superconducting QUantum Interference Device, or SQUID. SQUIDs are the single most accurate measuring instruments for magnetic fields, the most accurate ones being able to measure fields on the order of attotesla (aT, 10^{-18} T) [1]. Because of this, SQUIDs, too, have found their way into vastly different fields of science [2, 3]: Astronomy, as part of the gyroscopic setup in spacecraft used to measure effects of general relativity [1], or aiding in the search for the components of dark matter [4, 5]; particle physics, where it was used to measure the dynamic Casimir effect for the first time [6], and looking for magnetic monopoles [7] and free quarks [8]; even biology, where it can measure the tiny magnetic fields produced by various processes in an organism [9].

In the experiments described in this thesis, SQUIDs were used to image the magnetism at the surface of various samples. To do this, a SQUID sensor is scanned across the surface, measuring the magnetic flux at each point. This technique is called Scanning SQUID Microscopy (SSM). The basic theory and operational aspects of SSM are laid out in Chapter 2.

Chapter 4 is a discussion on the imaging and spatial resolution of the SSM. Using simulations of different magnetic phenomena, we will analyse how they appear when imaged with SSM and how spatial resolution affects the information we can obtain from experiments. We will also have a look at deconvolution methods, which can be used to reverse the effect of field averaging due to the finite size of the sensor.

The main experimental project in this thesis is the imaging of ferromagnetism on the surface of $LaMnO_3$ (LMO) thin films deposited under various growth conditions. This was done to get a better understanding of the origin of ferromagnetism (and antiferromagnetism) in LMO thin films, and the influence of various factors (such as vacancies or strain) thereon. This is a continuation of a series of experiments that discovered an atomically sharp transition from antiferromagnetic to ferromagnetic ordering in LMO thin films on STO substrates [10]. A background on LMO is given in Chapter 3, while experimental details of the analysis of the thin films is presented in Chapters 5 and 6. Chapter 5 focuses on a series of samples deposited at different oxygen pressures. Chapter 6 presents results obtained from experiments with Au-capped LMO thin films.

Chapter 7 describes a collaboration set up between ICE and the Paleomagnetic Laboratory of the Utrecht University. This collaboration focuses on developing a new method of measuring the magnetic field throughout Earth's history by analysing samples obtained from lava deposits. Older methods are unreliable and destructive measurements [11, 12], so a more reliable, non-destructive measuring method is highly desired.

2. Scanning SQUID Microscopy - Theoretical Background

A variant of Scanning Probe Microscopy (SPM), Scanning SQUID Microscopy (SSM) is used to image magnetic flux emanating from the surface of a sample. Since their invention in 1964 by Jaklevic *et al.*, SQUIDs have become the most sensitive way of measuring magnetic field strength, with the ability to measure magnetic fields as low as 5 aT ($5 * 10^{-18}$ T) [1, 13]. This chapter will outline the most important equations and concepts to understand SSM and how SSM operates in an experimental setup.

2.1 Josephson Junctions

The SQUID that forms the integral part of the SSM sensor is made out of one or more so-called Josephson junctions. Josephson junctions were predicted in 1962 when Brian Josephson investigated superconductivity across so-called weak links. A weak link is formed when two superconductors are separated by a thin barrier of non-superconducting material (e.g., an insulator or a normal metal, as shown in Figure 2.1), or even if a section of the superconductor has a smaller physical size. Prior to this, experimenters had observed a supercurrent through these weak links, but attributed them to shorts in the barrier [14, 15].

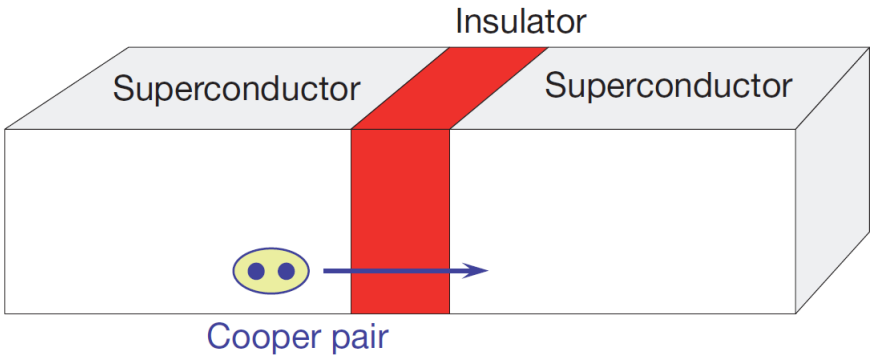

Figure 2.1: A weak link between two superconductors formed by an insulator. According to Josephson, Cooper pairs can tunnel through these barriers [16].

According to Josephson's theory, Cooper pairs can tunnel across non-superconducting barriers, much like normal electrons can tunnel across thin insulating barriers following the laws of quantum mechanics. Josephson derived two equations to describe the current I and voltage V as functions of the time t for these junctions:

$$I(t) = I_c sin(\varphi_j(t)), \tag{2.1}$$

$$V(t) = \frac{\hbar}{2e}\frac{d\varphi_j}{dt}, \tag{2.2}$$

where φ_j is the difference between the phases of the superconducting order parameters

of each side of the barrier (or phase drop), $\hbar = h/(2\pi)$ is the reduced Planck's constant, e is the electron charge and I_c is the critical current of the system.

Equation 2.1 show that a supercurrent, which is a function of the phase difference, can flow through such a system (known nowadays as Josephson junctions) at zero voltage. This is known as the dc Josephson effect. When a fixed voltage is applied across the junction, Equation 2.2 shows that the phase will increase linearly with time. When put into the first equation, one sees that this will cause the current to oscillate with time, at a frequency $\omega = 2e/\hbar * V$. This is known as the ac Josephson effect.

The experimental validation of Josephson's theory came in 1963 by Anderson and Rowell [17]. In 1973, Josephson received the Nobel Prize in Physics for his work.

2.2 Flux quantisation and fluxoid quantisation

When a magnetic field passes through a superconducting ring, one can show that the magnetic flux is quantised. To prove this, we start with the relationship between the phase φ of the superconducting order parameter $\Psi = |\Psi| e^{i\varphi}$, the supercurrent density J_s and the magnetic vector potential A:

$$\nabla\varphi = 2\pi \left[\frac{2m}{hn_s e} J_s + \frac{2e}{h} A \right], \tag{2.3}$$

where m is the electron mass (and, therefore, $2m$ the mass of a Cooper pair), n_s the density of superconducting electrons and h is Planck's constant. Since the order parameter must be single-valued everywhere, integrating this equation along a closed loop must lead to a phase difference equal to an integer multiple of 2π:

$$\Delta\varphi = \frac{4\pi e}{h} \left[\frac{m}{n_s e^2} \oint J_s \cdot dl + \oint A \cdot dl \right] = n \cdot 2\pi, \tag{2.4}$$

where n is an integer. If we take this closed loop deep enough in the superconductor (i.e., more than the London penetration depth λ away from the edges), J_s will be zero everywhere along the loop. Furthermore, since $\nabla \times A = B$ (where B is the magnetic field), we can apply Stokes theorem and obtain

$$n \cdot 2\pi = \frac{4\pi e}{h} \int B da. \tag{2.5}$$

Rearranging this, and noting that $\int B da$ equals the magnetic flux Φ, we end up with the flux quantisation condition:

$$\Phi = n \cdot \frac{h}{2e}. \tag{2.6}$$

In other words, the flux through a superconducting ring is quantised in units of $\Phi_0 = h/2e = 2.0 * 10^{-15}$ Wb. These units are known as flux quanta. Proposed by London in 1948 [18], flux quantisation was first observed experimentally independently by Doll and Näbauer [19] and by Deaver and Fairbank [20] in 1961. The above derivation is based on the derivation of flux quantisation found in [21].

Now, if we add one or more Josephson junctions to a superconducting ring, however, we have to adjust our equations slightly to include the phase drop across each junction.

If we have a ring with N Josephson junctions, each with a phase drop $\varphi_{j,i}$, Equation 2.4 becomes

$$\frac{4\pi e}{h}\left[\frac{m}{n_s e^2}\oint J_s \cdot dl + \oint A \cdot dl\right] + \sum_{i=1}^{N} \varphi_{j,i} = n \cdot 2\pi. \tag{2.7}$$

The term on the left-hand side is known as a 'fluxoid'. As before, we can set J_s to zero if we are deep enough in the superconductor, leading to

$$\frac{1}{2\pi}\sum_{i=1}^{N} \varphi_{j,i} + \frac{\Phi}{\Phi_0} = n. \tag{2.8}$$

We can see that now, with Josephson junctions, it is not the flux that is quantised, but the sum of the flux (normalised to Φ_0) and the total phase drop across all Josephson junctions is quantised: fluxoid quantisation.

2.3 RCSJ model

To analyse the voltage state of a Josephson junction, it is typically modelled as being connected in parallel to a resistor (with resistance R) and a capacitor (with capacitance C), as shown in Figure 2.2a. This model is known as the Resistively and Capacitively Shunted Junction (RCSJ) model. The model was first set up independently by Stewart [22] and McCumber [23] in 1968, and experimentally verified 3 years later by Hansma, Rochlin and Sweet [24].

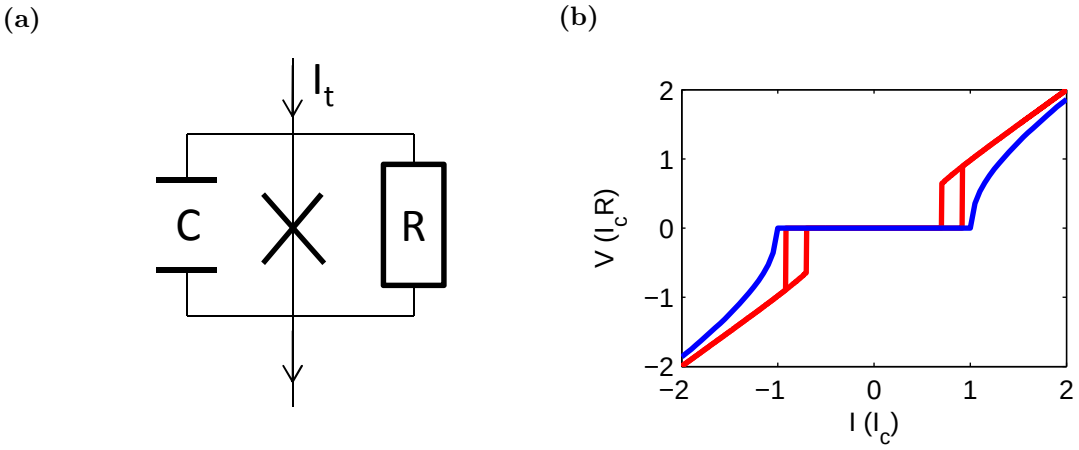

Figure 2.2: a) A Josephson junction (indicated by the cross) connected in parallel with a resistor and a capacitor. b) $I-V$ characteristics of a Josephson junction with $\beta_c = 0.5$ (blue) and $\beta_c = 5$ (red).

We can apply Kirchoff's law to this model to describe the current I_t through the junction:

$$I_t = C\frac{dV}{dt} + I_c sin(\varphi_j) + \frac{V}{R}. \tag{2.9}$$

If we put in Equation 2.2 and rearrange the terms, we obtain

$$0 = \frac{\partial^2 \varphi_j}{\partial t^2} + \frac{1}{RC}\frac{\partial \varphi_j}{\partial t} + \frac{2\pi}{C}\frac{I_c}{\Phi_0}\left[sin(\varphi_j) - \frac{I_t}{I_c}\right]. \tag{2.10}$$

We can define a parameter β_c, known today as the Stewart-McCumber parameter:

$$\beta_c = \frac{2\pi}{\Phi_0} I_c R^2 C. \tag{2.11}$$

Using this parameter, and defining

$$i = \frac{I_t}{I_c} \tag{2.12}$$

$$\tau = \frac{2\pi}{\Phi_0} I_c R t, \tag{2.13}$$

we can rewrite Equation 2.10 as follows:

$$i = \beta_c \frac{d^2\varphi}{d\tau^2} + \frac{d\varphi}{d\tau} + sin(\varphi_j). \tag{2.14}$$

By solving this equation numerically, we can see the influence of β_c on the system: for values $\beta_c < 1$, the system has no hysteresis (overdamped), and for values $\beta_c > 1$, hysteresis will appear (underdamped), as shown in Figure 2.2b. Although the division between over- and underdamped in literature is usually made at $\beta_c = 1$, the actual value is around 0.756 [25]. For most practical applications (like SSM), having non-hysteretic behaviour is of course preferable, to ensure a one-on-one relation between I and V.

2.4 dc SQUIDs

A direct current Superconducting QUantum Interference Device (dc SQUID) is a device that consists of two parallel Josephson junctions in a circular structure. Typically, a supercurrent bias I_b is applied to this structure during an experiment. Figure 2.3 shows a schematic representation of a dc SQUID.

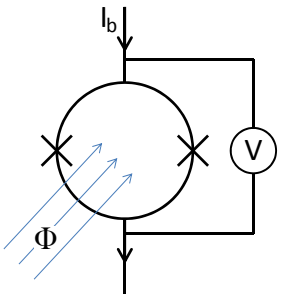

Figure 2.3: Schematic overview of a dc SQUID.

2.4.1 dc SQUID in the superconducting state

Assuming the two junctions are symmetric (i.e., have the same properties) and the SQUID is in the superconducting state, then the total current through the junction becomes

$$I = I_c \left[sin(\varphi_{j1}) + sin(\varphi_{j2}) \right]. \tag{2.15}$$

The fluxoid quantisation condition from Equation 2.8, bearing in mind the direction of the current, turns into

$$\frac{1}{2\pi}(\varphi_{j1} - \varphi_{j2}) + \frac{\Phi_t}{\Phi_0} = n, \tag{2.16}$$

where Φ_t is the total flux threading the SQUID. Combining the above two equations gives us the critical current I_{ct} of a dc SQUID:

$$I_{ct} = 2I_c \left| cos\left(\pi \frac{\Phi_t}{\Phi_0}\right)\right|. \tag{2.17}$$

Now, Φ_t is the total flux through the SQUID, which is the sum of the external flux Φ and the flux generated by the SQUID itself due to screening currents:

$$\Phi_t = \Phi + I_c L[sin(\varphi_{j1}) - sin(\varphi_{j2})]. \tag{2.18}$$

The influence of the screening current and the resulting flux can be described by the screening parameter:

$$\beta_L = \frac{2LI_c}{\Phi_0}, \tag{2.19}$$

where L is the inductance of the dc SQUID. The lower β_L, the less the external flux is screened. Figure 2.4a shows how the relation between I_{ct} and Φ changes depending on β_L. Figure 2.4b shows the relation between Φ_t and Φ for different β_L.

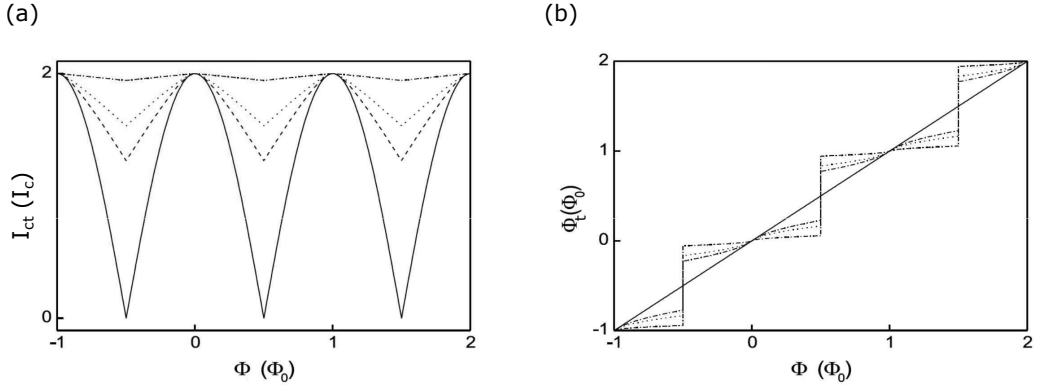

Figure 2.4: a) Total critical current of a dc SQUID as a function of external flux through the loop. b) Total magnetic flux through a dc SQUID as a function of the external flux. Solid lines correspond to $\beta_L = 0$, dashed lines to $\beta_L = 5$, dotted lines to $\beta_L = 10$ and dash-dotted lines to $\beta_L = 100$. Adapted from [26].

Figure 2.4 shows that with increasing β_L, a SQUID will behave more and more as a regular superconducting ring. When an external flux is applied, the SQUID creates an opposing flux to bring the total flux back down to 0. If the external flux becomes larger than $\Phi_0/2$, however, it becomes energetically favourable to instead create a flux in the same direction to bring the total flux up to 1 Φ_0. The dc SQUID has an optimal energy sensitivity at $\beta_L \approx 1$ [2].

One can use a superconducting dc SQUID to measure magnetic flux by measuring the critical current, which involves increasing the current until it passes I_{ct} and the voltage state appears, at every measurement point. However, there is an easier method.

2.4.2 dc SQUID in the voltage state

A dc SQUID biased at a certain I_b just above the critical current will have a sinusoidal flux-voltage relation with a period of Φ_0 (see Figure 2.5). This means the voltage output of the SQUID will oscillate between some minimum value V_1 (at $n\Phi_0$) and some maximum value V_2 (at $(n + 1/2)\Phi_0$), regardless of the actual amount of flux. For small flux changes, a dc SQUID can be operated by biasing the system to a working point W at the steepest part of the flux-voltage relation (i.e., where $F = \partial V/\partial\Phi$ is largest). Around this point, a small change in flux will create a proportional change in voltage. However, this linearity is only valid for a small range of flux values $\Phi_{lin} \lesssim \Phi_0/\pi$ [2].

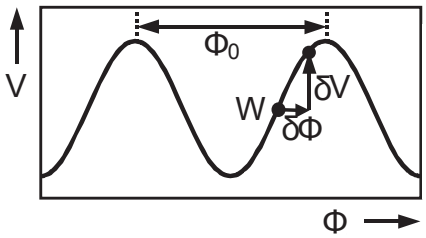

Figure 2.5: Flux-Voltage ($\Phi - V$) relation of a dc SQUID biased just above the critical current. Around working point W, a small change $\delta\Phi$ will lead to a proportional change δV. Adapted from [2].

To solve this, we can apply a bias flux Φ_B to bias the system to W. A feedback circuit is set up by feeding the output to a feedback resistance R_f and a feedback coil coupled to the SQUID through a mutual inductance M_f. Then, when the flux through the SQUID changes by an amount $\Delta\Phi$, the feedback coil will create a feedback flux Φ_f in the SQUID in such a way that $\Phi_f = -\Delta\Phi$. This causes the total flux in the loop to become locked to the value corresponding to W: a Flux-Locked Loop (FLL). This keeps the SQUID at maximum sensitivity. At the same time, the voltage across R_f, which is a measure of Φ_f and therefore total flux, gives the output signal V_L. Futhermore, the measurable range can be extended to $10^4 - 10^5$ Φ_0 by adding a digital component to the feedback circuit, which can 'reset' Φ_f to 0 when it exceeds an integer number of Φ_0 (since the output voltage is periodic in Φ_0), and adding the number of flux quanta reset this way to the signal digitally [27].

A more advanced FLL method involves applying a small flux modulation $\Phi_m(\omega) = |\Phi_m| sin(\omega t)$ to a dc feedback flux signal. In Figure 2.6, three different working points are shown at points A, B and C. When the modulation is applied, the three points will show different voltage outputs V_S. At points A and C, the signal will show an oscillation at frequency ω, but with the amplitude opposite in sign. Yet, at point B, the signal will oscillate at a frequency 2ω.

This can then be used to create an FLL. The SQUID is biased to a flux value of $n\Phi_0/2$, one of the extrema in the flux-voltage relation. Then a modulating flux signal $\Phi_m(\omega)$ with frequency ω is applied. When the sensor picks up a flux of $n\Phi_0/2$, the output signal will only contain a component at 2ω. However, any other amount of flux will create an output with a component at ω. Using a lock-in amplifier, the amplitude of this component (V_L) is fed back into the modulation signal to bring the system back to $n\Phi_0/2$. At the same time, V_L is a measure for the flux through the sensor (using calibration data obtained by applying a known field).

The FLL allows an SSM setup to measure a large flux range as opposed to the small linear range without an FLL. Yet at the same time the FLL enables the SSM to measure flux changes only a fraction of a flux quantum, and the electronics needed for an FLL add only very little noise to the system [2].

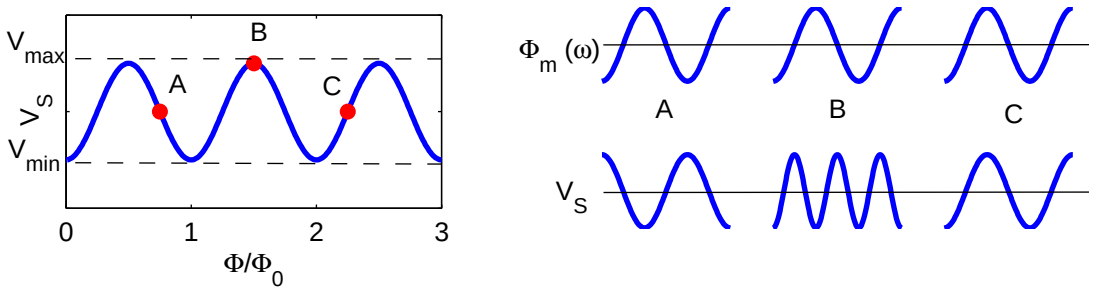

Figure 2.6: Output voltage as a function of a flux modulation $\Phi_m(\omega)$ at three different working points A, B and C. The output at B has a frequency of 2ω compared to A and C, where it has a frequency of ω.

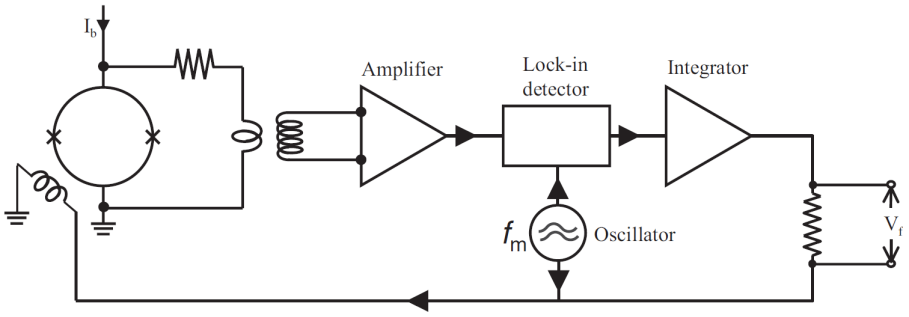

Figure 2.7: Simplified schematic of a Flux-locked loop operating at a modulation frequency f_m [2].

V_L is amplified and then converted to a digital signal using an AD-converter to be used by a computer. To convert V_L into a flux Φ or a magnetic field B, we use the following formula:

$$\Phi = B * A_p = \frac{1}{F * G} \frac{A_p}{A_e} * V_L \tag{2.20}$$

In this equation, F is the flux-to-voltage ratio (sometimes written as $\partial V/\partial \Phi$), a characteristic of the FLL. G is the gain applied to the voltage signal before conversion into a digital signal. Finally, A_p is the area of one 'pixel' on the sample (defined as the resolution squared), and A_e is the effective area of the pickup loop after considering the angle and effects such as flux focusing (see Chapter 4).

In most SSM sensors, the circuitry shown in Figure 2.3 is extended with a pickup loop (see Figure 2.8). The loop is made out of superconducting material, and serves as a predefined area through which magnetic flux can penetrate while the remaining elements of the SQUID are magnetically shielded. This is done to prevent stray magnetic fields from influencing the measurements as much as possible.

In some setups, instead of having the pickup loop connected directly to the SQUID as in Figure 2.8, an intermediate pickup coil is used, coupled inductively to the SQUID using a secondary coil (see Figure 2.9a) [28]. This can be done when the object or field of interest is too large to measure with the above method.

Apart from a magnetometer, dc SQUIDs can also be used as a first and second derivatie axial ($\partial B/\partial z$ and $\partial^2 B/\partial z^2$ respectively) gradiometer (see Figure 2.9b-c). Another option is a first derivative planar ($\partial B/\partial x$) gradiometer (Figure 2.9d).

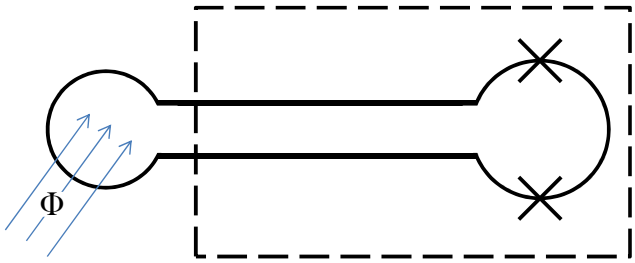

Figure 2.8: Schematic representation of a dc SQUID extended with a pickup loop. The dashed area is magnetically shielded.

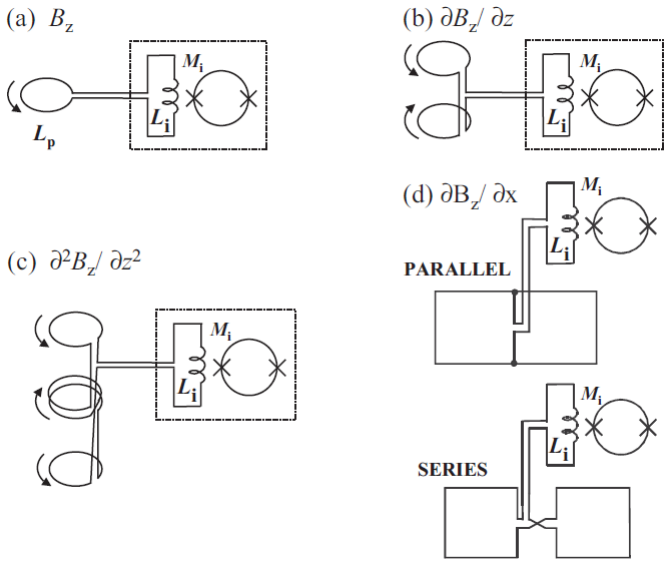

Figure 2.9: Four different SQUID based measurement setups: a) magnetometer, b) first derivative axial gradiometer, c) second derivative axial gradiometer, d) parallel and serial first derivative planar gradiometer [2].

2.5 Scanning SQUID Microscopy

In Scanning SQUID Microscopy, the sensor is brought into close proximity of the sample surface, and is then scanned across it to measure the signal. The pickup loop, with diameter d_0 (radius r_0), has a distance z above the sample and 2-dimensional scans are made in the x and y-directions (see Figure 2.10).

In our setup, SSM measurements are done with both sample and sensor in a cryostat cooled to liquid He temperatures (4.2 K) to ensure the sensor is in the superconducting state. The sensor remains stationary while the sample is moved in the three spatial directions by means of a lever, with the sample at one end and three motors (one for each of x, y and z) at the other, outside the cryostat. A lever is used for motion instead of piezoelectric actuators due to the limited range of motion of the latter under cryogenic circumstances ($\sim$ 100 μm) [29, 30].

The sensor is mounted on a cantilever, which flexes to reduce damage to the sensor and/or the sample in case of physical contact between the two (for example, during approach). Due to the wires connecting the sensor to the cantilever, the sensor is placed at a small angle with respect to the sample to prevent damage to these wires. This angle is approximately 10° (see Figure 2.10). This changes the effective area of the pickup

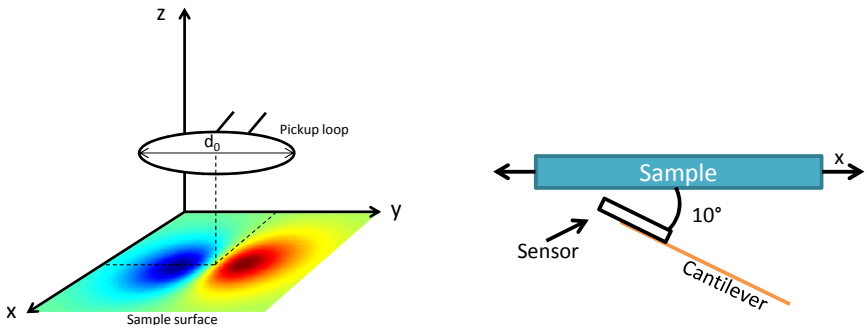

Figure 2.10: Geometry of the sensor and sample surface.

loop, which is accounted for during data processing.The effective area of the pickup loop of our sensors is approximately 21 μm^2, which also includes effects such as flux focusing. The physical diameter of the pickup loop is 3 μm.

During a measurement, the tip of the sensor is brought into contact with the sample surface. This means the centre of the pickup loop is roughly 2 μm away from the surface. Since the cantilever is flexible, pushing the sensor against the sample will slightly change the contact angle.

Figure 2.11 shows a schematic representation of a line scan. Field lines coming out of the surface will yield a positive output signal, field lines going into the surface a negative signal. Normally, the sensor would only be sensitive to magnetic flux in the z-direction, but since it is under a small angle, some flux in the x and y-directions will be measured as well.

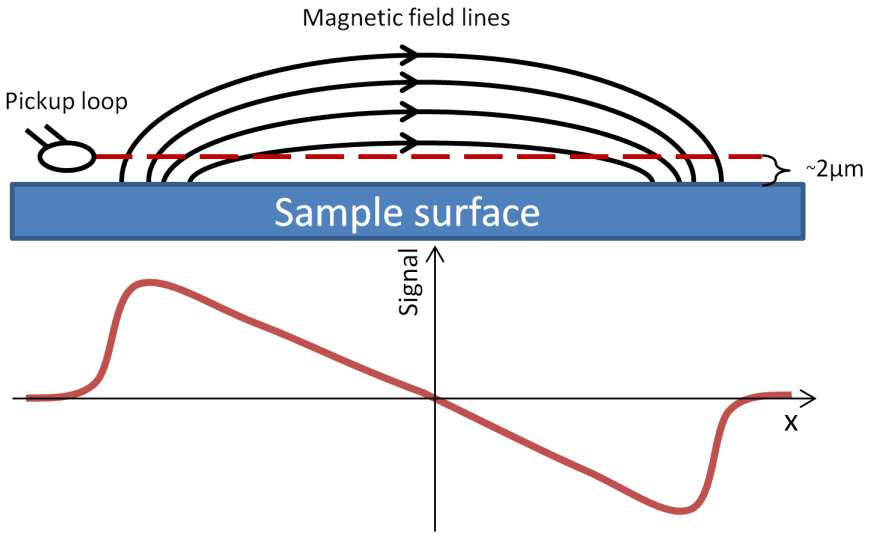

Figure 2.11: Schematic representation of the output signal as a result of a line scan.

2.6 Noise in the SSM

As with all measurements in physics, SSM measurements will have some noise contribution. Due to the high sensitivity of the SQUID, external noise sources can have a large impact on the signal. Things such as passing cars or telecommunication signals (telephones, radio, wifi, etc.) produce noticeable output signals from the SQUID. Acoustic vibrations (e.g., from a nearby vacuum pump or construction work) also lead to noise by causing the sensor to move in the ambient field. The electronics that handle the signal between the SQUID and the computer also contribute to the noise, such as the 50 Hz ac-power from the mains.

In SQUID literature, noise spectral densities are often calculated as flux noise spectral densities S_Φ:

$$S_\Phi = \frac{S_V}{F^2}, \tag{2.21}$$

where S_V is the voltage noise spectral density, and F the flux-to-voltage conversion factor (the same as in Eqn. 2.20). This number is usually displayed as $\sqrt{S_\Phi}$ in units of $\mu\Phi_0/\sqrt{\text{Hz}}$.

The typical noise spectrum of a SQUID consists of two parts: a region of $1/f$ noise ('pink' or 'flicker' noise) below roughly 1-10 Hz, and white noise above that [2]. As mentioned, various internal and external sources can affect the amount of noise in the system. This section will only discuss noise sources intrinsic to the SQUID.

Just as any resistor at finite temperature, the SQUID will produce thermal noise (also known as Johnson-Nyquist noise), described by

$$S_V = 4k_BTR, \tag{2.22}$$

where k_B is the Boltzmann constant, and T is the temperature of the resistor R [31]. For a low-temperature SQUID, this leads to a flux noise on the order of 1 $\mu\Phi_0/\sqrt{\text{Hz}}$ [32], which is approximately constant across the whole spectrum. Thermal noise acts as a lower bound to the sensitivity, being a fundamental source of noise. As we can see in Figure 2.12, the white noise level is higher than what thermal noise would produce. Most of this is due to external sources [2].

The 1/f part of the noise spectrum is much less understood [2], though understanding 1/f noise in SQUIDs is not only important for improving SSM capabilities, it is also important for other systems based on Josephson junctions, such as varying types of qubits in quantum computing [33,34]. Several mechanisms have been identified that contribute to the noise in a 1/f-fashion, one of which is due to trapped states in the Josephson junction. Defects in the junction can trap electrons, which alters the tunneling barrier height. This, in turn, changes the critical current through the Josephson junction. The trapping and releasing of electrons is a thermally activated process, resulting in noise described by

$$S(f,T) \propto \frac{k_BT}{f} D_T(E), \tag{2.23}$$

where $D_T(E)$ is the distribution of activation energies of trapping sites [35,36].

A second mechanism has to do with trapped vortices in the body of the SQUID or the superconducting circuit connected to it. If enough thermal energy is available, these trapped vortices can move between pinning sites, changing the stray flux that the

SQUID detects. In the same way as for trapped electrons, one can show that the noise due to vortex motion behaves as

$$S(f,T) \propto \frac{k_B T}{f} D_P(E), \tag{2.24}$$

where $D_P(E)$ is the distribution of activation energies, but now for the pinning sites [35–37]. However, noise due to moving vortices is more apparent in high-T_c SQUIDs compared to low-T_c SQUIDs, due to the higher thermal energy and lower pinning energies [33].

More recently, fluctuating spins of electrons trapped in defect states are also believed to be contributing to 1/f noise [33,38]. These electrons are mostly located at the interface between the SQUID and an insulator (e.g., the substrate or an oxide layer on the SQUID surface) [39].

Various methods exist to suppress the different sources of noise, such as active or passive magnetic shielding or different readout schemes. Some methods are discussed in Ref. [2]. For our own setup, we have an optional Nb shield which surrounds the sample and the sensor. Since Nb becomes superconducting in the cryostat, the shield will repel nearly all of the external influences. A comparison of the noise spectra with and without shield can be seen in Figure 2.12. The figure also clearly shows the high-pass filter (cutoff frequency of 5 kHz) built into the system to reduce high-frequency noise. The disadvantage of the filter, however, is that it limits scanning speeds. Without the shield, the noise is roughly 14 $\mu\Phi_0/\mathrm{Hz}^{1/2}$, or a field error of $\pm$ 40 nT. With the shield, this becomes about 3 $\mu\Phi_0/\mathrm{Hz}^{1/2}$, or 9 nT.

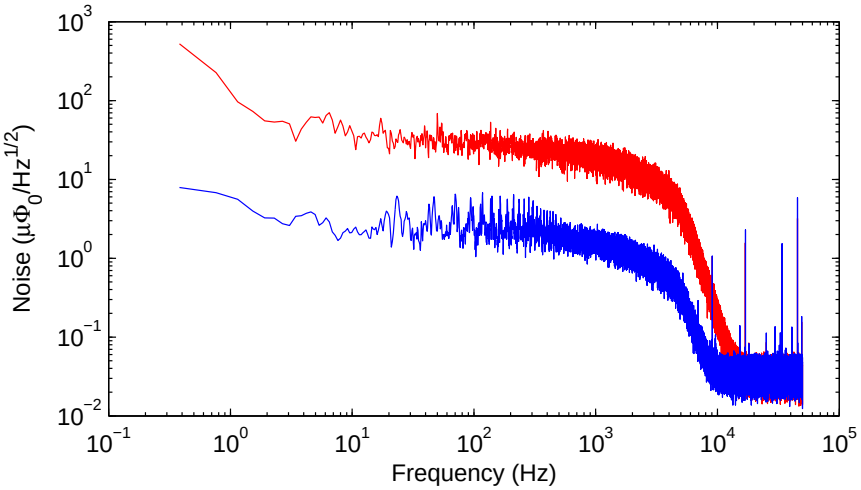

Figure 2.12: Comparison of the noise spectra with (blue) and without Nb shield

Another simple way to reduce noise is to make multiple scans, and then taking the average. This requires no changes to the setup or scanning method. By averaging over N measurements, the signal-to-noise ratio will increase as $\sqrt{N}$. Doing this, however, will require that both the setup and the sample itself are stable. The setup should be stable to guarantee that each point of a certain measurement corresponds to the same point in all other measurements (i.e., the sample and sensor have not moved with respect to one another). The sample itself should also be stable in the sense that its magnetic features should not change in time, or at least on a time scale far longer than the time required to do the measurements.

3. Introduction to $LaMnO_3$

In this chapter we will look at some properties of $LaMnO_3$ (LMO) that will be important to understand for the experiments. We will go into the structure of LMO, discuss factors such as doping and strain, and discuss how these influence the magnetic properties of LMO, in which we are ultimately interested.

3.1 Perovskites

Perovskites are a class of materials with the general chemical composition ABO_3, where A and B are cations. An ideal perovskite has a cubic crystal structure, as can be seen in Figure 3.1. In the crystal structure, the A cations sit at the corners of the cube, the smaller B cations sit in the centre, and the O anions sit in the centre of the faces of the cube, forming an octahedron around the B cation.

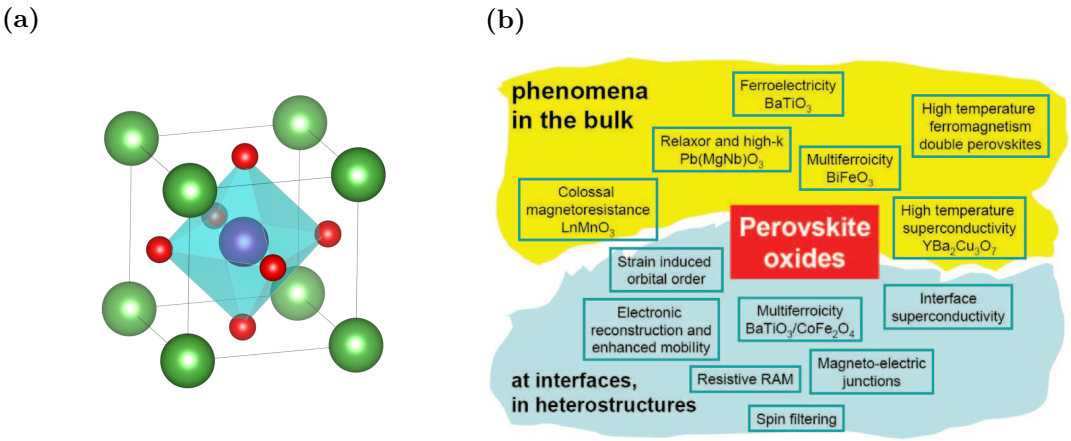

Figure 3.1: a) A single unit cell of the perovskite crystal structure ABO_3, with A in green, B in purple and O in red. The oxygen octahedron is highlighted in blue. b) Various properties of bulk and thin film perovskites with some example compounds [40].

Perovskites are an interesting group of materials due to the various unusual properties they possess, such as (high temperature) superconductivity, colossal magnetoresistance, ferroelectricity and charge ordering [40–43]. Furthermore, since most perovskites have very similar lattice parameters, heterostructures with low strain values can be created. At the interface, various phenomena arise due to an interplay of doping, charge transfer and structural changes. The most famous example is probably the creation of a 2-dimensional electron gas at the interface of two insulators: $LaAlO_3$ and $SrTiO_3$. A collection of bulk and interface properties is shown in Figure 3.1b.

3.2 The structure of LMO

LMO is such a perovskite, with a bulk lattice parameter of 3.94 Å [44]. The crystal structure of LMO deviates from the ideal cubic perovskite structure due to distorted O-octahedra, as shown in Figure 3.2a [45]. This distortion is a result of the Jahn-Teller effect [46].

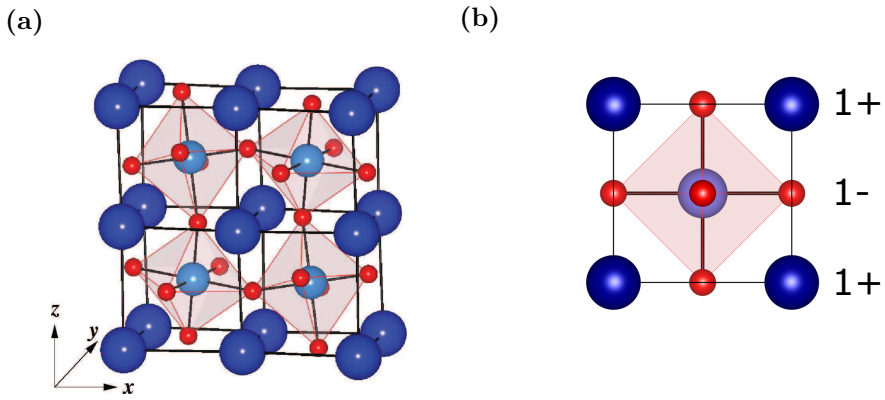

Figure 3.2: a) Schematic representation of the distorted structure of $LaMnO_3$ due to the Jahn-Teller effect [47]. b) Net charge of different planes of LMO: LaO has 1+, MnO_2 has 1-.

To understand the Jahn-Teller effect, we have to look at the electron configuration of Mn. In LMO, Mn ions have a charge of 3+, meaning they have 4 electrons occupying the 3d orbital. Due to the O ions surrounding the Mn ion, the d-levels split up, as shown in Figure 3.3. The $3d_{xz}$, $3d_{yz}$ and $3d_{xy}$ levels have their energy lowered, whereas the $3d_{3z^2-r^2}$ and $3d_{x^2-y^2}$ are raised in energy. The former three are collectively named the t_{2g} states, the latter are the e_g states. The total separation in energy between these two levels is Δ_0. To ensure energy conservation, the t_{2g} states are lowered by $\frac{2}{5}\Delta_0$, and the e_g states are raised by $\frac{3}{5}\Delta_0$, so that the total energy change amounts to 0.

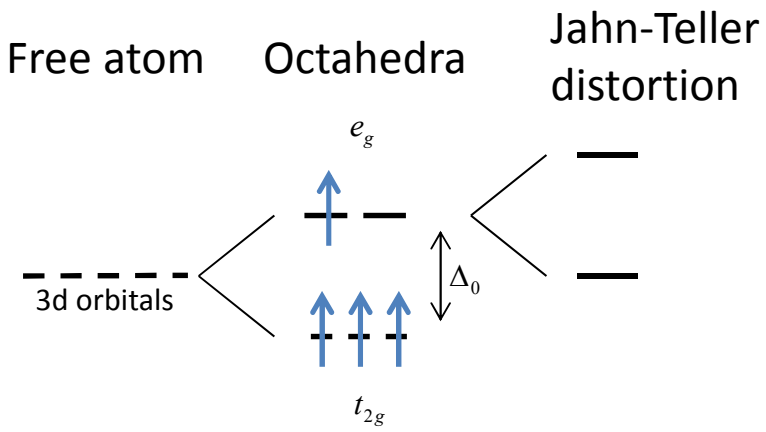

Figure 3.3: Splitting of the d-levels due to the MnO_6 octahedra and the Jahn-Teller effect. The blue arrows indicate the location of the electrons in LMO.

The Jahn-Teller effect attempts to lift the degeneracy of the e_g states by alternatingly lengthening and shortening Mn-O bonds in the ab-plane of LMO [48–50], which leads to the distorted structure visible in Figure 3.2a. The longer Mn-O bonds are 0.218 nm, the shorter ones are 0.191 nm; in the c-direction the Mn-O bond length is 0.196 nm [49]. These changes in bond lengths are accompanied by a tilt and rotation of the octahedra, leading to a orthorhombal structure instead of the ideal cubic perovskite crystal structure [48, 50]. Through the Jahn-Teller effect, the electronic properties are coupled to the physical dimensions of the LMO structure. Therefore, one can expect deformations due to strain, thermal expansion, etc. to influence these electronic properties [51].

In LMO, both the Mn and La ions have a charge of 3+, whereas the O ion has a charge of 2-. When viewing LMO along one of the crystal axes, we can see that there are

planes of alternating net charge in the structure, as shown in Figure 3.2b. The MnO_2 planes have a net charge of 1-, whereas the LaO planes have a net charge of 1+. This makes LMO a polar material. To compare, take a look at $SrTiO_3$ (STO): there the TiO_2 and SrO planes both have 0 net charge, making it non-polar.

Following Hund's rules, Mn^{3+} will have 1 electron in each of the t_{2g} states, and 1 electron in one of the e_g states, with all 4 having the same spin (either all up or all down), as shown in Figure 3.3. This becomes relevant when we look at the magnetic ordering in LMO, which is determined by the Mn electrons.

LMO is a Mott-insulator. Mott-insulators are a class of materials that, according to their band-structure should be a metal, but show insulating behaviour. This is due to strong on-site electron-electron repulsion, which means that electrons cannot move from one lattice site to another without overcoming a significant energy barrier resulting from Coulomb-interactions between the moving electron and the electron at that lattice site.

3.3 Magnetic ordering in LMO

Some materials can show spontaneous magnetic order even in the absence of an external magnetic field. This is due to exchange interactions aligning the spins of unpaired electrons in an atom. The electrons can be aligned in different ways. They can all point in the same direction, giving the material a bulk non-zero magnetisation, known as ferromagnetism (FM). If the spins are aligned antiparallel to one another, the material will have no bulk magnetisation, which is known as antiferromagnetism (AF). AF can be divided into subclasses based on along which planes the spins are aligned parallel and antiparallel (see Figure 3.4). Further distinctions can be made, depending on exactly which orbitals are occupied and interacting [52].

A third type is when spins are aligned antiparallel, but the magnitude of the magnetic moments in both directions is unequal, leading to a small net magnetisation. This is known as ferrimagnetism.

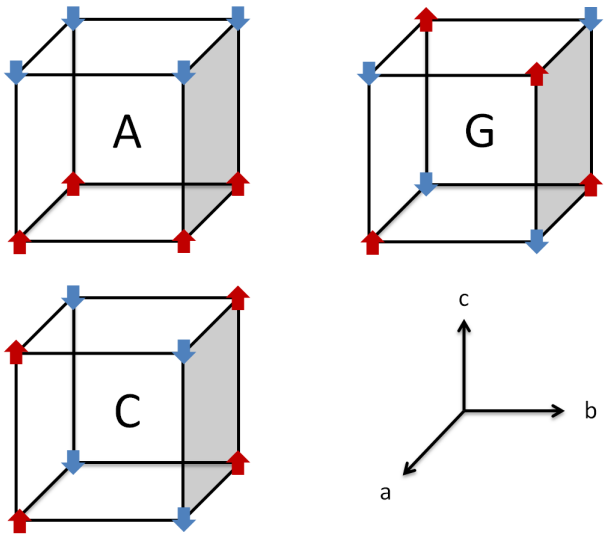

Figure 3.4: Three types of antiferromagnetic ordering: A-type, C-type and G-type. Note that the arrows indicate the Mn-ions, which have a net spin.

The following sections will explain different magnetic couplings and how they apply to the LMO system.

3.3.1 Direct Exchange and RKKY-interaction

Direct exchange is a result of the overlap of electronic wave functions of neighbouring atoms and the electrostatic energy between them. Because of Pauli's principle, the wave functions of two electrons must be antisymmetric if their spins are equal, and vice versa. On average, the distance between two electrons is larger in the antisymmetric case. Thus, by aligning the spins, the electrostatic energy of the two electrons is lowered, which is favourable. This means that direct exchange leads to ferromagnetic ordering.

Direct exchange, however, only appears if neighbouring atoms are close enough together that the electronic wave functions overlap. For more localised electrons (such as d and f-electrons), or when the atoms are spaced apart enough or are separated by other atoms, the wave functions do not overlap (enough) to create a significant electrostatic energy difference between symmetric and antisymmetric wave functions, as is the case in LMO. Therefore, direct exchange will not lead to spin alignment in LMO, where the Mn-ions are separated by O-ions. However, in such cases, different types of indirect exchange can still lead to magnetic ordering.

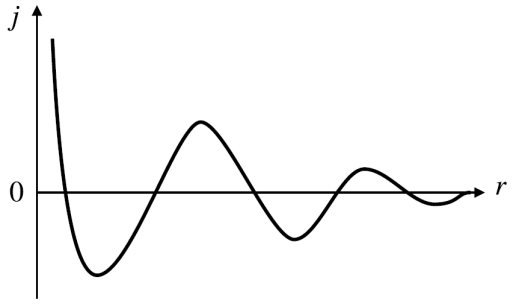

Figure 3.5: The RKKY coupling constant j as a function of distance r from a magnetic ion at the origin [53].

RKKY-interaction (named after Ruderman, Kittel, Kasuya and Yosida) describes magnetic ordering mediated by free conduction electrons. A magnetic ion will cause nearby conduction electrons to have opposite spin (due to Pauli's exclusion principle). These conduction electrons will, in turn, cause other spins (be they other conduction electrons or neighbouring magnetic ions) to have opposite spin to them. As a function of distance from the starting ion, spins will be coupled in a FM or AF fashion (see Figure 3.5). RKKY-interaction can therefore lead to FM or AF, depending on the distance between neighbouring atoms. The coupling constant j is described by

$$j \propto \frac{sin(k_m r) - 2k_m r cos(2k_m r)}{r^4}, \tag{3.1}$$

where k_m is the wavevector of the conduction electrons and r is the distance between two ions. Positive values of j indicate FM coupling, and negative values lead to AF coupling.

3.3.2 Superexchange and Double Exchange

In materials without free conduction electrons, magnetic coupling can be mediated by intermediate non-magnetic atoms. The rules that allows one to qualitatively predict the ordering in these situations are known as the Goodenough-Kanamori rules [54–56].

One such mechanism is superexchange (also known as Kramers-Anderson superexchange) [54,57], explained visually in Figure 3.6. Using two Mn-ions and an intermediary O-ion as an example, superexchange is the result of virtual hopping of the O-2p electrons

to the Mn-e_g orbitals they overlap with. Such a virtual hop can lead to a reduction in energy. But Pauli's exclusion principle dictates the hopping O-2p electron must have a spin opposite to the Mn-e_g electron. And from Hund's rules, we know that the Mn e_g electron has the same spin has the three t_{2g} electrons. This means that all four Mn $3d$ electrons have a spin opposite to the hopping O-2p electron.

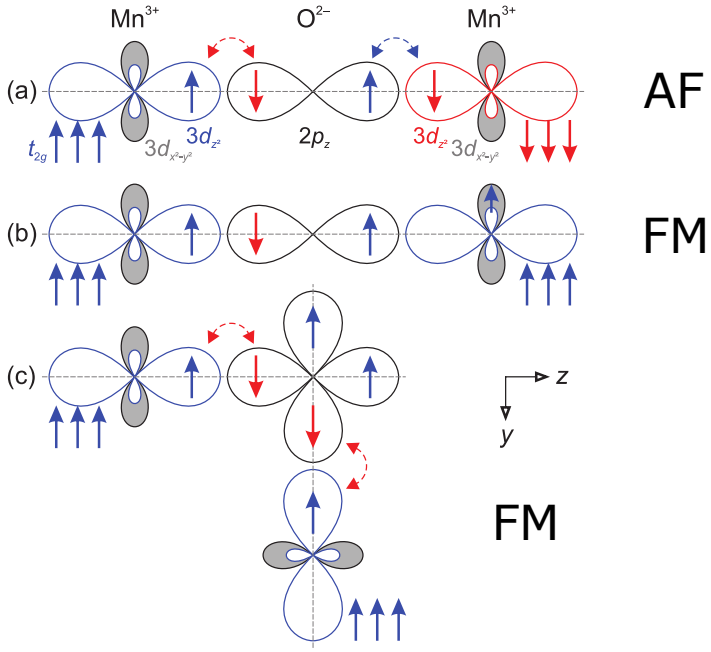

Figure 3.6: Schematic depiction of the superexchange mechanism, with the resulting magnetic ordering indicated [43].

Now, the leftover O-2p electron has some overlap with the e_g orbital of the other Mn ion. If the e_g electron of the second Mn ion is in the same orbital as the first (say, both are in the $3d_{3z^2-r^2}$ orbital), since this O-2p electron has a spin opposite to the first one, the second Mn-$3d$ electrons must in turn have a spin opposite to that. Combining this, the $3d$ electrons of the two Mn ions must have opposite spin, resulting in an AF coupling. This is shown in Figure 3.6a.

Now, if the e_g electron of the second Mn ion is in a different orbital compared to the first one (e.g., the first is in the $3d_{3z^2-r^2}$ orbital and the second is in the $3d_{x^2-y^2}$ orbital), virtual hopping will result in a reduction of energy if the spins of the electrons of the two Mn ions are aligned. The spin of the O-2p electron that is (virtually) hopping to the second Mn-e_g state (which is empty) has a spin with the same direction as the e_g electron of the first Mn ion. Now, Hund's rules say that the other $3d$ electrons of the second Mn ion must have the same direction as the hopping electron. This means the $3d$ electrons of both Mn ions will have the same spin, so they have FM coupling. This is shown in Figure 3.6b.

When our example Mn-O-Mn system forms a 90° angle, superexchange is done through virtual hopping of two O-2p electrons of different orbitals (in the case of Figure 3.6c, the $2p_z$ and $2p_y$ orbitals). The two hopping electrons should have the same spin (since the two electrons that stay behind should have the same spin following Hund's rules). If the two Mn ions have their e_g electron in the same orbital overlapping with the two hopping electrons, then they must have aligned spins as well (both being opposite to the hopping electrons). Therefore, this coupling is also ferromagnetic.

Out of these three superexchange situations, the first, AF coupling is the strongest [43]. As a result of the combination of superexchange and the Jahn-Teller distortion of

the unit cell of LMO, Mn ions in the ab-plane are coupled ferromagnetically, while along the c-axis, Mn ions are coupled antiferromagnetically [58, 59]. This means bulk LMO is an A-type antiferromagnet, and it has a Néel temperature of $T_N = 140$ K, above which LMO becomes paramagnetic [60].

The last exchange mechanism we will discuss here is double exchange. Whereas superexchange is mediated by virtual hopping of electrons, double exchange involves real hopping of electrons. In LMO, double exchange appears when part of the Mn^{3+} ions are replaced by Mn^{4+} or Mn^{2+} (see Sections 3.4 and 3.6). This mechanism is depicted schematically in Figure 3.7. In this example situation, the Mn^{3+} has an electron in the $3d_{z^2}$ orbital, whereas the Mn^{4+} ion does not. A O-2p electron can hop to the empty $3d_{z^2}$ orbital, turning the Mn^{4+} into Mn^{3+}. On the other side, the electron from the original Mn^{3+} ion's $3d_{z^2}$ orbital can hop to the O ion to fill the hole left behind, turning it into a Mn^{4+} ion. Both hopping electrons must have the same spin (since both form a pair with the remaining O-2p electron), leading to FM coupling between the two Mn-ions.

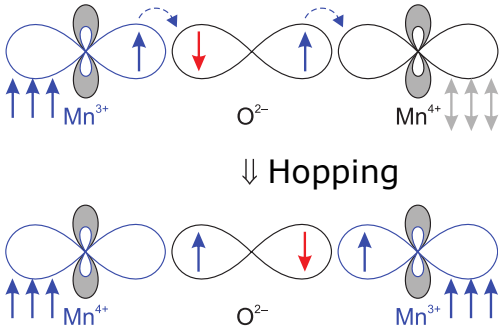

Figure 3.7: Schematic depiction of the double exchange mechanism [43].

3.4 Doping in the LMO system

As mentioned in the previous section, doping can change LMO from an antiferromagnet into a ferromagnet by altering the valency of some Mn ions. In general, perovskites are known for their sensitivity to doping [43], such as the $YBa_2Cu_3O_{7-\delta}$ system, which changes from an AF insulator to a high-T_c superconductor for small values of δ [61].

Doping in LMO (and perovskites in general) is done either through cation substitution (replacing La and/or Mn ions with other cations), through oxygen doping (i.e., $LaMnO_{3\pm\delta}$) or a combination of the two. Different dopants and doping content have different effects; this section will mostly focus on magnetic effects. Unless otherwise mentioned, this section discusses the bulk state.

The La^{3+} in LMO is often substituted with Sr^{2+} or Ca^{2+} (cation substitution), which donates holes to the system. These holes will cause part of the Mn^{3+} to form Mn^{4+}, which leads to double exchange and ferromagnetism, as explained earlier. $La_{1-x}Sr_xMnO_3$ (LSMO) in particular gets scientific attention for its uses in solid oxide fuel cells [62] and spintronics [63]. A look at the phase diagram for LSMO (Figure 3.8) shows different regions of FM and AF ordering.

Since SSM measurements are done at 4 K, the low-temperature region of the phase diagram is the most interesting. There are clear transitions from AF insulator to FM insulator to FM metal with increasing Sr-content.

Apart from cation substitution, oxygen doping is the other way of creating off-stoichiometric LMO. One can discern two cases: $LaMnO_{3+\delta}$ and $LaMnO_{3-\delta}$. Literature mostly describes both as $LaMnO_{3\pm\delta}$, but in reality, there is a fundamental difference

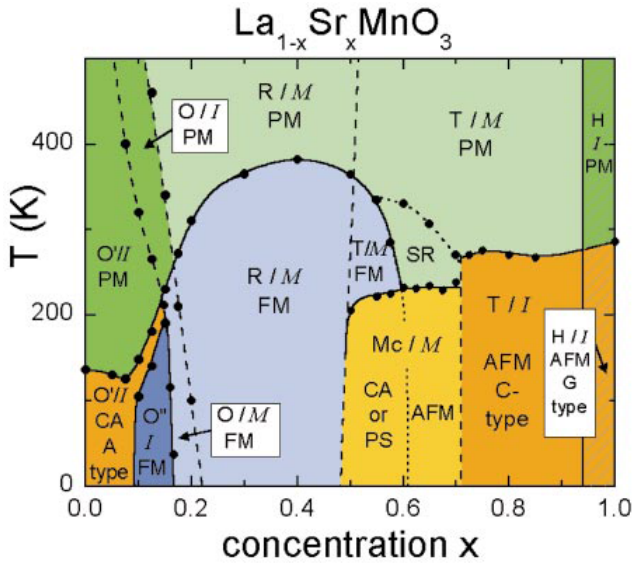

Figure 3.8: Phase diagram of $La_{1-x}Sr_xMnO_3$. PM - Paramagnetic; AFM - Antiferromagnetic (A, G and C denote AF ordering); FM - Ferromagnetic. M - Metal; I - Insulator. O' - Orthorhombic; O' - Jahn-Teller distorted orthorhombic; O" - Orbital-ordered orthorhombic; R - Rhombohedral; T - Tetragonal; Mc - Monoclinic; H - Hexagonal. From [64].

between the two. In $LaMnO_{3+\delta}$, excess oxygen cannot be incorporated into the crystal structure directly, but instead it creates La and/or Mn vacancies. Therefore, the correct formula should be written as $La_{3/(3-\delta)}Mn_{3/(3-\delta)}O_3$ [65]. In $LaMnO_{3-\delta}$, the structure does indeed contain oxygen vacancies as the formula would suggest.

Figure 3.9 shows part of the phase diagram for $LaMnO_{3+x/2}$. We can see that at the low end, bulk LMO remains in the AF state at low temperatures. Around $x = 0.07$, the phase diagram splits, and a mixed phase (denoted PS) appears, where AF and FM coexist, possibly due to electronic phase separation [66]. At higher doping levels ($x > 0.2$), LMO turns into a FM metal.

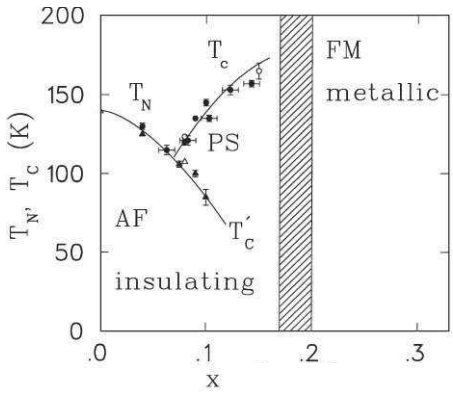

Figure 3.9: Phase diagram of $LaMnO_{3+x/2}$. T_c denotes the Curie temperature (measurements indicated with triangles), T_N is the Néel temperature (measurements indicated with circles). PS is a mixed-phase region [66].

In $LaMnO_{3-\delta}$, the non-stoichiometry is accomodated by oxygen vacancies [67, 68]. Though at first it was believed that these vacancies were distributed randomly throughout the lattice [67], Abbattista *et al.* showed that different phases ($La_8Mn_8O_{23}$ and

$La_4Mn_4O_{11}$) appear when δ is increased [68].

Later, it was shown that for $0.03 \leq \delta \leq 0.12$, $LaMnO_{3-\delta}$ is a mixed phase of $LaMnO_3$ and $La_8Mn_8O_{23}$ [69]. The mixed structural phase is accompanied by a mixed magnetic phase: one with a transition temperature of about 130 K, corresponding to T_N of $LaMnO_3$, and one with a transition temperature at 35 K, associated with the $La_8Mn_8O_{23}$ phase. Around $\delta = 0.12$ (i.e., $LaMnO_{2.88}$), the $LaMnO_3$ phase disappears and the $La_8Mn_8O_{23}$ (or $LaMnO_{2.875}$) phase remains [69].

3.5 Strain in the LMO system

When thin films are grown epitaxially on a substrate, there will be some amount of strain in the film due to the mismatch between the lattice parameters of the substrate and the film. The mismatch f is typically calculated as follows:

$$f = \frac{a_f - a_s}{a_s}, \tag{3.2}$$

where a_f and a_s are the lattice parameter of the film and the substrate, respectively. For example, one of the most commonly used substrates, $SrTiO_3$, will lead to a mismatch of approximately 2%.

Since epitaxial films will have a lattice parameter matching that of the substrate, the unit cell will change size in-plane. To compensate, it is common that films will change size accordingly in the out-of-plane direction. In strained films, strain energy will build up as the film thickness increases. When this energy becomes too high, the film will try to relax the strain by forming dislocations. These changes in structure (changes in lattice parameters and forming of dislocations) can lead to changes in the electronic and/or magnetic structure as well. For example, from the field of ferroelectric and multiferroic materials, strained films of $BaTiO_3$ can have their remanent polarisation increased by over 250% and their Curie temperature increased by over 500° C [70].

Taking an STO substrate as an example, Hou *et al.* showed that, due to the strain, the MnO_6 octahedra deform into two different types: Mn-A, which is elongated along the c-axis, and Mn-B, which is stretched in the ab-plane (see Figure 3.10). Because of this, the e_g state with the lowest energy will be different for each octahedron: for Mn-A octahedra, the d_{3z^2-r2} state will have the lowest energy, whereas for Mn-B octahedra, the $d_{x^2-y^2}$ state will have the lowest energy (as shown in Figure 3.10) [71].

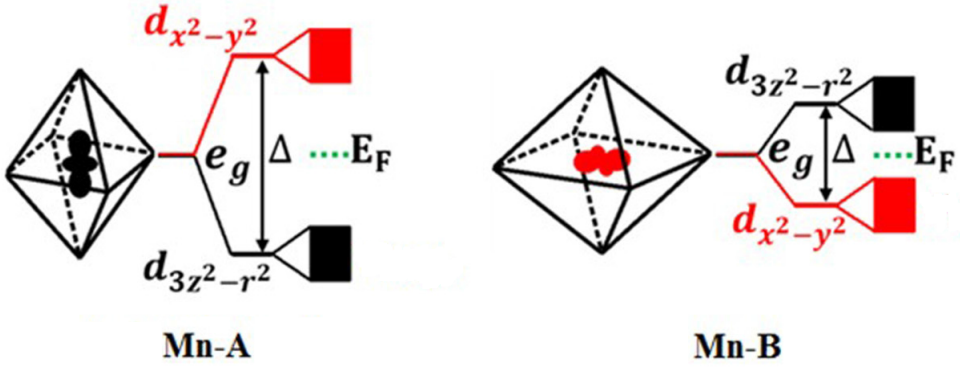

Figure 3.10: Deformation of the MnO_6 octahedra in strained LMO, leading to two different structures, denoted Mn-A and Mn-B. Adapted from [71].

Structurally, Mn-A and Mn-B alternate in a checkerboard (G-type) fashion. Now, referring to Figure 3.6b, we can see that having neighbouring e_g electrons in different

orbitals leads to FM ordering. In this way, strain, by changing the Mn-O bond lengths, can induce FM [71].

Figure 3.11 shows the energy of different magnetic and structural phases as a function of the lattice constant. Below $a = 3.87$ Å, LMO thin films will be an FM metal. For values of $3.87 \leq a \leq 4.03$ Å, the system will be an FM insulator, and when a increases above 4.03 Å, it will turn into an A-type AF insulator.

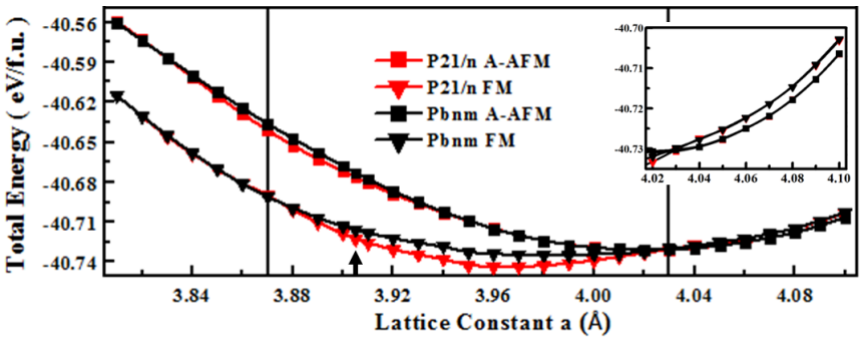

Figure 3.11: Magnetic phase energy versus the in-plane lattice constant. The black arrow indicates the commonly used substrate STO. The inset shows the region for $4.02 < a < 4.10$ [71].

Multiple theoretical papers have investigated the influence of strain in LMO thin films [48, 51, 52, 71], though correctly predicting the insulating FM state seen by experiments [72–74] has proven difficult [71]. Furthermore, not much has been reported on LMO thin films on substrates other than STO [49, 75]. For this reason, the strain effect in LMO is still a largely unexplored area.

3.6 Polar catastrophe and electronic reconstruction

In 2004, Ohtomo and Hwang discovered a conducting 2-dimensional electron gas (2DEG) at the interface between the insulators STO and LAO [76]. Soon after, more effects at this interface were discovered, such as superconductivity [77] and magnetism [78]. Although the mechanism behind the appearance of a 2DEG is not fully understood, the leading hypothesis is that it is due to an electronic reconstruction at the interface [79].

The basis for electronic reconstruction in LAO/STO is the 'polar catastrophe'. LAO is a polar material (as explained in Section 3.2), whereas STO is non-polar. This causes a polar discontinuity at the interface between these two materials. Due to the polar nature of LAO, an electric potential will build up as more layers are grown on top of the STO (see Figure 3.12a).

Now, if more and more layers of LAO are deposited, the potential would diverge, which is physically impossible. To resolve this, electrons are transferred from the surface to the interface. By relocating half an electron per unit cell to the interface, the polar catastrophe is removed (see Figure 3.12b), which is known as electronic reconstruction.

Since LMO, like LAO, is a polar material, one can expect that a similar situation arises when LMO is deposited on STO and a polar discontinuity is created. Despite the similar structure, research indicates that the interface between LMO and STO is not conducting and that no 2DEG is formed [80, 81].

Some recent studies, however, show that there does seem to be an electronic reconstruction scenario at the LMO/STO interface at a certain critical thickness [10, 82]. Wang *et al.* showed that, instead of leading to a conducting interface, ferromagnetism appeared at the LMO surface for layer thicknesses above 6 unit cells (uc). This tran-

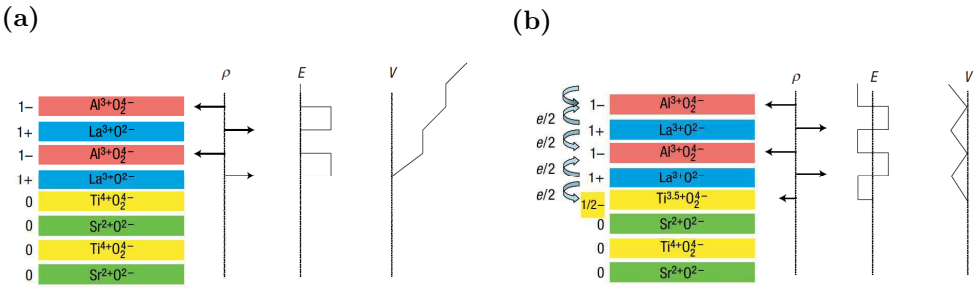

Figure 3.12: a) schematic representation of the polar catastrophe at the LAO/STO interface. b) resolution of the catastrophe by electronic reconstruction. ρ is the local charge, E the local electric field and V is the potential. Adapted from [79].

sition is atomically sharp, i.e., the FM signal measured by SSM increased by over 2 orders of magnitude when going from 5 to 6 uc LMO [10]. This mimics the behaviour of the LAO/STO interface, where the 2DEG appears at a critical thickness of 4 uc of LAO [83]. Mundy *et al.* used electron energy loss spectroscopy (EELS) to show a change in valency of Mn ions at the interface [82]. Similarly, electronic reconstruction has also been observed at LMO/$SrMnO_3$ interfaces [84, 85].

Wang *et al.* described the electron transfer using a simple first order model, where the internal electric field is

$$E_0 = \frac{e}{2A\epsilon_0\epsilon_r}, \tag{3.3}$$

where A is the unit cell area, ϵ_0 is the permittivity of the vacuum and ϵ_r is the dielectric constant of LMO [10]. This electric field shears the conduction and valence bands in the LMO, until a certain thickness t_t where the valence band at the surface rises above the conduction band at the interface and electrons start transferring (see Figure 3.13a).

t_t can be derived by equating the bandgap E_g of LMO (1.3 eV [86]) to the internal potential:

$$E_g = E_0 t_t \tag{3.4}$$

$$t_t = \frac{E_g}{E_0}. \tag{3.5}$$

Figure 3.13b shows the amount of transferred charge as a function of the thickness. The transferred charge q is described by

$$q(t) = \frac{1}{2n} e \left[1 - \frac{t_t}{t}\right], \tag{3.6}$$

where t is the thickness of the LMO layer and n is the number of layers the charge spreads across, which Wang *et al.* found to be equal to 2 [10]. We can see in Figure 3.13b that this simple model predicts the critical thickness t_c for the FM state to be 6 uc. Furthermore, we can also see that around 20 uc, the model predicts that LMO will be in the metallic FM state.

If electronic reconstruction happens in LMO/STO, it is easy to see how that leads to ferromagnetism. When electrons are transferred from the surface to the interface, they leave holes at the surface, which leads to the formation of Mn^{4+}. At the interface, the extra electrons will conversely lead to Mn^{2+} ions. As we have seen before, a mixed Mn valence state leads to double exchange, which gives rise to ferromagnetism.

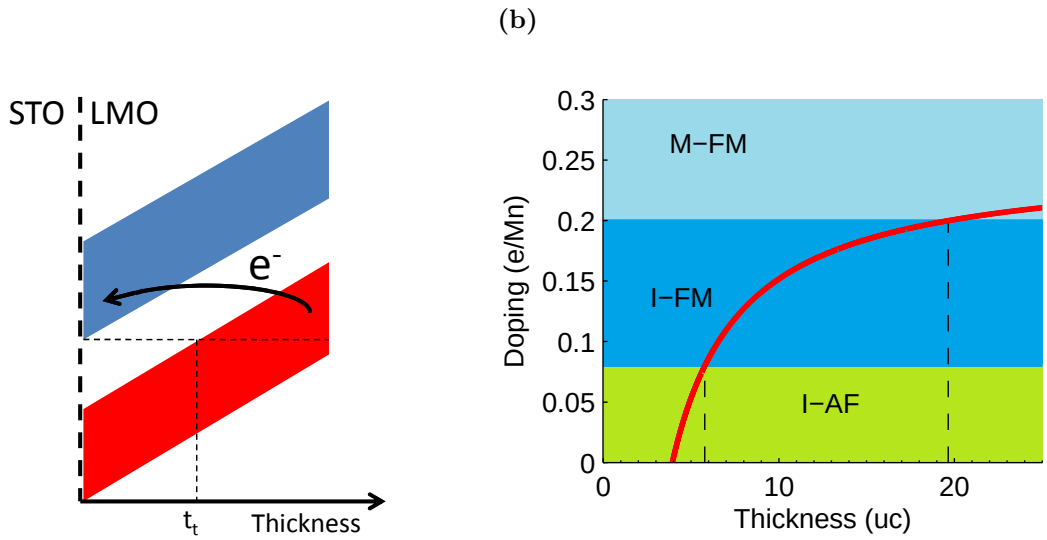

Figure 3.13: a) schematic representation of the sheared valence (red) and conduction bands near the LMO/STO interface due to the internal electric field E_0. b) Amount of transferred charge per Mn-ion as a function of thickness. The three coloured regions correspond to the insulating AF state (I-AF), the insulating FM state (I-FM) and the metallic FM state (M-FM).

3.7 Summary

LMO is a polar perovskite material that in the bulk shows insulating AF behaviour. We have discussed three different factors that can lead to FM ordering: doping, strain and electronic reconstruction (see Figure 3.14). Of course, these factors are not necessarily independent from one another. For example, doping can lead to small changes in the crystal structure which influences strain, or can lead to changes in the band gap which influences the electronic reconstruction. By fine-tuning these three parameters, different regions of the phase diagram can be explored and utilised for various experiments or devices.

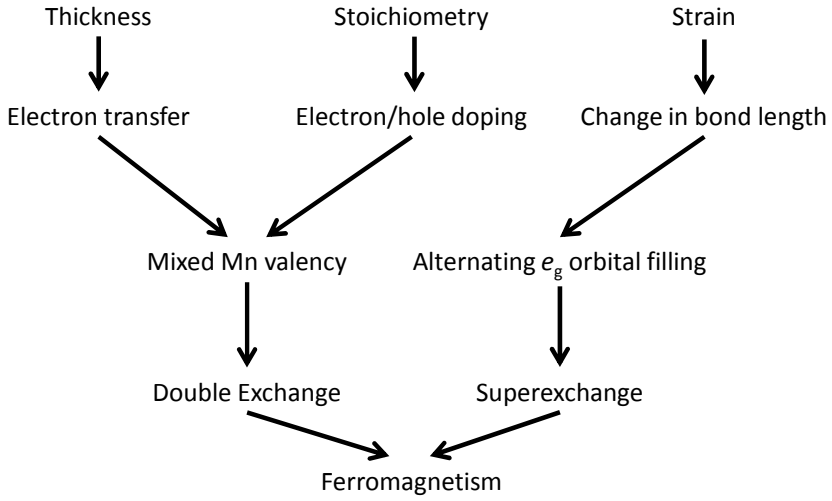

Figure 3.14: The three factors influencing magnetic ordering in LMO thin films.

4. Scanning SQUID Microscopy - Methodology

This chapter will discuss more of the imaging side of SSM. The focus will be on the two most important factors that impact the spatial resolution: scanning height z and the size of the pickup loop r_0. The influence of these two factors is explained and analysed by simulating several common magnetic features: vortices, dipoles and ferromagnetic domains. We will also briefly discuss some methods to improve spatial resolution post-scanning through deconvolution.

4.1 Spatial resolution

Although SSM and SQUIDs in general are highly praised for their field resolution, proper spatial resolution is just as important to understand the data obtained from an experiment. Apart from the physical size of the pickup loop, there are a few other factors that change the spatial resolution, which are discussed in this section.

One factor is the Meissner effect. Since the Nb pickup loop is superconducting, it will repel any magnetic field. This causes field lines that would otherwise go through the Nb to go through the inner radius of the ring, adding to the total field (see Figure 4.1a). This effect is known as flux focusing and increases the effective area A_e of the pickup loop. One can easily see that the thicker the pickup loop (t_l), the stronger this effect becomes.

As mentioned before, the angle also influences the effective area, as we can see in Figure 4.1a. The larger the angle, the smaller the effective area becomes. Apart from that, having the sensor under an angle will let it pick up in-plane components of the magnetic field. For now, we will focus on the z-component. Figure 4.1b shows the effective area A_e (scaled to the physical area A_0), as a function of both the angle θ and the thickness of the pickup loop t_l.

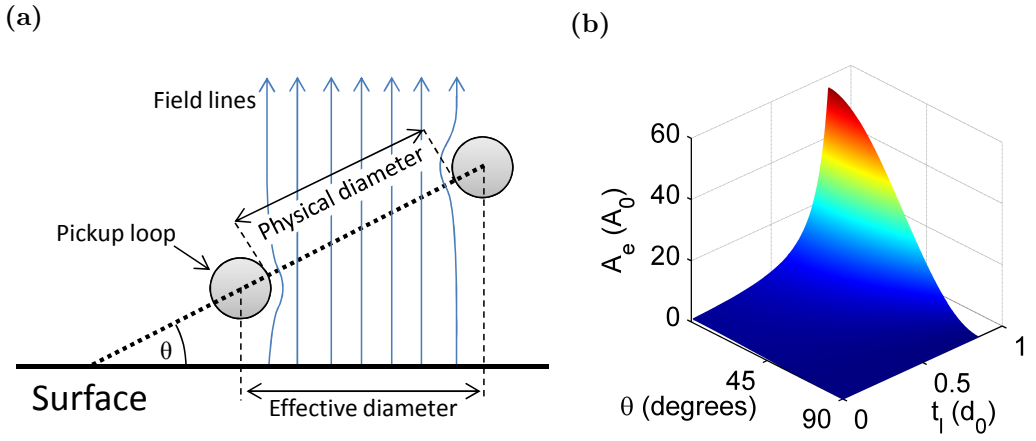

Figure 4.1: Schematic representation of the flux focusing effect when a magnetic field is present in the (superconducting) pickup loop.

In an SSM, spatial resolution is not only determined by the effective area, but also

by the distance z between the sensor and the sample. This is illustrated in Figure 4.2. It shows the magnetic field lines of two smaller magnetic domains (like one would find on the surface of a ferromagnetic material), and the field lines of several combined domains, like one would see at higher scanning heights. One can easily see that scanning at height h_1 will lead to a different signal than scanning at height h_2.

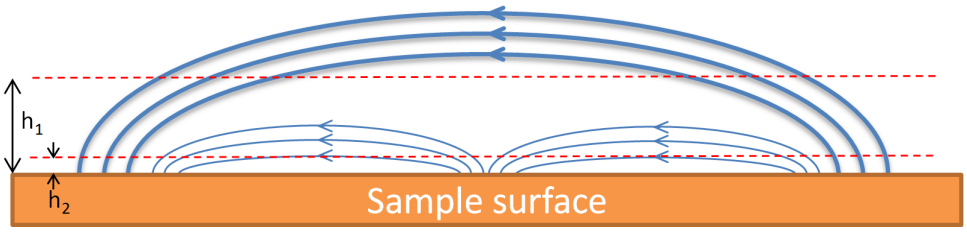

Figure 4.2: Schematic representation of the influence of sensor height when scanning magnetic domains. The upper curves represent the average field of several domains when measuring at larger distances.

We will define the spatial resolution of the SSM as the full width at half maximum (FWHM) of a scan of a vortex. As we will see, the spatial resolution is set by a combination of the physical size of the pickup loop and the distance between the sensor and the sample. Most accounts in literature use either the physical size of the loop or the sample-sensor distance as the spatial resolution, but defining it as we do here will include both factors and give a better idea of what to expect. This definition is only really valid for sensors with a diameter $d_0 \gg \lambda$, where λ is the London penetration depth of the scanned material, which doubles as the rough size of the vortices formed in that material.

Using this definition and a scan of vortices on the surface of $La_{2-x}Sr_xCuO_4$ (LSCO), we find the spatial resolution of our SSM setup to be approximately 11 μm, seen in Figure 4.3.

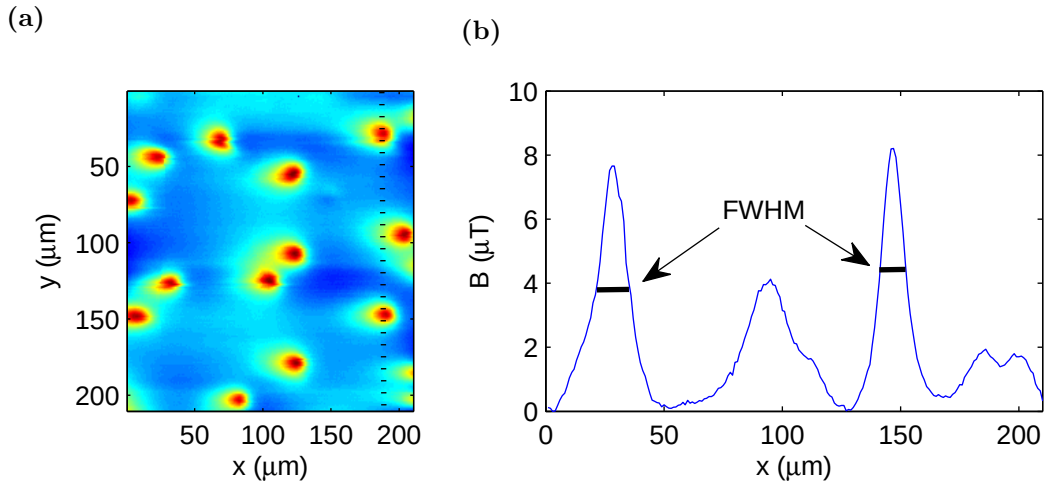

Figure 4.3: Analysis of the spatial resolution of the SSM setup by determining the FWHM (b) of a vortex along the dotted line in (a).

4.2 Vortices

SSM is often used to image vortices in superconducting materials. Due to the high flux sensitivity of SQUIDs, it is possible to image individual vortices, provided the spatial

separation between them is large enough. The radial size of a vortex is on the order of the London penetration depth λ (so a diameter of 2λ), which is usually several orders of magnitude smaller than d_0 (e.g., for Nb, $\lambda = 39$ nm). This means that when imaged with SSM, a vortex will appear larger due to the large pickup loop. From Figure 4.4 we can see that the apparent size of a vortex d_v will be roughly $d_v = d_0 + 2\lambda$, though as we will see shortly, there is a little more to it.

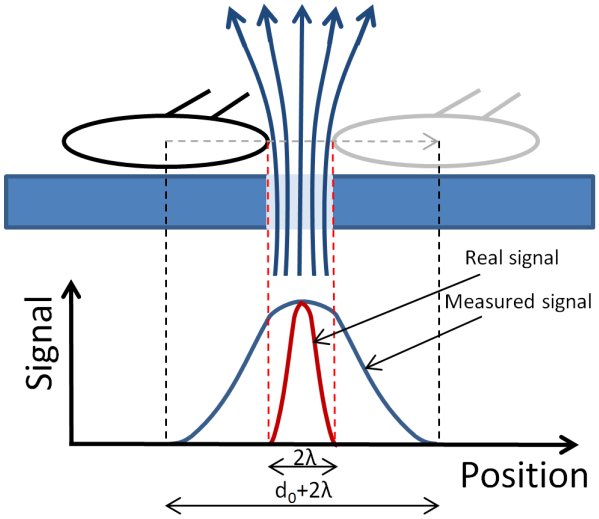

Figure 4.4: Influence of the pickup loop diameter d_0 on the signal measured when scanning a vortex with diameter 2λ.

This broadening of features is because of a convolution of the pickup loop with the signal, which can be described as

$$s = f * \ell, \tag{4.1}$$

where s is the measured signal, f is the original signal and ℓ is the function describing the pickup loop, also known in general as the transfer function, impulse response or, in terms of deconvolution, the point-spread function (PSF). Of course, this effect due to the finite size of the pickup loop applies to every situation, not just vortices. Therefore, it is important to consider the size of the pickup loop when determining the size of features in a scan, especially when d_0 is on the order of the feature size. However, as we have seen in Section 4.1, not only the size of the pickup loop is relevant, the height at which the scan is made is also important.

To get more insight how both these factors influence scans of vortices, several simulations were done. The field of a vortex at distances $r \gg \lambda$ is given by

$$\mathbf{B} = \frac{\Phi_0}{2\pi r^3}\mathbf{r}, \tag{4.2}$$

which is the monopole approximation of a vortex [87].

The simplest situation we can look at is when the pickup loop is centred exactly above the vortex. By integrating the above equation, we can find the total flux penetrating the loop when measuring at height z:

$$\Phi = \Phi_0 \left[1 - \frac{z/r_0}{\sqrt{1 + z^2/r_0^2}}\right]. \tag{4.3}$$

Figure 4.5 shows the measured flux Φ as a function of the ratio z/r_0. By plotting it this way, the graph is universal for different sizes of pickup loops. From the graph we can see that at a ratio of 1, the measured flux is about 0.29 Φ_0. For our own setup, that would equate to roughly $z = 10$ μm, which is easily attainable.

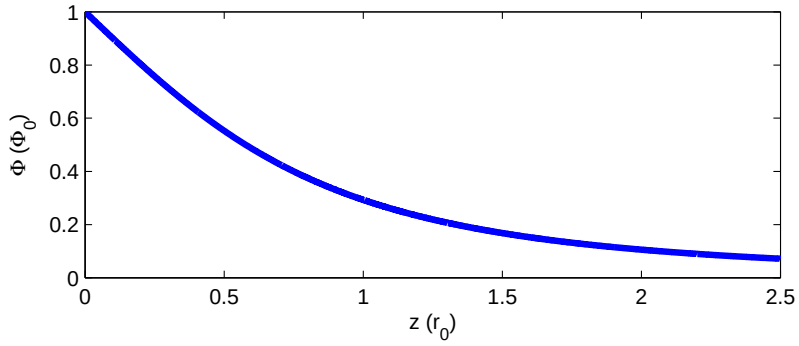

Figure 4.5: The measured flux Φ as a function of the ratio z/r_0.

The next step is to see what an actual scan of a vortex would look like for different z. Figure 4.6 shows simulations for some values of z. It is clearly visible that the vortex appears larger at higher z, while its intensity decreases. This is to be expected, due to the magnetic field lines spreading out at larger distances from the source.

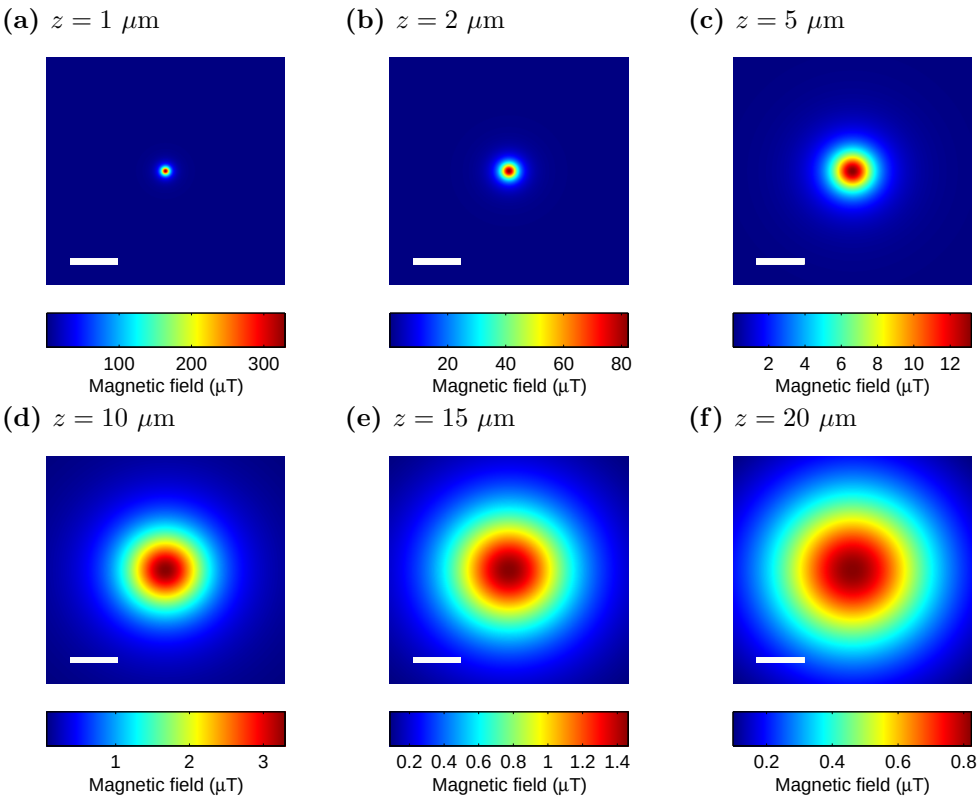

Figure 4.6: Simulated SSM scans of a vortex at different z: a) 1 μm; b) 2 μm; c) 5 μm; d) 10 μm; e) 15 μm; f) 20 μm. The scale bars indicate 10 μm.

Figure 4.7 shows the apparent diameter d_v of the vortex as a function of scanning height. d_v is defined here as the full width at half maximum, and measured from the simulated data. This definition is used since it can also be easily measured from scanning data.

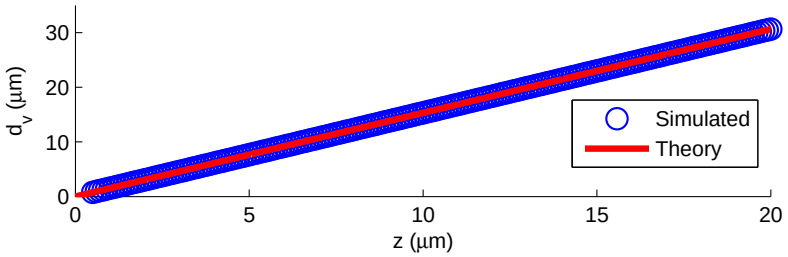

Figure 4.7: d_v as a function of z, simulated (open circles) and from theory (solid line).

We can also deduce d_v directly from Equation 4.2:

$$B_{max}(z) = \frac{\Phi_0}{2\pi}\frac{1}{z^2}, \tag{4.4}$$

$$B_{halfmax} = \frac{\Phi_0}{2\pi}\frac{1}{2z^2}. \tag{4.5}$$

$$\tag{4.6}$$

To find d_v, using axial symmetry, we set $y = 0$ and find the x coordinate corresponding to half maximum:

$$\frac{\Phi_0}{2\pi}\frac{1}{2z^2} = \frac{\Phi_0}{2\pi}\frac{z}{(x^2+z^2)^{3/2}}, \tag{4.7}$$

$$\frac{1}{2z^2} = \frac{z}{(x^2+z^2)^{3/2}}, \tag{4.8}$$

$$(x^2+z^2)^{3/2} = 2z^3, \tag{4.9}$$

$$x = z\sqrt{2^{2/3}-1}. \tag{4.10}$$

Now, d_v follows simply: $d_v(z) = 2x = 2z\sqrt{2^{2/3}-1} \approx 1.53z$. This agrees with the simulation as shown in Figure 4.7.

The previous simulations were done assuming the field measured by the pickup loop corresponds pixel for pixel with the simulated field. In reality, the finite size of the pickup loop smears out the signal, as was shown before in Figure 4.4. To simulate a pickup loop, for each point, we take the average of all points within a radius r_0 around that point. Figure 4.8 shows simulations of a vortex scanned at $z = 2$ μm for different r_0.

As expected, a larger r_0 leads to a larger apparent diameter of the vortices, due to the pickup loop averaging out the field over larger areas. We can have another look at d_v against z, but this time varying the size of the pickup loop. The result of these simulations is shown in Figure 4.9.

We can see in Figure 4.9 that, at smaller z, d_v seems to flatten out at a value equal to d_0. This makes sense, as at low z, the size of the pickup loop is the dominant factor, leading to a size roughly equal to d_0 as explained in Figure 4.4. Then at higher z, it converges to the line from Figure 4.7. We can roughly divide the figure into two regions: a region where the factor dominating d_v is r_0, and a region where the dominating factor is z.

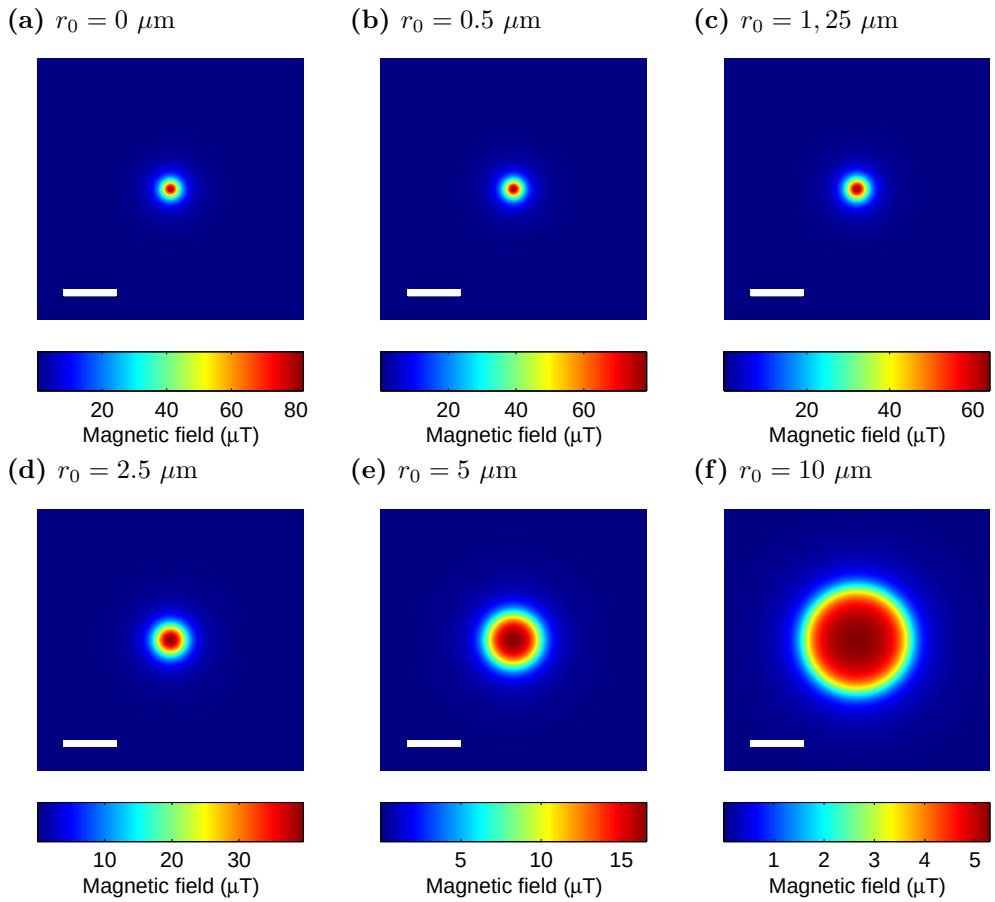

Figure 4.8: Simulations of vortices scanned at $z = 2$ μm for different r_0: a) Original; b) $r_0 = 0.5$ μm; c) $r_0 = 1.25$ μm; d) $r_0 = 2.5$ μm; e) $r_0 = 5$ μm; f) $r_0 = 10$ μm. The scale bar indicates 10 μm.

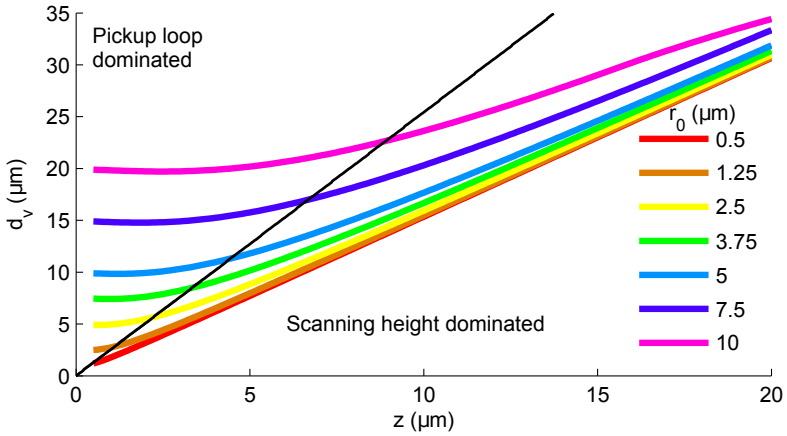

Figure 4.9: d_v as a function of z for different r_0.

4.3 Dipoles and ferromagnetic structures

Another common magnetic feature are magnetic dipoles. Small ferromagnetic particles or grains display a dipole-like behaviour when imaged with SSM. Although these particles are physical dipoles, as long as the particle is smaller than the pickup loop or the pickup loop is far enough away, the field can reasonably be approximated by a point dipole. Larger features can be represented as a sum of multiple point dipoles, as we will see later [88].

The field B_z of a dipole is determined by its magnetic moment $\mathbf{m}$. The equations for the field due to each component of $\mathbf{m}$ are given by:

$$B_{z,x}(x,y,z) = \frac{\mu_0}{4\pi} 3m_x \frac{xz}{(x^2+y^2+z^2)^{5/2}} \tag{4.11}$$

$$B_{z,y}(x,y,z) = \frac{\mu_0}{4\pi} 3m_y \frac{yz}{(x^2+y^2+z^2)^{5/2}} \tag{4.12}$$

$$B_{z,z}(x,y,z) = \frac{\mu_0}{4\pi} m_z \frac{3z^2-(x^2+y^2+z^2)}{(x^2+y^2+z^2)^{5/2}}, \tag{4.13}$$

where μ_0 is the magnetic permeability of free space and $B_z = B_{z,x} + B_{z,y} + B_{z,z}$. A derivation of these equations can be found in Ref. [88].

We will start in similar fashion as we did with the dipoles by looking at the z-dependence of scans by simulating the above equations. The resulting images for a selection of z-values can be seen in Figure 4.10. The dipoles simulated here have a magnetic moment of $\mathbf{m} = \{1,1,0\}\mu_B$.

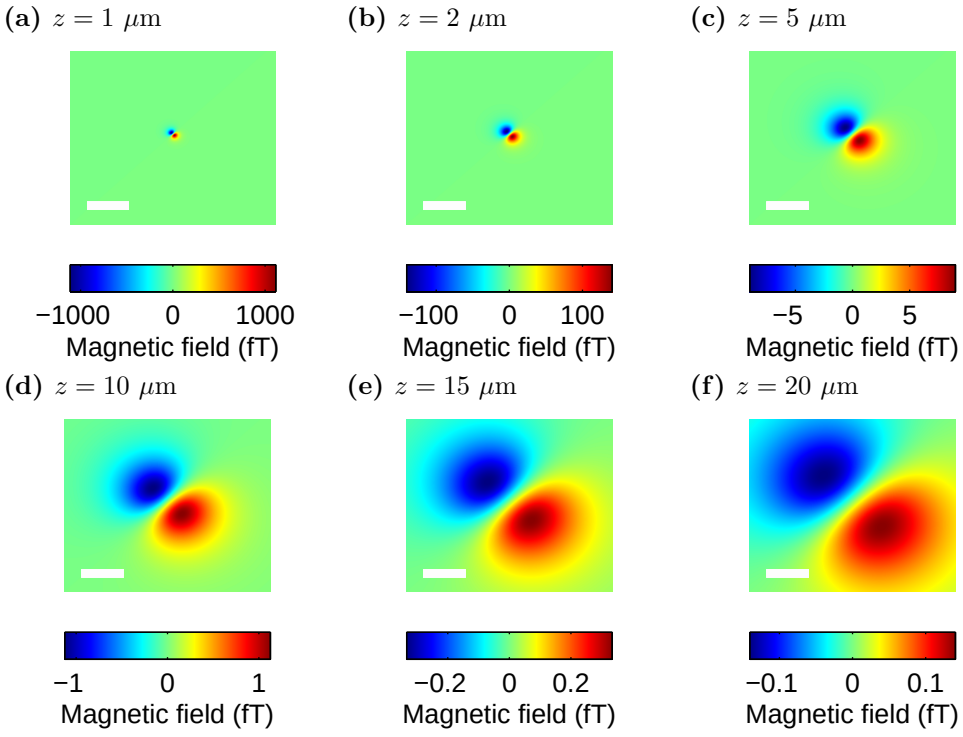

Figure 4.10: Dipoles at different z: a) $z = 1$ μm; b) $z = 2$ μm; c) $z = 5$ μm; d) $z = 10$ μm; e) $z = 15$ μm; f) $z = 20$ μm. The scale bar indicates 10 μm.

Again we see that the apparent size of the dipole increases with z, just like for vortices. In the same vein, the measured field decreases sharply with increasing z: almost a factor 10^4 with z increasing a factor of 20, displaying the $1/r^3$ nature of dipoles.

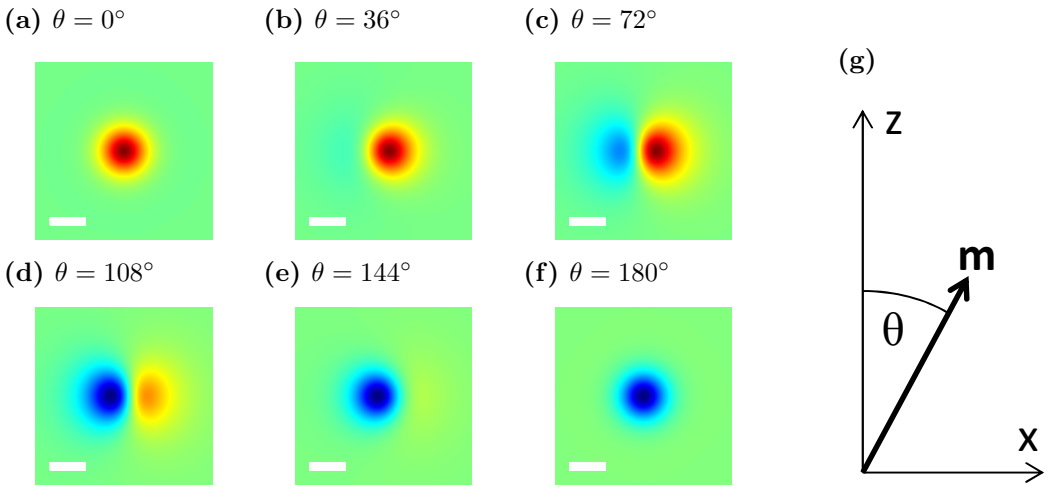

Figure 4.11: Dipoles simulated in the xy-plane, at different angles θ in the xz-plane: a) $\theta = 0°$; b) $\theta = 36°$; c) $\theta = 72°$; d) $\theta = 108°$; e) $\theta = 144°$; f) $\theta = 180°$. Scale bar indicates 10 μm, simulated for $z = 10$ μm. g) Definition of angle θ.

The dipoles in Figure 4.10 have a magnetic moment in the xy-plane. Of course, a real dipole could be oriented in any 3-dimensional direction. Figure 4.11 shows a dipole in different orientations in the xz-plane. We can see that the second lobe is only really visible in Figure 4.11c and d, with only a very faint signal present in Figure 4.11b and e.

When oriented along or close to the z-axis, the dipoles resemble the vortices we have seen in the previous section. However, the dipole field is, of course, different from the monopole field approximation we used for the vortices ($\propto \frac{1}{z^3}$ as opposed to $\propto \frac{1}{z^2}$ for the vortices). Furthermore, since ferromagnetic particles or regions and superconductivity do not typically coexist (see Refs. [89–92] for some rare cases), mixing the two up is unlikely.

One typical involving dipoles we will discuss here concerns materials with magnetic grains in them. This might be the case, for example, when scanning geological rock samples, archaeological finds, contaminated samples, etc. These grains, depending on their size, will appear as dipoles on an SSM image. Now, depending on the magnetic environment in which the material was formed (and kept), the magnetisation direction of these dipoles might be uniform or, on the other end of the spectrum, randomly oriented.

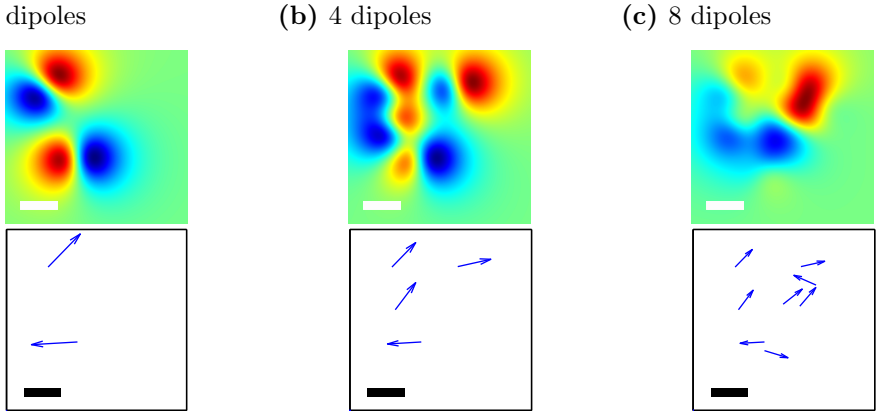

Figure 4.12: Clusters of randomly oriented dipoles. a) 1 dipole; b) 4 dipoles; c) 8 dipoles. The figures in lower row indicate the location and orientation for the dipoles in the top row.

Figure 4.12 shows what clusters of dipoles located closely together might look like. These dipoles are oriented randomly in 3 dimensions, lying in the xy-plane. These dipoles all have the same magnetic moment of 1 μ_B. As we can see, especially from Figure 4.12c, one may not be able to discern each indidividual dipole easily. Even a few dipoles can create a (visually) complex pattern.

Finally, any ferromagnetic object can be viewed as a summation over particles, each producing a dipole field. This way, we can simulate larger ferromagnetic features and see how they would appear under an SSM. Some examples with an H-shaped structure are shown in Figure 4.13. The magnetisation corresponds roughly to 1 monolayer of saturated bcc-Fe [93], though at the moment, we are more interested in the visual aspect. We can see that the outline of the structure may not be that easy to discern, depending on the magnetisation direction. However, combining an SSM scan of such a structure with, for example, an AFM image will give a good picture of how the magnetic field behaves around said structure.

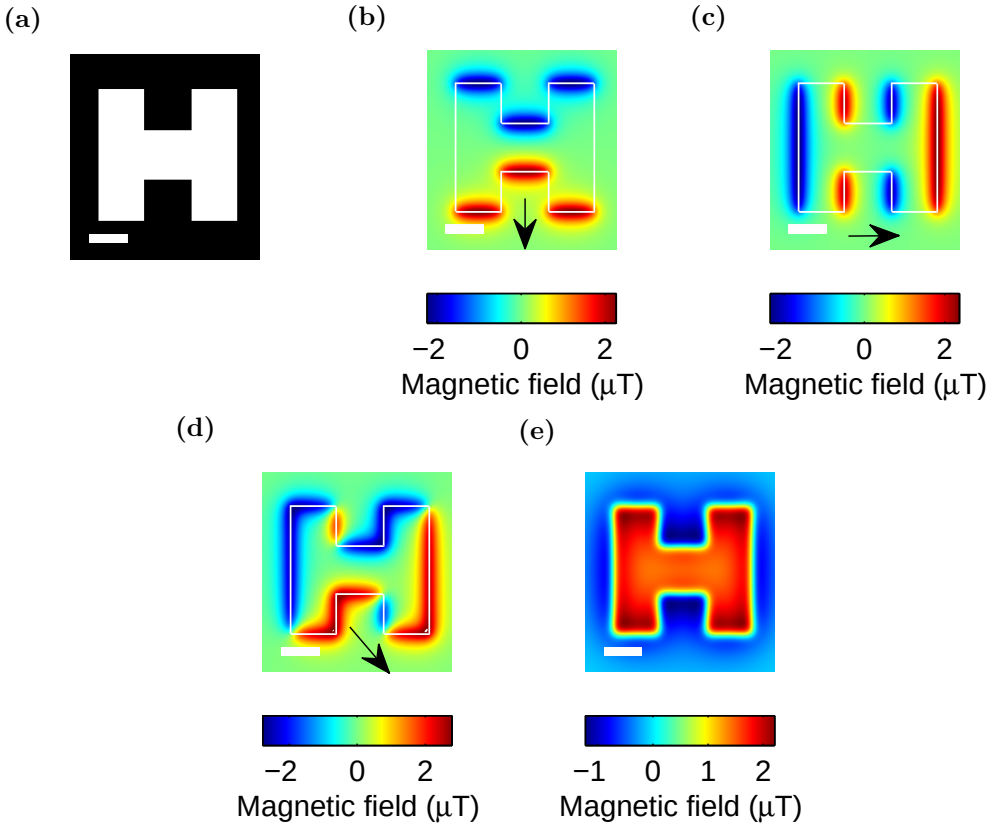

Figure 4.13: a) An example H-shaped structure with simulated with differently oriented magnetisations: b-d) in-plane, in the direction indicated by the arrow, the outline of the structure in white; e) out-of-plane. The scale bar indicates 20 μm.

Of course, these simulations assume that the structure is perfectly uniformly magnetised, which need not be the case. The examples in Figure 4.13, however, serve more to show the techniques we will use in the next section to perform simulations of ferromagnetic domains.

4.4 Ferromagnetic domains

This section discusses the simulation of ferromagnetic domains. Resolving individual domains properly is important to understand how the various forces forming these domains balance out. We will also again look at how the scanning height and the pickup loop alter the scans. Simulating and analysing ferromagnetic domains is relevant since most of our current SSM experiments at the University of Twente are aimed at samples that show this kind of behaviour (such as the experiments described in Chapters 5 and 6).

For simplicity, the domains in these simulations are created by generating a Voronoi diagram around randomly distributed points in a 100 by 100 μm^2 plane (Figure 4.14a and b). Each Voronoi cell is then assigned a magnetisation, which creates a domain structure (Figure 4.14). Again for simplicity, it is assumed that the magnetisation aligns itself along crystallographic axes. The total field is then calculated by treating each pixel (which represents 0.1 by 0.1 μm^2, or about 256 by 256 unit cells of LMO per layer) as a dipole and calculating the dipole field as imaged by an SSM at a certain height z. This is shown in Figure 4.14d.

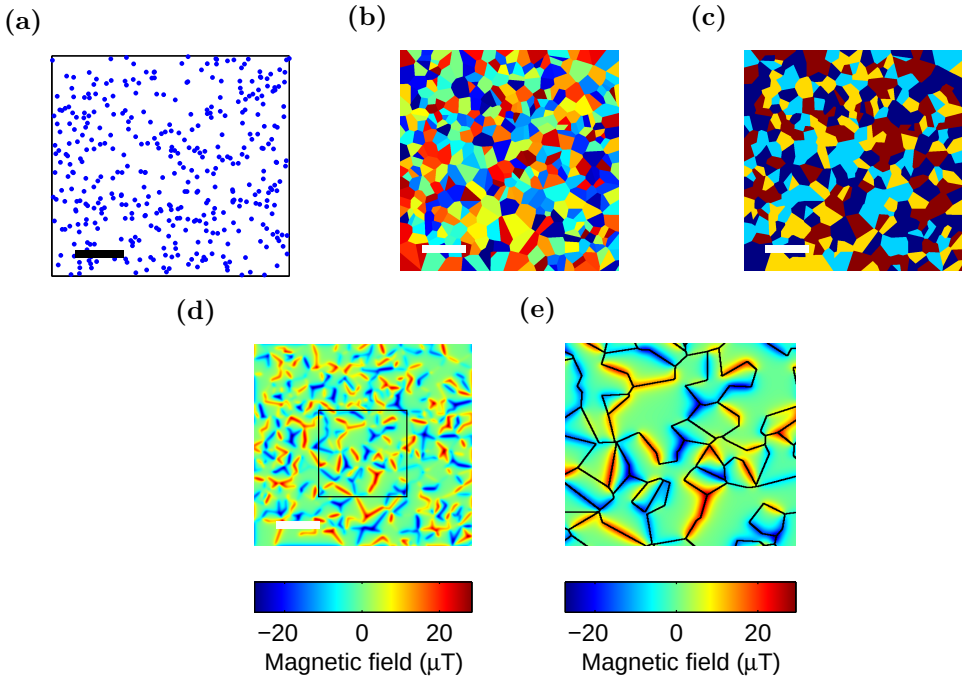

Figure 4.14: Four steps of simulating ferromagnetic domains: a) randomly create N points in an area ($N = 400$ in this simulation); b) create a Voronoi diagram out of these points; c) assign a magnetisation direction to each domain created in b); d) calculate the magnetic field. The scale bar indicates 20 μm. e) Zoom of the boxed region in (d), with the domain walls outlined in black.

These simulations were done assuming 1 layer of ferromagnetic LMO, with each unit cell contributing 1 μ_B (similar to what has been found in real LMO thin films [10] and by ourselves in Chapter 5 and 6). A total of 400 mathematical domains make up these simulations. The field strength displayed in Figure 4.14d is comparable to what we find in real scans (i.e., on the order of 10 μT), showing that at least field-wise, these simulations are accurate.

From Figure 4.14d we can also see that the magnetic field is strongest at the domain walls, and close to zero in the domain centre. This makes sense, since for in-plane

domains, the field lines will run parallel to the surface along the domain, and only obtain an out-of-plane component at the domain walls to close the loops.

To illustrate the influence of z, Figure 4.15 shows simulations with the same parameters as above, but changing z from 1 μm up to 20 μm. We can see that at $z = 2$ μm, the domains are still fairly recognisable, but at higher z, the fine structure is lost. By calculating the root-mean-square field strength B_{RMS} and plotting it as a function of z, we can see that it sharply decreases as the scanning height increases. B_{RMS} is given by

$$B_{RMS} = \sqrt{\frac{1}{n}\sum_{i=1}^{n}(B_i - \bar{B})^2} \tag{4.14}$$

where $\bar{B}$ is the average magnetic field, B_i is the magnetic field at point i and n is the total number of data points.

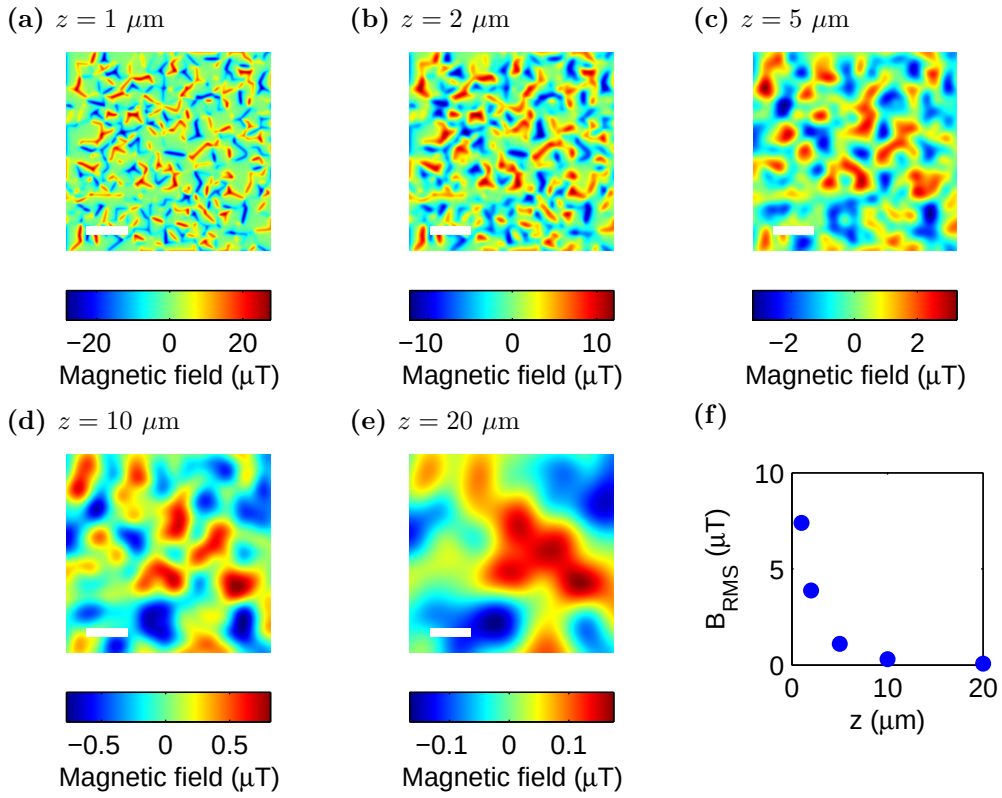

Figure 4.15: Simulated SSM scans of a ferromagnetic surface with in-plane magnetised domains. The simulated scanning heights are: a) 1 μm; b) 2 μm; c) 5 μm; d) 10 μm; e) 20 μm. The scale bar indicates 20 μm. f) B_{RMS} as a function of z.

The main point to take away here is that due to the averaging of domains (most noticeably in Figure 4.15e), one cannot easily make statements about the domain structure from an SSM scan. The difference between Figure 4.15a and Figure 4.15e will be similar when going down in scale and imaging smaller domains at smaller z. The only real way to say something about the domain sizes is when scans are in the range of Figure 4.15a, where the images are so sharp the domains become clearly visible: strong signal at the edges, and almost no signal above the domains themselves.

To illustrate the difference between magnetisation directions, Figure 4.16 shows simulations with the same parameters as the ones in Figure 4.15, but with the magnetisation out-of-plane instead of in-plane.

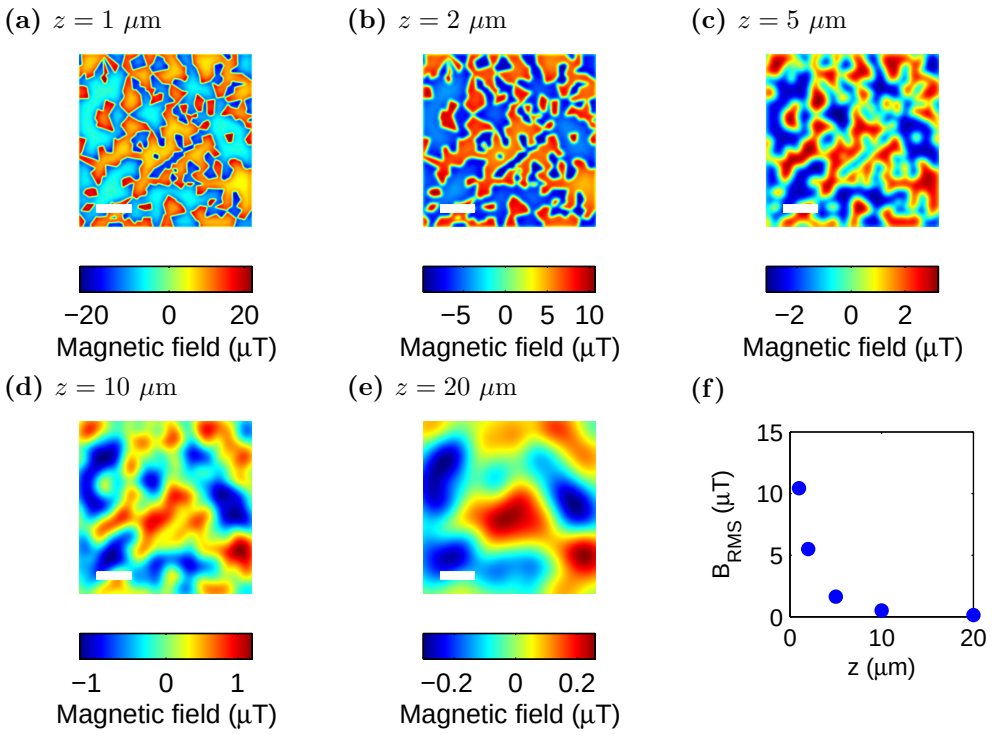

Figure 4.16: Simulated SSM scans of a ferromagnetic surface with out-of-plane magnetised domains. The simulated scanning heights are: a) 1 μm; b) 2 μm; c) 5 μm; d) 10 μm; e) 20 μm. The scale bar indicates 20 μm. f) B_{RMS} as a function of z.

Comparing the simulations in Figure 4.16 with the in-plane simulations show a striking difference. As expected, in this case, the magnetic signal is strongest at the centre of the domains, where the field lines enter or exit the surface, and lowest at the domain walls where the magnetisation flips from one direction to another. Comparing Figure 4.15a to Figure 4.16a, we can see that at this level of detail, the difference between in-plane and out-of-plane magnetisation is very clear.

However, as z increases, we see that at some point, in-plane and out-of-plane magnetisation become indistinguishable from one another. This means that, unless the spatial resolution is good enough, SSM imaging may not be enough to determine the orientation of the magnetisation. We also see a similar behaviour in B_{RMS}, decreasing rapidly with increasing z. It starts out at a higher value compared to Figure 4.15f, which is due to the out-of-plane magnetisation, thus having the field primarily along the z-axis.

So far, we have used B_{RMS} as a way to quantify the overall magnetic field strength. In a real experiment, one of the things of interest is the total magnetic moment per unit cell, or per magnetic ion. Normally, this calls for a vibrating sample magnetometer (VSM) measurement, but it is interesting to see if and how we can relate SSM scans to the magnetic moment through the value of B_{RMS}.

Figure 4.17 shows the result of series of simulations done with the same domain structure at $z = 1$ μm, but with a different magnetic moment M per unit cell. Since each simulation in a series has the same visual output, only with a different field scale, one representative image with $M = 2$ μ_B/uc is shown for each series. Figure 4.17c shows B_{RMS} as a function of M, showing a linear behaviour. The slope is related to the 'waveform' of the magnetic field, much like root-mean-square value of a sine-wave has a value of $a/\sqrt{(2)}$ where a is its amplitude. Of course, the coefficient is also determined in part by z, but that parameter is not our focus here. These simulations basically show that, if the coefficient is known, one can calculate the magnetic moment from SSM

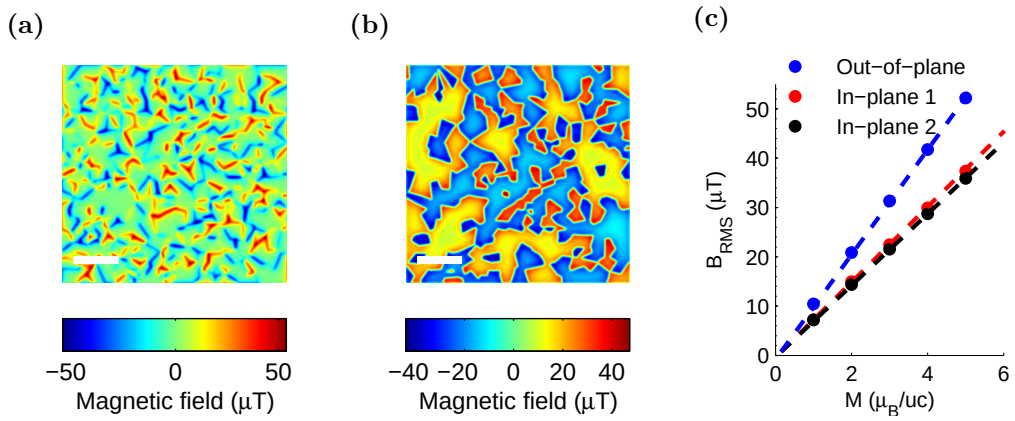

Figure 4.17: a) Simulated SSM scan of a ferromagnetic surface with in-plane magnetised domains, with $M = 2\ \mu_B$/uc. b) Simulation with the same M but now oriented out-of-plane. c) B_{RMS} as a function of M. The dashed lines are guides to the eye.

measurements. However, a direct VSM measurement will always be a better method of measuring M.

We see that there is a slight difference between the two in-plane simulation series in Figure 4.17. Since all parameters were kept the same between series, this can only be due to the randomised domain structure. One could imagine that simulating larger and larger areas would reduce this error and result in a single coefficient. We also see that there is a more noticeable difference between the in-plane and out-of-plane series. The out-of-plane naturally will create a larger B_{RMS} due to almost every data point having its field aligned along the z-direction.

The above simulations were performed without taking the finite size of the pickup loop into account. Naturally, this is not representative of a real SSM scan, as we have discussed before. To illustrate the effect of a pickup loop, we do the same as we did with the vortices in the previous section. Figure 4.18 shows how the image changes as the radius of the pickup loop r_0 changes. As one would expect, the value of B_{RMS} drops with increasing loop radius (Figure 4.18f).

The image also changes visually in a different way compared to Figure 4.15. The simulations at high z look smoother than the simulations convoluted with high r_0 do. Interestingly, Figure 4.18a-c look almost identical to Figure 4.15a-c, even though they are created in a different way. Much like with increasing z, the domain structure becomes lost due to the convolution, meaning that in a real image, one would not be able to make conclusions regarding the domain structure.

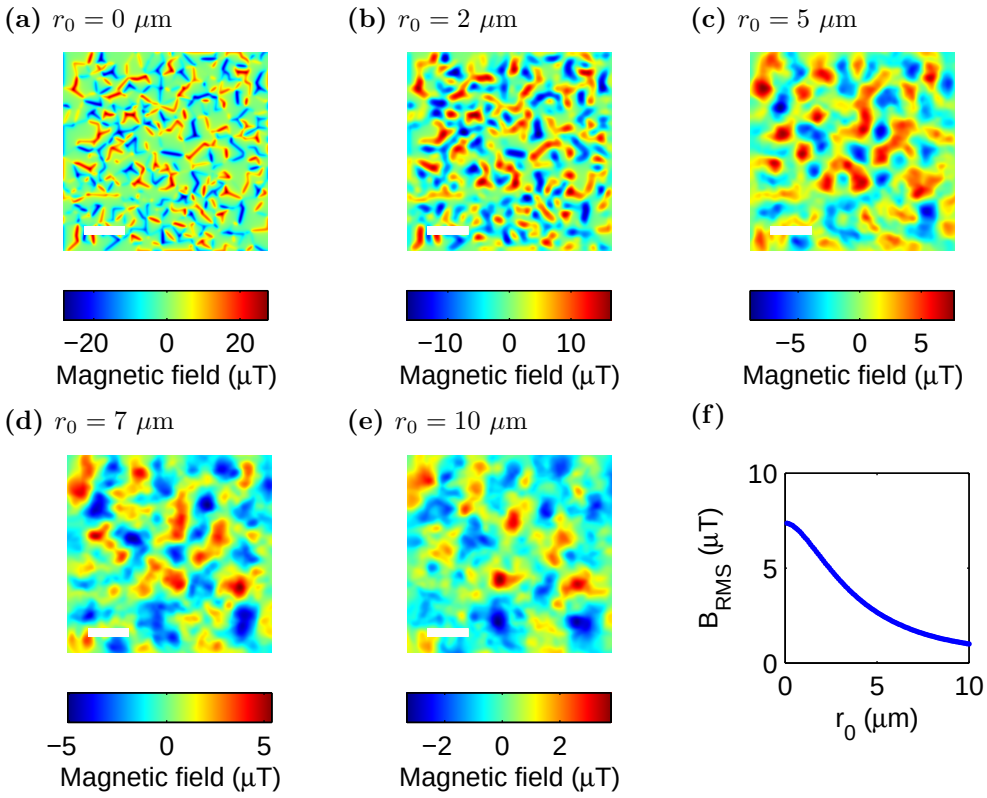

Figure 4.18: a) Original simulation. b-e) Convoluted image with r_0 of 2, 5, 7 and 10 μm, respectively. The scale bars indicate 20 μm. f) B_{RMS} as a function of the loop radius r_0.

4.5 Deconvolution

A way to gain spatial resolution is to use deconvolution methods on the data. As we have discussed, the data from an SSM scan is the convolution of the actual magnetic signal and the finite size of the pickup loop (Eq. 4.1). Performing a Fourier transform, a convolution in real space becomes a multiplication in Fourier space:

$$s(x,y) = f(x,y) * \ell(x,y) \xrightarrow{\mathcal{F}} s_F(k_x,k_y) = f_F(k_x,k_y)\ell_F(k_x,k_y), \tag{4.15}$$

where $\mathcal{F}$ denotes the Fourier transform.

Ultimately, deconvolution attempts to find the PSF and with it, make the division in Fourier space to obtain $f_F(k_x,k_y)$ and then perform an inverse Fourier transform to obtain the desired data $f(x,y)$. There is plenty of literature available on different deconvolution methods and concepts in various fields (for some reviews, see Refs. [94–97]), but only a handful of papers is dedicated to the deconvolution problem in SSM [98–100].

The intent of this section is not to develop deconvolution methods that can be applied to SSM scans, but rather, through some examples, highlight the strengths and weaknesses of deconvolution.

4.5.1 The point spread function

Unfortunately, there is no 'one-size-fits-all' deconvolution method. A variety of algorithms exists, the choice depending on how well known the system is (amount of noise, the PSF, etc.). Some can be found in the literature listed above.

For the real SSM setup, one likely option is blind deconvolution. Blind deconvolution is an iterative process that requires no prior knowledge of the PSF, and attempts to guess the PSF and restore the image. In the case of our own system, the PSF is hard to determine, due the fact that every sensor is different (which means the PSF will have to be determined for each new sensor) and due to differences in scanning height and the angle between the sensor and the sample (meaning the PSF will have to be determined for each scanning session).

Most deconvolution methods, however, require some knowledge of the PSF. In optical microscopy and astronomy, the PSF is typically determined by imaging a point (i.e., sub-resolution) light source, such as a star for telescopes or fluorescent nanoparticles for microscopes [94, 101]. In scanning SQUID microscopy, the functional equivalent of a point light source would be a superconducting vortex. Looking at Equation 4.15, normally we would recover the image by rewriting it as follows:

$$f(x,y) = \mathcal{F}^{-1}\left(\frac{s_F(k_x,k_y)}{\ell_F(k_x,k_y)}\right), \tag{4.16}$$

where $\mathcal{F}^{-1}$ is the inverse Fourier transform. To find the PSF of our own system, we can flip this equation around:

$$\ell(x,y) = \mathcal{F}^{-1}\left(\frac{s_F(k_x,k_y)}{f_F(k_x,k_y)}\right). \tag{4.17}$$

Then, by using a theoretical description of a vortex for $f(x,y)$ (Equation 4.2), and making a real image of a vortex and using that for $s(x,y)$, one can make an attempt at determining ℓ for the system.

Figure 4.19a shows a real scan of a vortex from an LSCO sample, and Figure 4.19b shows the theoretical field a vortex would produce, imaged at $z = 2$ μm. The vortex is centred at the same location where the signal in the scan is at its maximum. Performing the deconvolution using the Lucy-Richardson algorithm (a built-in function in Matlab), we obtain the PSF as visible in Figure 4.19c.

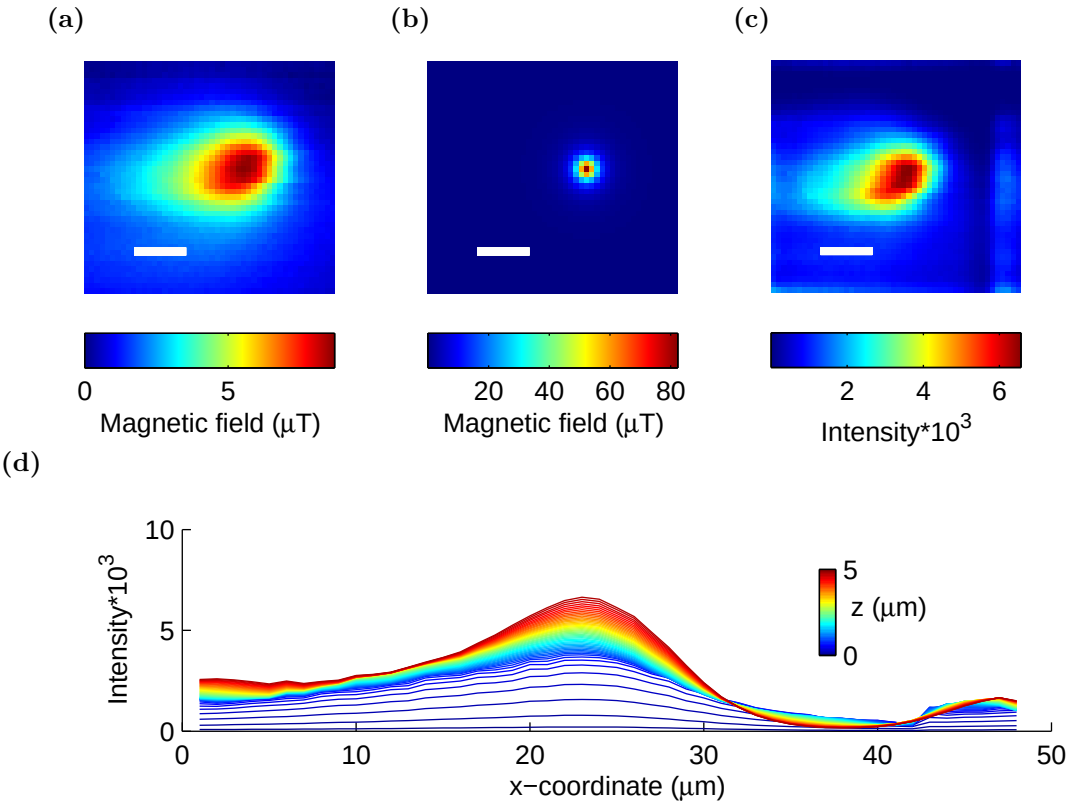

Figure 4.19: a) Scan of a vortex found on a LSCO surface. b) Theoretical field of a vortex at $z = 2$ μm. c) Calculated PSF at $z = 2$ μm. d) Value of the PSF along a line for different z.

One of the issues is determining which z to use for the theoretical vortex. This value should be equal to the actual scanning height, but the actual value is not easily verifiable. To see how the PSF changes depending on z, Figure 4.19d shows the value of the PSF along one spatial coordinate for different z-values. As we can see, the values increase as z increases. This makes sense, because as we increase z, the values of the theoretical vortex field become lower, meaning the PSF will have to compensate more to get the proper end result.

With this PSF, we can apply deconvolution to a larger image made with the same sensor. Figure 4.20a shows the original scan where the vortex from Figure 4.19 comes from. The deconvoluted image is shown in Figure 4.20b. The difference is clear; the deconvolution has removed most of the spread of the vortices. The d_v of the vortices is now roughly 5-6 μm, which corresponds to a scanning height of roughly 3 μm if we look at Figure 4.6g. This shows that the real scans and deconvolution process can closely match the simulations we did earlier.

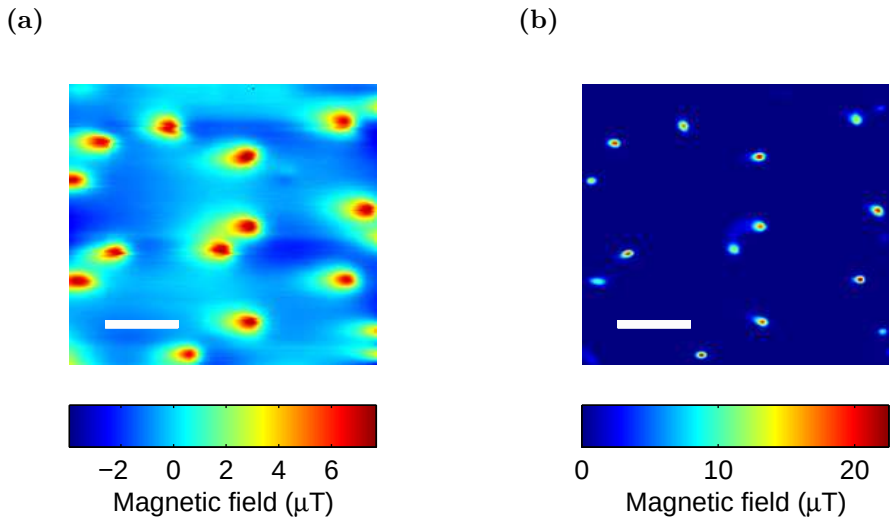

Figure 4.20: a) Scan of vortices at the surface of LSCO. b) Deconvoluted image. The scale bar indicates 40 μm.

4.5.2 Deconvolution of simulated vortices

Previously we have seen the result of convoluting simulated scans of vortices with a model pickup loop with different radius. Now we will have a look at how well we can restore the original again using deconvolution. Figures 4.21a and b show the original vortex (for $z = 5$ μm) and the same vortex convoluted with a pickup loop of radius $r_0 = 5$ μm, respectively. Figures 4.21c-e show the restored image using three of Matlab's built-in deconvolution functions: blind, Lucy-Richardson and regularized. For some details on how these algorithms work mathematically, see Refs. [97, 102–105].

We can see that each of the three deconvoluted images, Figures 4.21c-e, match the original closely. Looking at the graph in Figure 4.21g, we see that the blind algorithm performs best out of the three, closely followed by the Lucy-Richardson algorithm. The regularized deconvolution matches the original closely up to roughly $z = 9$ μm, where it starts to deviate significantly.

The erratic behaviour of the regularized algorithm is seen in Figure 4.21f. The image has clearly lost resemblance to the original in Figure 4.21a. What we see here are ringing artifacts, which are the result of the deconvolution process. They originate from the fact that at the edge of the image, there is a sharp change in signal strength (i.e., from any signal inside the image to no signal outside). The Fourier-series involved in the deconvolution algorithms creates a ripple effect, due to the Gibbs-phenomenon arising at these discontinuities.

Ringing artifacts can be reduced somewhat by smoothing out the edges and removing the discontinuity. However, this has already been done for the simulations above, and the effect is still present. More advanced methods of suppressing ringing artifacts exist (see, for example, Refs. [106–108]), but require a deeper mathematical analysis of the problems here. This is outside of the scope of this section, which is more aimed at showing what deconvolution does and how it can improve SSM.

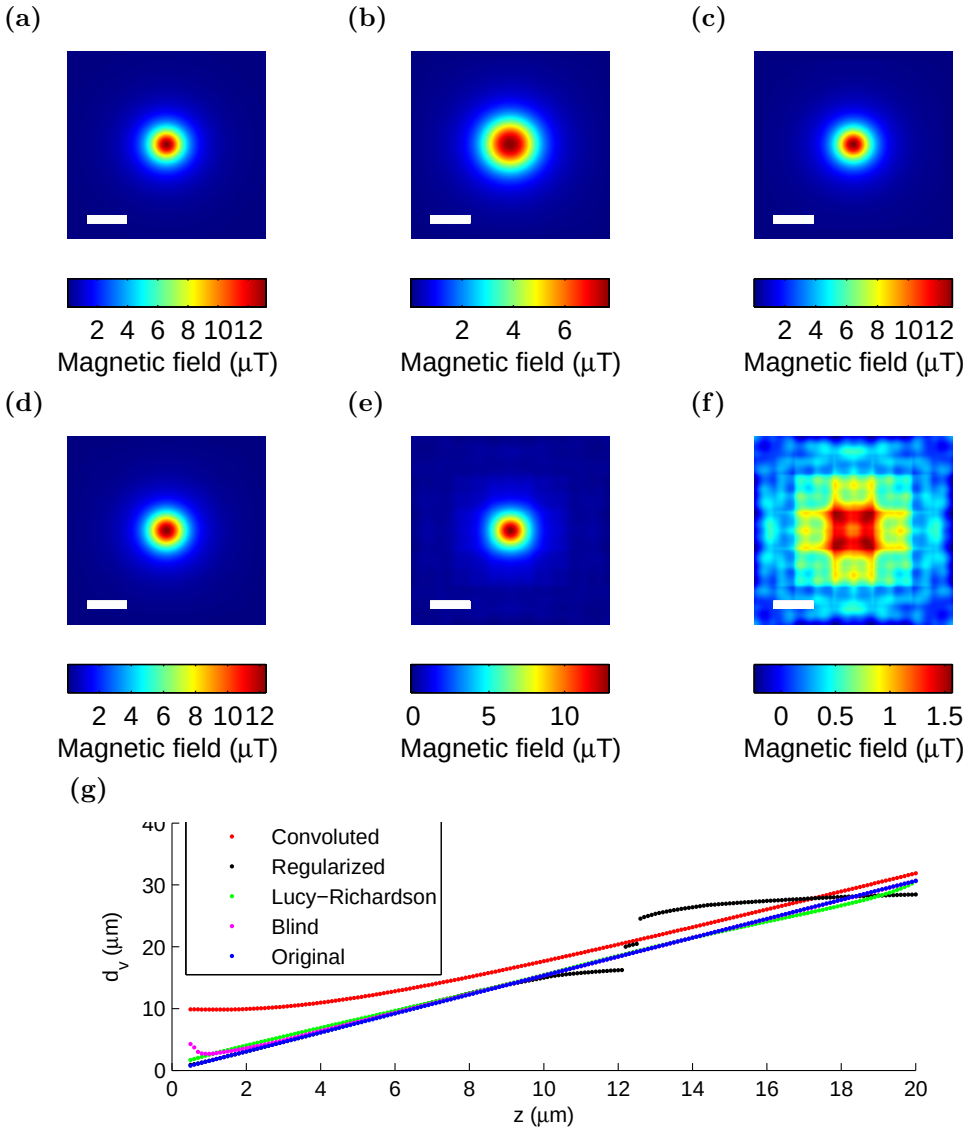

Figure 4.21: a) Original vortex simulation. b) Convoluted image with $r_0 = 5$ μm. c) Deconvoluted with the blind algorithm. d) Deconvoluted with the Lucy-Richardson algorithm. e) Deconvoluted with the regularized algorithm. f) Another deconvolution with the regularized algorithm, but at $z = 15$ μm. g) d_v as a function of z for the original signal, the convoluted signal, and the deconvoluted signal for each of the three deconvolution methods used.

4.5.3 Deconvolution of ferromagnetic surfaces

However, the problem with deconvolution is that the solution might not necessarily be unique. This is illustrated by using one of the ferromagnetic surface simulations from Section 4.4. Figures 4.22a and b show the original simulation and the convoluted image, respectively. Figure 4.22c and d shows the result of deconvolution using Matlab's regularized and Lucy-Richardson algorithms. Deconvolution using the blind method yielded nothing (i.e., a matrix of zeroes).

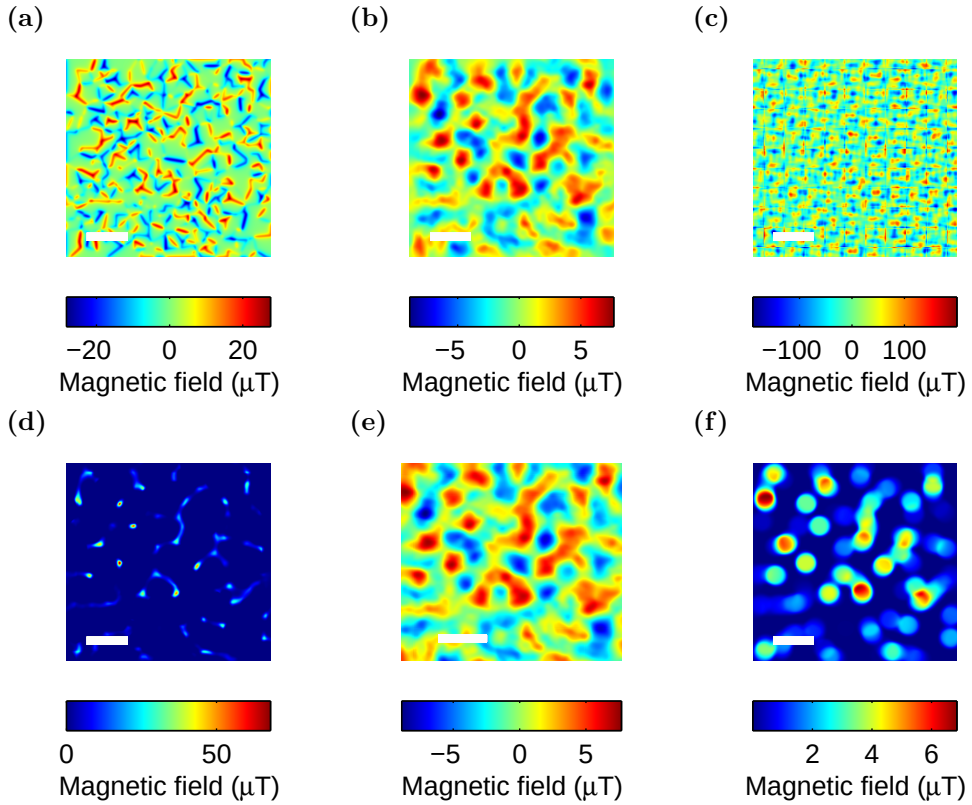

Figure 4.22: a) Simulated SSM scans of a ferromagnetic surface with in-plane magnetised domains at $z = 1$ μm. b) The simulation convoluted with a pickup loop with $r_0 = 5$ μm. c) The result of deconvoluting the image using the regularized algorithm. d) The result of deconvoluting the image using the Lucy-Richardson algorithm. e) Convoluting (c) again with a pickup loop of $r_0 = 5$ μm, with 5 μm removed from each edge. f) Convoluting (d) again with a pickup loop of $r_0 = 5$ μm.

As we can see, deconvolution with the regularized algorithm (Figure 4.22c) gives an image with no resemblance to the original. Performing the deconvolution with the Lucy-Richardson algorithm (Figure 4.22d) yields a very different result, which shows a small likeness to the convoluted image. Convoluting both again, using the same convolution process as done on the original image, we see something interesting.

Figure 4.22e shows the 'reconvoluted' image after deconvoluting with the regularized algorithm. Even though the deconvoluted image did not look like the original, this image is nearly identical to Figure 4.22b. The biggest difference is that, near the edges, the signal becomes very large, an artifact of the deconvolution process. For clarity, the edges have been removed from Figure 4.22e.

Conversely, reconvoluting the image after deconvoluting it with the Lucy-Richardson algorithm (Figure 4.22f) looks a lot less like Figure 4.22b. Ideally, like with the regularized algorithm, reconvoluting the image should yield the same result as before deconvo-

lution.

Going back to Figure 4.22c, it illustrates that deconvolution does not necessarily give a unique, or even representative, solution. In terms of convolution and deconvolution, this image is basically 'identical' to the original, in that they both produce nearly the same image when convoluted. Therefore, when deconvolution is used with experimental data, one has to be wary of this.

4.5.4 Deconvolution and noise

One aspect we have not discussed here is noise. As we have seen, especially with the ferromagnetic domains, deconvolution can be difficult enough without the addition of noise. The problem of noise becomes clearer when we look at Equation 4.1 and add in the noise ε:

$$s(x, y) = f(x, y) * \ell(x, y) + \varepsilon(x, y). \tag{4.18}$$

Normally, we would perform a Fourier transform, divide by ℓ_F and transform back to obtain f. However, if we do that in the presence of noise, we obtain

$$\frac{s_F(k_x, k_y)}{\ell_F(k_x, k_y)} = f_F(k_x, k_y) + \frac{\varepsilon(k_x, k_y)}{\ell_F(k_x, k_y)} \tag{4.19}$$

Now, if $\ell_F(k_x, k_y)$ has a value close to zero for certain frequencies, the noise contribution will become very large. To see how noise affects things we will do a similar analysis to what we did in Section 4.5.2, but this time adding noise before deconvolution (but after convolution). The noise will be Gaussian white noise with a mean of 0 and a standard deviation of 45 nT (somewhat larger than our own SSM setup, done for clarity purposes). Figure 4.23 shows the results of this process.

It is easy to see the differences that result from the added nosie. Most strikingly is the blind deconvolution (Figure 4.23d), which has such strong spiking values at the edges that the actual image is nigh invisible. Figure 4.23e shows the same image, but with 10 μm removed from each edge. The deconvoluted image is clearly there, representing the original in Figure 4.23a fairly well. The Lucy-Richardson algorithm does a lot better (Figure 4.23c), which is probably in part due to the algorithm having some basic noise handling methods.

Looking at Figure 4.23g, we see that the deconvolution becomes more and more erratic at higher z. This is due to the lower magnetic field strength, and hence a lower signal-to-noise ratio. Of course, part of the error in d_v is due to it being determined via code, whereas if done by hand, a much better value would be obtained, since the shape of the vortex is still clear enough below the noise (Figure 4.23f).

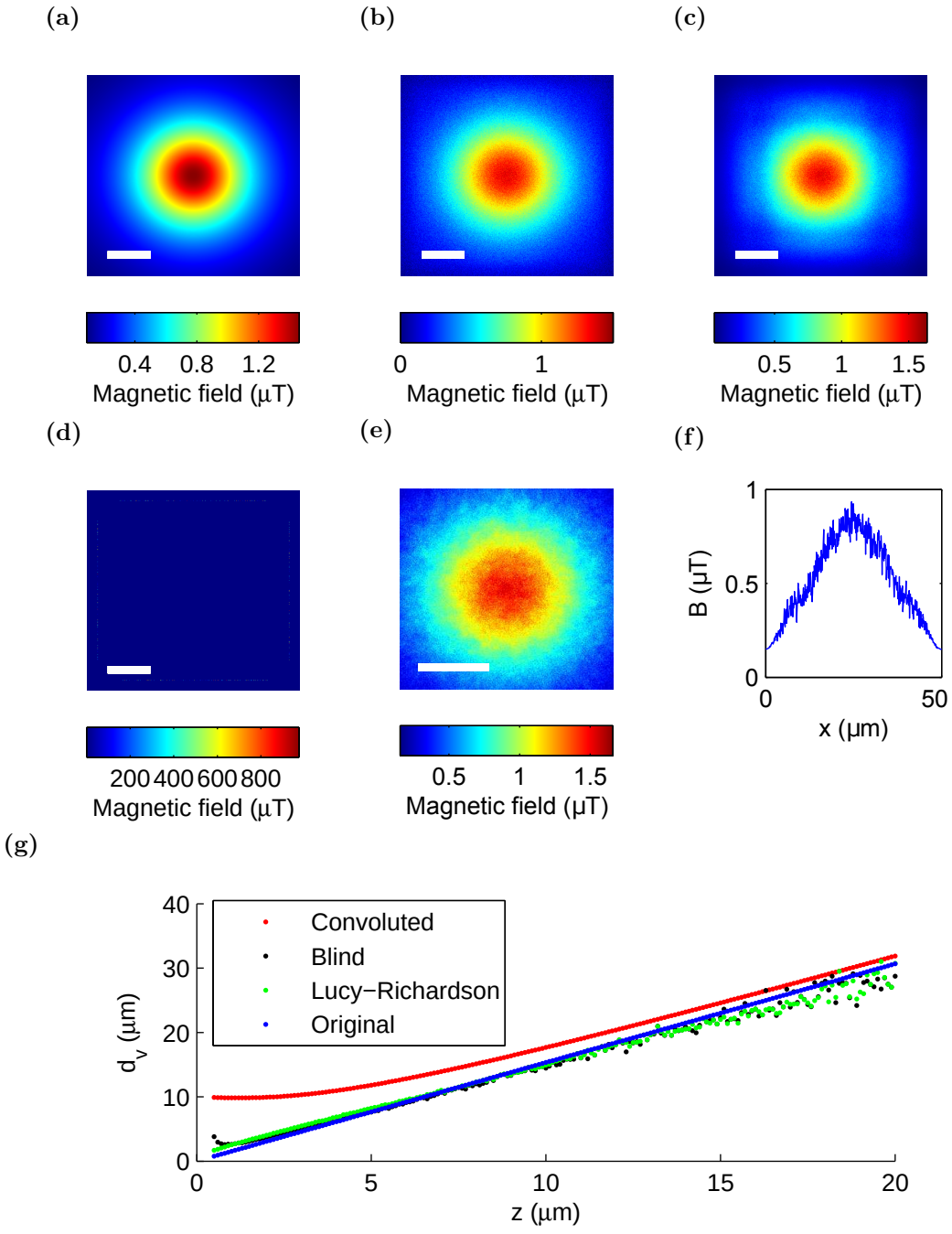

Figure 4.23: Deconvolution process with added noise. a) Original simulated at $z = 15$ μm. b) Convoluted with $r_0 = 5$ μm and added noise. c) Deconvoluted using Lucy-Richardson algorithm. d) Deconvoluted using blind algorithm. e) Same as (d), but with 10 μm removed from each edge. Scale bars indicate 10 μm. f) A line section through a Lucy-Richardson deconvoluted image at $z = 20$ μm. g) d_v as a function of z for the original signal, the convoluted signal, and the deconvoluted signal for the two deconvolution methods used.

4.6 Conclusions and discussion

In this chapter we have discussed the spatial resolution of SSM and the various factors influencing it. The influence of these factors was shown through simulations of several common magnetic features: vortices, dipoles and ferromagnetic domains. We have looked at how the magnetic field values change as z and r_0 change, but we have also seen how these two variables change SSM images visually.

Starting off with vortices, the simulations made use of a monopole approximation, which is a commonly used approximation for the field of a vortex. We have seen that increasing the sample-sensor distance z increased the apparent size of the vortex in a linear fashion, while decreasing the field values as $1/r^2$. Simulating pickup loops with increasing size also showed a decreasing signal. Combining the two factors showed that there is a region which is dominated by r_0 (low z), and a region that is dominated by z (high z).

If the effective radius of a pickup loop is known, the model can be used to give a confirmation on the value of z in an experiment. Since experiments are done in a cryostat, determining z is difficult due to not having any visual confirmation. But as we have seen throughout this chapter, knowing the actual value of z can be important to interpreting the data of an SSM image.

For this purpose, the model may need some improvement. Currently, it does not take the fact that the sensor is under an angle into account. As mentioned before, having the sensor under an angle causes the system to pick up other components of the magnetic field besides the z-component. Beyond that, the equation we used to approximate the vortex is only valid for $z \gg \lambda$. If, in future, the system is upgraded or replaced by something that can approach and scan on length scales on the order of λ, this model can no longer be used and a new model will have to be set up.

We also had a quick look at dipoles, and showed that ferromagnetic structures can be modelled as a collection of dipoles. Although SSM may not be able to resolve the structure properly in certain cases, combining it with AFM creates a powerful tool to analyse the magnetic behaviour of micrometre scale ferromagnetic structures. From what we have seen, having an out-of-plane magnetisation direction is optimal for a structural analysis, due to the sharp gradient that appears between the structure and the non-magnetic surroundings. Since our own SSM setup comes with a magnetic field coil that can apply a field in this direction, it can magnetise a sample in this direction, thus allowing some structural analysis where methods like AFM may not be sufficient.

We used the simulation of magnetic structures as a stepping stone to the simulation of ferromagnetic domains. The simulation was simplified by forgoing the actual physics that are involved in forming the domains. Instead, the domains were randomly created and magnetised, with the domain size simply controlled by the number of domains present.

We have looked at domain structures and how they are influenced by the scanning height. At larger z values, the domain structure becomes lost as the fields average out. As expected, this is accompanied by a sharp ($1/r^3$) decrease of the magnetic field strength.

Comparing in-plane and out-of-plane magnetism showed that the two are only distinguishable at low z; at higher z, the fields are averaged out and telling one magnetisation direction from the other becomes impossible. As we have seen with the ferromagnetic structure before, out-of-plane magnetisation allows for a clearer image of the actual domain structure than in-plane magnetisation does. However, drawing conclusions on the domain structure in general should be done with care. Just as the simulations at high z values showed an averaging, resulting in fewer but larger domains, so can a real SSM im-

age, depicting some domain structure, be an average over yet smaller domains (possibly sub-resolution).

B_{RMS} is a good figure of merit for the magnetic field of a surface showing a domain structure. We have seen that it is linearly dependent on the magnetisation, with the coefficient depending on the orientation of M. This allows for magnetisation measurements with SSM, but only if the coefficient is known.

Although including proper physical models for creating the domains would improve the simulation, the question is more about how much. The aim of these simulations was not to learn more about domains themselves, how they form and behave, but mostly about how their resultant magnetic field appears when imaged with SSM and what we can deduce from that. One can argue that having proper underlying domain physics might not be necessary for that purpose. For example, a typical domain wall has a thickness of $\sim$100 unit cells [109], which is less than half a pixel in these simulations. Having the proper physical models in place would definitely create more realistic domains (in terms of size and shape), but will probably not change the visual result too much from what we have seen, which was our end goal in the first place.

Beyond that we have discussed the method of deconvolution. Due to the finite size of the pickup loop, the measured field will always be an average over a certain area. This obscures small features in scans and worsens the spatial resolution. Deconvolution algorithms were used to try and improve both simulations with convolution as well as a real scan.

We went on to show some of the basics of deconvolution and what it can do for SSM. We used three of Matlab's built in deconvolution functions and looked at how they resolved the convolution problem. Part of the problem is determining (if possible) the PSF. We have done this for a real scan using the Lucy-Richardson algorithm, and used it to deconvolve an image of vortices. The result showed a clear difference, reducing the size of the vortices down to a size more resembling a theoretical prediction.

In an experimental situation, this means that the PSF will have to be determined for each sensor (and even every scanning session). Therefore, one needs to have access to vortices to calculate the PSF, even if the material does not naturally contain vortices (like ferromagnetic materials). One can solve this by depositing a small area of superconducting material (e.g., Nb) on the sample of interest, and include it in the scans to be able to determine the PSF and perform the deconvolution.

We also looked at how noise impacted the deconvolution process. The problem with noise is that it can create large values in the frequency domain due to the division with ℓ_F (Equation 4.19). To solve this (or at least, reduce its effect), one will have to use more sophisticated algorithms than the ones we have used here.

5. LMO thin films at different oxygen pressures

This chapter will discuss the experiments performed on the LMO/STO system. LMO thin films were deposited on STO substrates, varying different parameters to analyse their influence on the system.

5.1 Growth

Two series of sample were made for the experiments in this project. The samples used for the pressure series (this chapter) were prepared by the NUSNNI group of the National University of Singapore. The samples for the Au-capped experiments (Chapter 6) were prepared at the University of Twente. All samples were prepared on 5x5x0.5 mm^3 TiO_2-terminated STO(001) substrates using Pulsed Laser Deposition (PLD) (the method for preparing the STO substrates is described in Ref. [110]). Deposition was performed at 750° C using a polycrystalline stoichiometric LMO target. The laser fluency was 1.8 J/cm^2 with a repetition rate of 1 Hz. The LMO was grown layer-by-layer, which was controlled using in-situ Reflection High-Energy Electron Diffraction (RHEED). All samples in the pressure series are 25 uc, the thickness of the samples for the Au-capping experiments are specified in Chapter 6. The gating samples were grown at a oxygen partial pressure of 10^{-2} Torr. After deposition, the samples were cooled under the deposition pressure.

5.2 XRD data

X-ray diffraction (XRD) analysis was performed on all samples to gain information about the crystal structure. This will tell us if the grown films are strained or relaxed, which can influence the magnetic ordering as explained in Section 3.5. The following 2θ scans were made using a PANalytical X'pert Multi-Purpose Diffractometer.

Figure 5.1 shows 2θ XRD scans around the STO(002) peak. The scans were made around the STO(002) peak, which is clearly visible. The splitting that can be seen in that peak is due to the Cu K_α doublet, with wavelenghts $\lambda_{K\alpha 1} = 0.1541$ nm and $\lambda_{K\alpha 2} = 0.1544$ nm, that is produced by the X-ray source of the XRD. It is not present in the scan for the $P_{O_2} = 10^{-2}$ Torr sample, because a monochromator was used there. For the samples between $P_{O_2} = 10^{-2}$ Torr and $P_{O_2} = 3 * 10^{-6}$ Torr, we can see a broad LMO(002) peak on the left hand side of the STO peak.

Furthermore, we can see that the LMO peak changes position, indicating a change in the out-of-plane lattice parameter c depending on P_{O_2}. Figure 5.1b shows c as a function of P_{O_2}, as obtained from these XRD scans. c first decreases with increasing pressure, down to roughly 3.92 Åat $P_{O_2} = 10^{-4}$ Torr, after which it increases again. This indicates that any changes in magnetic or electric properties could be in part due to changes in strain.

To get more details about the in-plane lattice parameters, asymmetrical reciprocal space maps (RSMs) were made using a PANalytical X'pert Materials Research Diffractometer. Figure 5.2 shows the RSMs of the $P_{O_2} = 10^{-2}$ Torr sample (RSMs for the other

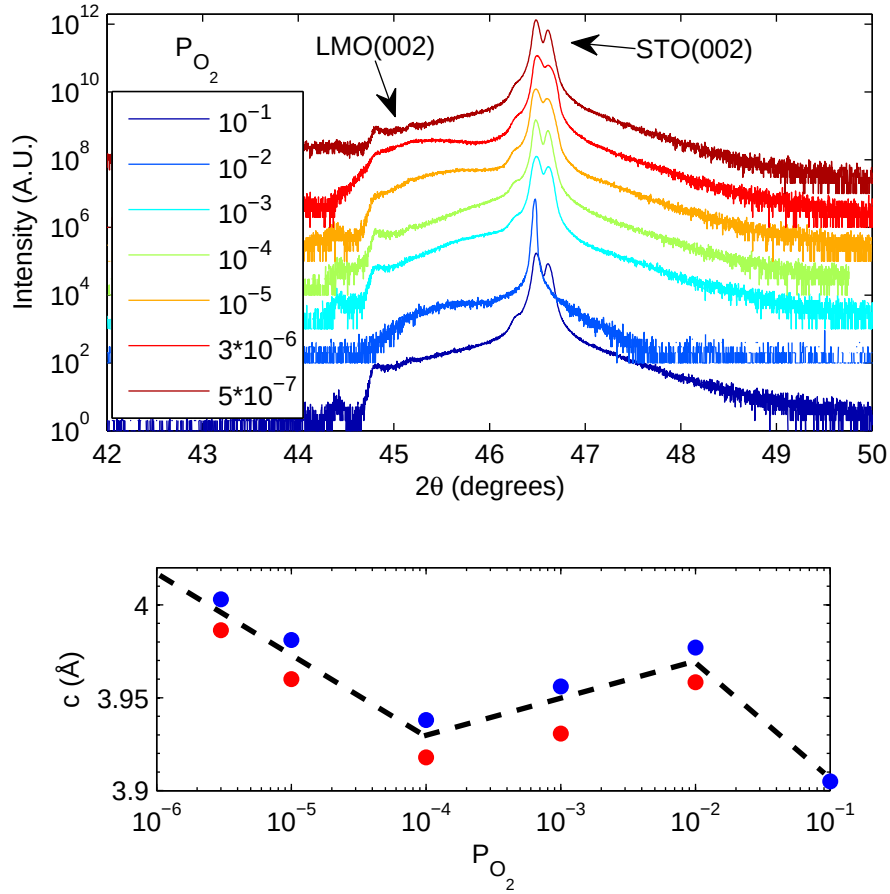

Figure 5.1: a) 2θ scans of the samples in the pressure series. Scans are offset for clarity. b) Out-of-plane lattice parameter c as a function of P_{O_2} from the 2θ scans (red) and the RSM data.

samples can be found in Appendix B). The RSMs were made around the STO(103) peak, which is clearly visible in the figures. Directly below it we can see the LMO(103) peak. It is stretched out vertically due to the small film thickness. The peak being directly below the STO(103) peak indicates that these samples are epitaxially grown on the STO substrate, thus matching the in-plane lattice parameter of 3.905 Å. The diagonal streak that is visible in the RSMs is due to the finite width of the detector.

The RSMs also allows us to obtain the out-of-plane lattice parameter c, which is shown in Figure 5.1b in blue. Though maybe not as clear as the other samples, the LMO(103) peak of the $P_{O_2} = 10^{-1}$ Torr in the RSM data (Figure B.1, Appendix B) seems to be centred on the STO(103) peak, meaning the c-value of that sample is 3.905 Å.The overall behaviour of c is the same with both methods, the only difference being a small but constant offset of roughly 0.02 Å, which is most likely due to small differences between analyses.

This behaviour matches the data from Marton *et al.* [74], including the drop of c to 3.905 Å at high pressure, although they find larger values for c than we do here, by about 0.05 Å. The parameters used in their study are different from ours: their laser pulse repetition rate was 10 Hz, and deposition was done at 600° C. The lower temperature might result in a lower oxygen uptake by the thin film, leading to a higher c compared to our samples at the same pressure.

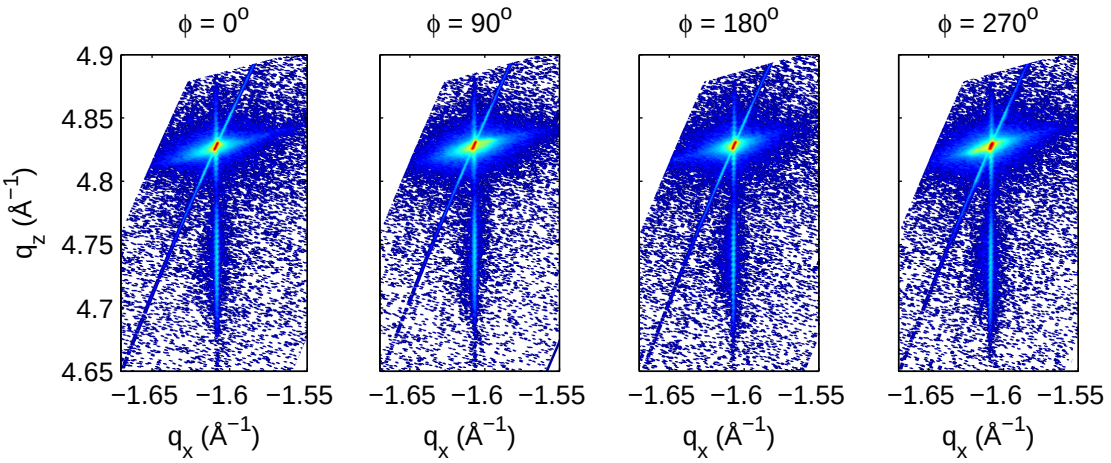

Figure 5.2: Reciprocal space map of the $P_{O_2} = 10^{-2}$ Torr sample around the STO(103) peak.

5.3 VSM data

To get an idea about the magnetic properties of the samples, measurements were done in a vibrating sample magnetometer (VSM). Figure 5.3a shows the magnetisation of each sample as a function of temperature. First of all, we can see that each sample transitions into the FM state at approximately 100 K, except for the $P_{O_2} = 10^{-1}$ Torr sample, which begins transitioning at roughly 175 K.

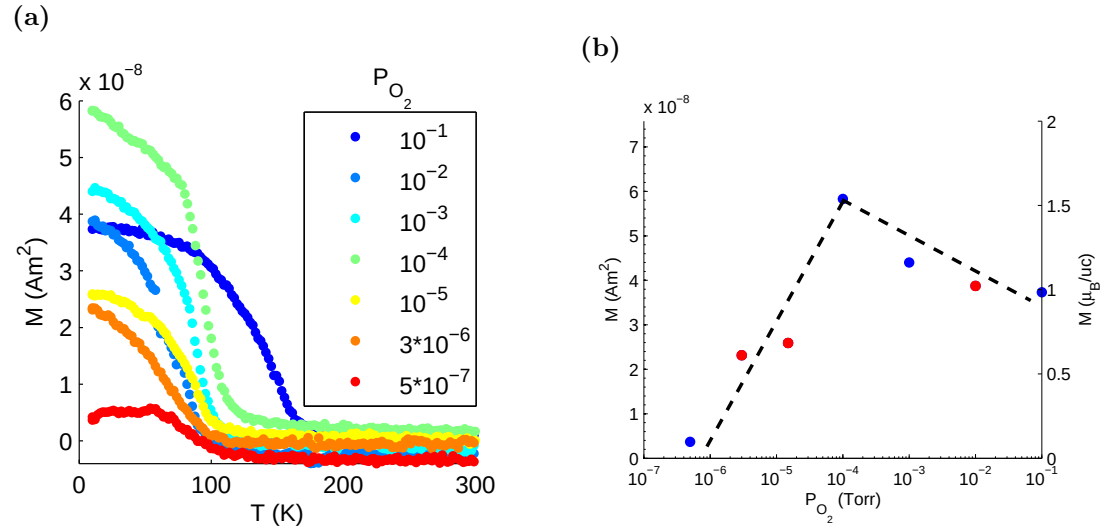

Figure 5.3: a) Magnetic Moment M versus Temperature T measurements. b) M at $T = 10$ K versus P_{O_2}. Samples marked red may have had contaminants.

Secondly, we see that the strength of the FM does not increase or decrease monotonically, but rather peaks at $P_{O_2} = 10^{-4}$ Torr. This is shown more clearly in Figure 5.3b, where the magnetisation at $T = 10$ K is shown as a function of P_{O_2}. Looking back at Figure 5.1b, it seems likely that this behaviour is linked to the change in c. The same goes for the different transition temperature for the $P_{O_2} = 10^{-1}$ Torr sample, corresponding to its sudden decrease in lattice parameter. It could be that a different $La_xMn_xO_y$ phase has formed, with slightly different magnetic and structural properties.

Marton *et al.* also measured the higher Curie temperature at high deposition pres-

sure, but whereas we see a drop in magnetisation for pressures higher than 10^{-4} Torr, they observe that the magnetisation at $P_{O_2} = 10^{-1}$ Torr is higher than at lower pressures [74].

For some more information about the magnetic properties, we can look at M while sweeping an applied magnetic field H. Figure 5.4 shows the M versus H curves for each sample. Something that is immediately clear is that in some samples ($P_{O_2} = 10^{-2}$, 10^{-5} and 10^{-6} Torr) there are multiple saturation plateaus. This means that there is more than one ferromagnetic material present in these samples. It could be an indication of different LMO phases, however, it seems more likely that it is due to contaminations (for example, iron particles, silver paint or contaminants from tools).

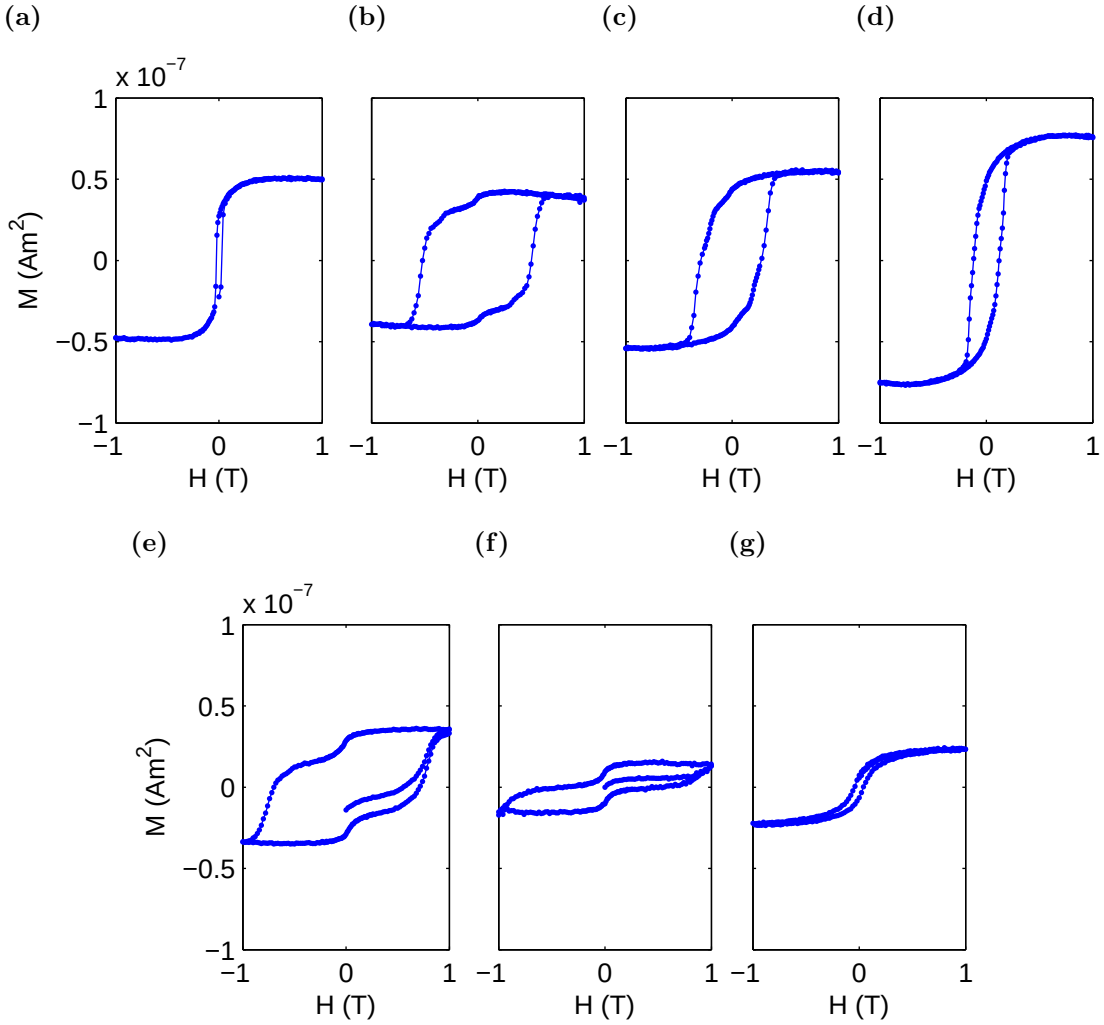

Figure 5.4: M versus H measurements for the samples in the pressure series: a) $P_{O_2} = 10^{-1}$ Torr; b) $P_{O_2} = 10^{-2}$ Torr; c) $P_{O_2} = 10^{-3}$ Torr; d) $P_{O_2} = 10^{-4}$ Torr; e) $P_{O_2} = 10^{-5}$ Torr; f) $P_{O_2} = 3 * 10^{-6}$ Torr; g) $P_{O_2} = 5 * 10^{-7}$ Torr.

Something else that can appear in (anti)ferromagnetic films is exchange bias. This occurs at the interface between an AF layer and an FM layer, where strong exchange interactions between the two layers can cause pinning of the spins of the FM layer. Because of this, the required magnetic field to reverse the magnetisation will be higher, causing a shift along the H-axis of the M versus H curve. However, since the curves in Figure 5.4 are not shifted along the H-axis, exchage bias does not seem to be a factor here.

As for the other samples, we again see the strongest magnetisation for the $P_{O_2} = 10^{-4}$

Torr sample (Figure 5.4d). It is hard to draw any conclusions about trends in the magnetisation or the coercive field due to the secondary phases and/or contaminants.

5.4 SSM data

To learn more about FM in LMO, the samples were scanned using SSM. Using SSM data we can have a look at the strength of the FM at a local level, and see how it changes depending on the oxygen pressure.

Figure 5.5 shows SSM scans of a sample grown at $P_{O_2} = 10^{-2}$ Torr. The domain structure is clearly visible, although it is not possible to discern between in-plane or out-of-plane FM. As we have discussed in Chapter 4, this is due to the limited spatial resolution. The same holds for the average domain size, in that we cannot say anything about it other than that domains are no larger than what we see here (a few micrometre across).

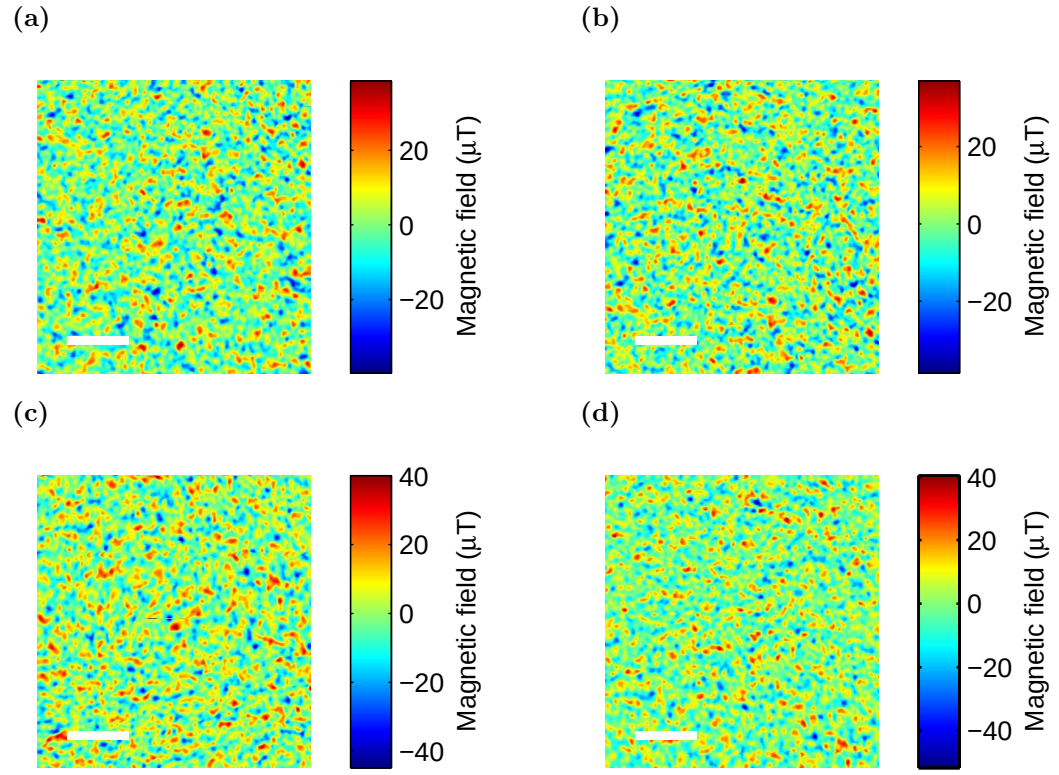

Figure 5.5: SSM scans of the $P_{O_2} = 10^{-2}$ Torr sample in different areas. The scale bar indicates 100 μm.

Figures 5.5b, c and d show scans made on the same sample at different locations. Both the domain structure and the overall magnetic field strength (as indicated by the colour bars) is similar, indicating that the sample surface is homogeneous in terms of magnetic features.

Figure 5.6 displays a representative scan for the other 6 samples in the pressure series ($P_{O_2} = 10^{-1}$; 10^{-3}; 10^{-4}; 10^{-5}; $3 * 10^{-6}$; $5 * 10^{-7}$ Torr). Overall, the domain structure remains the same throughout the series, meaning that a change in deposition pressure does not change the domains in a way visible to our SSM. It might be possible that changes occur on a smaller scale, but are not visible due to the limited spatial resolution.

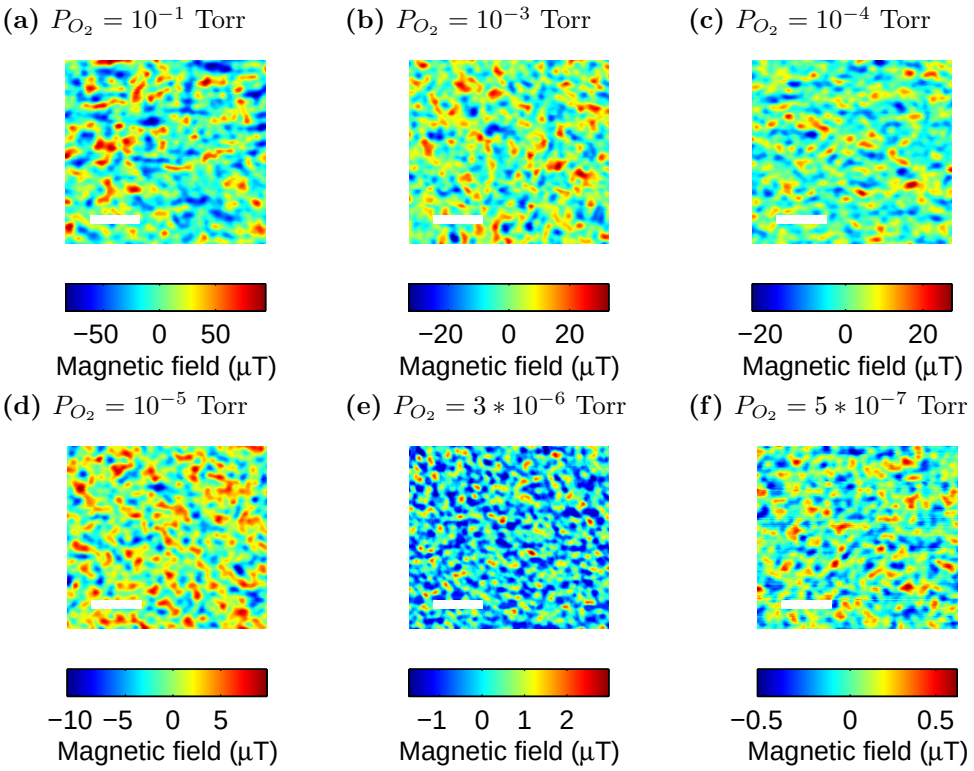

Figure 5.6: SSM scans of 25 uc LMO films deposited at different P_{O_2}: a) 10^{-1} Torr, b) 10^{-2} Torr, c) 10^{-3} Torr, d) 10^{-5} Torr, e) $3 * 10^{-6}$ Torr, f) $5 * 10^{-7}$ Torr. The scale bars indicate 50 μm.

Looking at the colourbars in Figure 5.6, we can see a decrease in magnetic field strength (from roughly ± 120 μT in Fig. 5.6a to ± 0.8 μT in Fig. 5.6f). To get a more clear picture of what is happening, we can plot B_{RMS} as a function of P_{O_2} in Figure 5.7.B_{RMS} varied by approximately 5-10% from scan to scan of the same sample, so multiple scans on different areas were made to get an average value of B_{RMS} for each sample. As mentioned in Chapter 2, the pickup loop size is not the same for all sensors, which means the resulting B_{RMS} values are not absolute. To correct for this somewhat, we set the B_{RMS} value of the $P_{O_2} = 10^{-4}$ Torr sample as a baseline. Whenever we installed a new sensor, a few scans of that sample were made. The ratio between the B_{RMS} values gained by using a new sensor and the baseline B_{RMS} value can be used to correct for the difference in pickup loop sizes.

From Figure 5.7, we can see that, at first, as P_{O_2} increases, B_{RMS} increases following a power law (i.e., of the form $B_{RMS} = a \cdot P_{O_2}^{bx}$, indicated by the red line). Then it saturates around $P_{O_2} \approx 10^{-2}$ Torr to a value of $B_{RMS} \approx 4$ μT (indicated in black). Then, at $P_{O_2} = 10^{-1}$ Torr, B_{RMS} suddenly seems to increase again. The green data point in Figure 5.7 indicates uncalibrated data, which, at the same time, serves to give an idea of the error in the value of B_{RMS}.

Other research into pressure-dependent stoichiometry of LMO showed that lower deposition pressures result in the La/Mn ratio approaching unity, in combination with a decreasing magnetic moment [74]. This is in line with what we see: towards lower pressure, the magnetic intensity decreases, which can be explained as more Mn ions being in the Mn^{3+} state and superexchange being the dominant interaction. At higher pressures, when the material deviates from stoichiometry (and vacancies appear), more and more Mn ions become Mn^{4+}, leading to higher magnetic intensity as a result of double exchange.

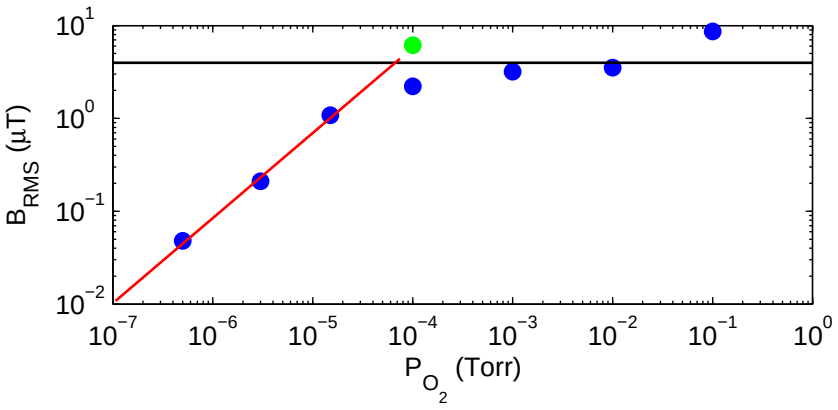

Figure 5.7: Log-log graph of B_{RMS} versus deposition oxygen pressure. The green data point indicates uncalibrated data and serves as an indication of the margin of error. The horizontal black line roughly indicates the saturation value of B_{RMS}, the red line is a guide to the eye for the linear region of the graph.

Physically speaking, it makes sense that there is a maximum value to the magnetism that can arise from changing the stoichiometry. Changes in stoichiometry will lead to changes in the amount of Mn^{4+}, which results in changes in magnetic intensity. However, as seen in Figure 3.8, there are optimal values for the amount of Mn^{4+}, since double exchange (which leads to FM) happens in mixed valence states.

The increase in B_{RMS} at $P_{O_2} = 10^{-1}$ Torr is likely related to the sharp change in the out-of-plane lattice parameter noted in Section 5.2. As we have discussed in Chapter 3, structural changes are related to the magnetic properties of the film. Marton *et al.* similarly noticed an increase in magnetisation in VSM measurements on LMO films grown under high pressure [74].

Interestingly, in another experiment done by Zhao *et al.*, thin films deposited with molecular beam epitaxy (MBE) showed increasing stoichiometry with increasing pressure [111], which seems to contradict our findings and those of Marton *et al.* A tentative explanation is that it could be due to the different deposition methods involved. PLD deposits material in short, highly energetic bursts, whereas MBE deposits a steady stream of material at lower energies [112]. It could be that when using MBE at low pressures, one deposits $LaMnO_{3-\delta}$, and stoichiometry is increased with increasing pressure. Conversely, PLD deposits stoichiometric LMO at low pressures, and overdopes oxygen ($LaMnO_{3+\delta}$) at higher pressures.

Chainani *et al.* found that a higher oxygen content in LMO decreases the bandgap (from 1.3 eV for $LaMnO_3$ to 0.24 eV for $LaMnO_{3.13}$) [86]. This means that the charge transfer starts at lower thickness values (Section 3.6), leading to more electrons transferred for a certain thickness. This in turn means there is a higher amount of Mn^{4+}, leading to a higher FM intensity. Combined with the notion that lower P_{O_2} leads to more stoichiometric LMO [72,74], this is a possible explanation for the observed magnetic behaviour as function of P_{O_2}.

Comparing to our VSM data, Figure 5.7 seems to show different behaviour than what we have seen in Section 5.3. There we saw a peak in the magnetisation at $P_{O_2} = 10^{-4}$ Torr, whereas here, we see B_{RMS} increasing monotonically. Of course, in VSM we applied an up to ± 1 T field during the measurement, whereas in the SSM, we had no magnetic surroundings (other than Earth's magnetic field). However, in Chapter 4 we saw that there is a linear relationship between B_{RMS} and M (Figure 4.17c), which means Figures 5.7 and 5.3b should show the same overall behaviour. However, from

Figure 4.17c we can see that different magnetisation directions have different coefficients relating M to B_{RMS}. This means that if the preferred alignment of the spins in the LMO changes (from in-plane to out-of-plane, for example), B_{RMS} can increase even if M decreases.

5.5 Resistivity data

As part of the characterisation of the LMO films, electrical transport measurements were performed. These measurements were carried out in a Quantum Design Physical Property Measurement System (PPMS).

For each sample in the pressure series, resistance versus temperature ($R-T$) measurements were done. The standard Van der Pauw method was used to measure the resistance while sweeping the temperature. The results of these measurements are shown in Figure 5.8.

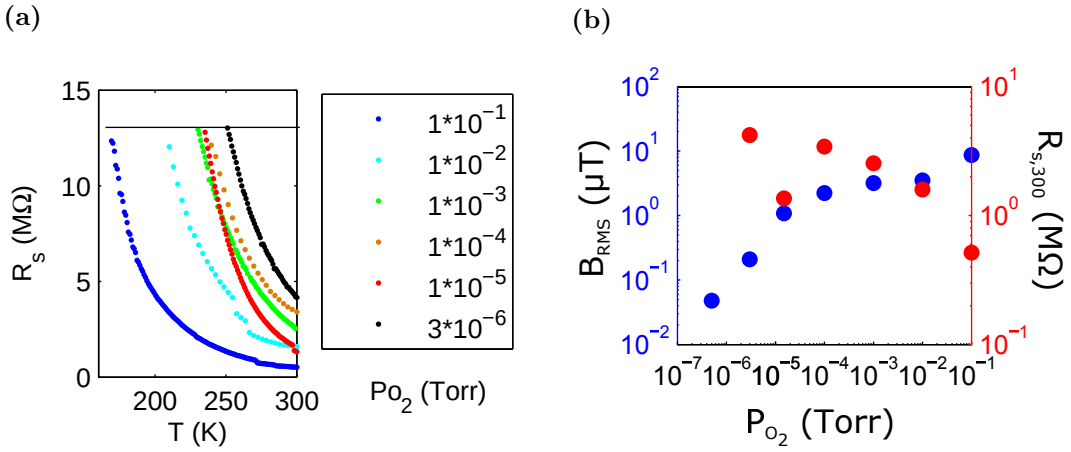

Figure 5.8: a) Sheet resistance R_S versus Temperature T measurements. b) R_S at $T = 300$ K (red) and B_{RMS} versus P_{O_2}.

The individual curves clearly show semiconducting resistance behaviour, and the overall resistance values decrease with increasing pressure. Both observations are in agreement with results from earlier studies [75, 113, 114]. The resistance curve for the 10^{-5} sample shows somewhat different behaviour: it has a lower resistance at $T = 300$ K than one would expect, and crosses the $P_{O_2} = 10^{-2}$ and 10^{-3} Torr samples' curves.

The resistance values at $T = 300$ K against P_{O_2} are shown in Figure 5.8b. The resistance appears to saturate at lower pressures, which is in line with the expected increased stoichiometry at lower pressures (since stoichiometric LMO is an insulator). However, when compared to the magnetic intensity, the resistance shows opposite behaviour: the magnetic intensity saturates at higher pressures, whereas the resistance saturates at lower pressures. This indicates that transport properties and magnetic properties are not correlated. Figure 5.8b again shows the odd behaviour of the $P_{O_2} = 10^{-5}$ Torr sample.

The resistivity of the $P_{O_2} = 5 * 10^{-7}$ Torr sample, however, differed largely from the curves in Figure 5.8, as shown in Figure 5.9. Here we see an increasing resistance as function of T, as opposed to decreasing. The curves are reminiscent of the resistivity curves of reduced STO (for example, see Ref. [115]), leading us to believe that the STO substrate was reduced during sample preparation and is now contributing to the conductivity of the sample.

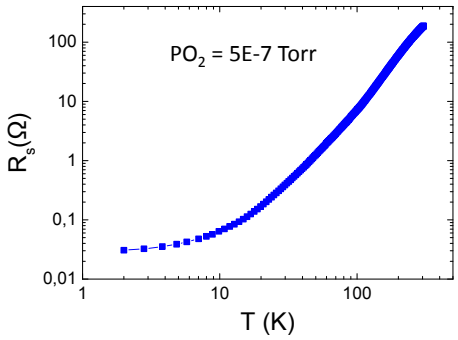

Figure 5.9: R versus T curve of the 10^{-7} sample.

5.6 Detection of contaminants

One sample, however, showed radically different behaviour. That sample was grown at $P_{O_2} = 10^{-6}$ Torr, and a scan of it is shown in Figure 5.10, together with a scan of $P_{O_2} = 3 * 10^{-6}$ Torr for comparison.

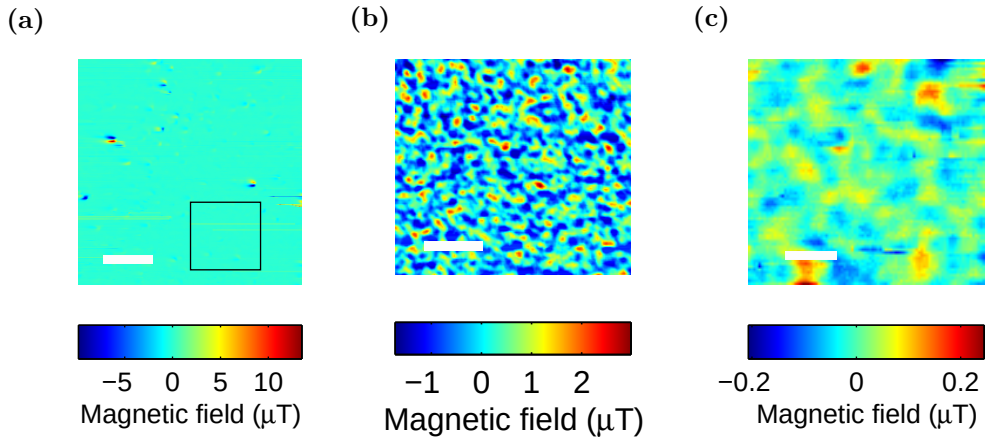

Figure 5.10: a) Scan of the $P_{O_2} = 10^{-6}$ sample. Scale bar indicates 100 μm. b) Scan of the $P_{O_2} = 3 * 10^{-6}$ sample. Scale bar indicates 50 μm. c) Zoom of the area indicated in black in (a). Scale bar indicates 20 μm.

At first glance, it would seem the system manifests magnetism in the form of dipoles. Similar results were seen at LAO/STO interfaces Bert *et al.* [90,116]. This would be odd, however, since the samples at higher and lower pressure show large-scale FM domains (see Figures 5.6d-f). Furthermore, upon close inspection, it seems that in areas where there are no visible dipoles, the domain structure is visible (see Figure 5.10c).

This leads us to believe that the dipoles might be due to contamination of the surface. Using Atomic Force Microscopy, the surface was analysed to see if any contaminants could be found. The scans are shown in Figure 5.11).

The scan shows particles on the surface of the LMO. The particles are roughly 3-5 μm across, and vary in height from approximately 200 nm to 1 μm. Looking at the shape of these particles, they do not appear to be dust or dirt particles: the shapes are very angular. The close-up scan of one of the particles seen in Figure 5.11b shows this clearly.

A likely possibility is that the particles are contaminants from the PLD process. For example, when cleaning the sample holder by grinding, metallic particles might be left on the holder if not cleaned properly. These could then come off and land on the film

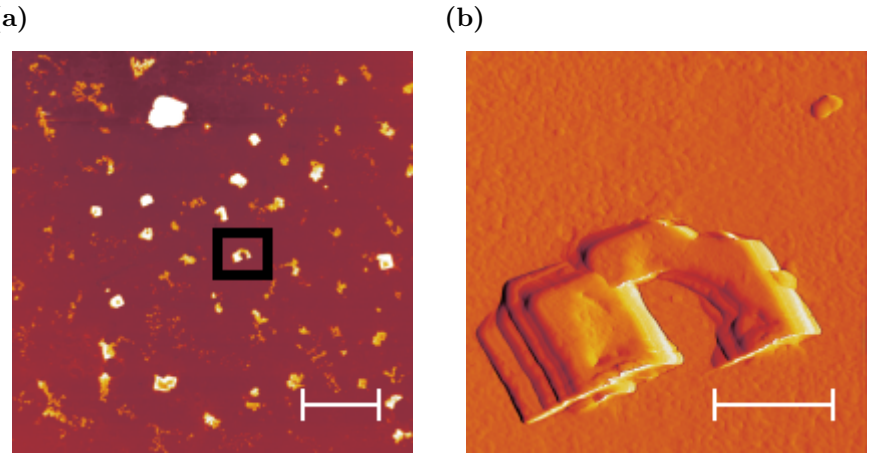

Figure 5.11: a) Atomic Force Microscopy scan of the surface of the 10^{-6} sample. Contaminants are clearly visible. The scale bar indicates 10 μm. b) Enlarged view of the boxed area in (a). The structure is approximately 200 nm high. The scale bar indicates 1 μm.

during PLD.

Inadvertedly, this sample does show the capability of the SSM to discern between contamination and film. The contaminations show up as dipole fields, whereas the underlying film is still visible as its FM domain structure. Unfortunately, the contaminations covered the film too much for any meaningful data to be extracted.

5.7 Conclusions and discussion

In this chapter we have looked at LMO thin films deposited at various oxygen pressures, and how the properties of these films change. XRD measurements showed that the out-of-plane lattice parameter has a local minimum around $P_{O_2} = 10^{-4}$ Torr (3.93 Å), and drops sharply between $P_{O_2} = 10^{-2}$ and 10^{-1} Torr to 3.905 Å. Both 2θ measurements and RSMs showed the same behaviour.

This behaviour of c is reflected in the VSM measurements, which show a local maximum in the saturation magnetisation at $P_{O_2} = 10^{-4}$ Torr of approximately $5.9 * 10^{-*}$ Am^2. The sudden change in lattice parameter of the $P_{O_2} = 10^{-1}$ Torr sample was accompanied by a rather large increase in the Curie temperature: 175 K for this sample compared to about 100 K for the other samples.

From literature we know that increasing the oxygen deposition pressure decreases the La/Mn ratio. A possible scenario is that as the ratio decreases, the amount of Mn^{4+} increases as La-vancancies donate holes to Mn^{3+}. At $P_{O_2} = 10^{-4}$ Torr, an optimal value of the Mn^{4+}/Mn^{3+} ratio is reached, leading to a maximum in double exchange and therefore the strength of the magnetism in LMO. As the La/Mn ratio decreases further, and Mn^{4+}/Mn^{3+} keeps increasing to where Mn^{4+} ions start showing superexchange interactions with each other, due to the lack of Mn^{3+} ions in the lattice. This then results in a decrease in the magnetisation.

Moving to the SSM measurements, we saw a clear magnetic domain structure present on the surface of the LMO thin films. Due to our spatial resolution, we are unable to make a real statement about the domain size or shape, other than that they are most likely sub-resolution. The domain structure was present in all samples and appeared constant throughout the series, as well as being constant across multiple locations on a single sample.

The magnetic field, measured as B_{RMS}, showed behaviour reminiscent of a power law, increasing by roughly 2 orders of magnitude from $P_{O_2} = 5*10^{-7}$ Torr to $P_{O_2} = 10^{-4}$ Torr, before saturating to a value of approximately 3 μT. Then, at $P_{O_2} = 10^{-1}$ Torr, another increase in B_{RMS} appeared, which is likely related to the behaviour of this sample we saw in the XRD and VSM measurements.

What is interesting is that the VSM and SSM measurements do not seem to match concerning the overall trend in magnetisation. The VSM measurements showed a clear peak at $P_{O_2} = 10^{-4}$ Torr, whereas B_{RMS} determined from the SSM scans increased monotonically. From the simulations in Chapter 4, we know that there is a linear relation between M and B_{RMS}. A possibility is that as the lattice changes due to increasing oxygen deposition pressure, spins may tend to align more and more along the out-of-plane direction (due to changes in the magnetic anisotropy). From Figure 4.17c we know that out-of-plane magnetisation will have a higher B_{RMS} at the same M. This means that B_{RMS} can increase even though M decreases.

To increase our understanding of these samples, it would be worthwhile to analyse the elemental composition of the films, for example with X-ray photoelectron spectroscopy (XPS) or Rutherford backscattering spectroscopy (RBS). Determining the ratio between Mn^{3+} and Mn^{4+} and the ratio between La and Mn will let us see how the doping levels change with changing P_{O_2}, which in turn give us an idea about the balance between superexchange and double exchange in LMO. Transmission electron microscopy (TEM) combined with EELS can also show the valency of the Mn ions, in combination with structural data of the interface.

6. LMO thin films with Au top layer

As discussed in Chapter 3, suggestions have been made of an electronic reconstruction scenario occuring in LMO thin films. To provide evidence for (or against) this, samples were created that would allow for a gate voltage to be applied to them. The idea being that, when a gate voltage is turned on, the band structure bends upwards, which causes the electron transfer to start at a lower critical thickness (see Figure 6.1a).

This way, one could take a sample that is below t_c (which would normally be AF), and use the gate voltage to bring it into the FM state. Conversely, one can take a sample above t_c, and tune the bands down back into the AF state.

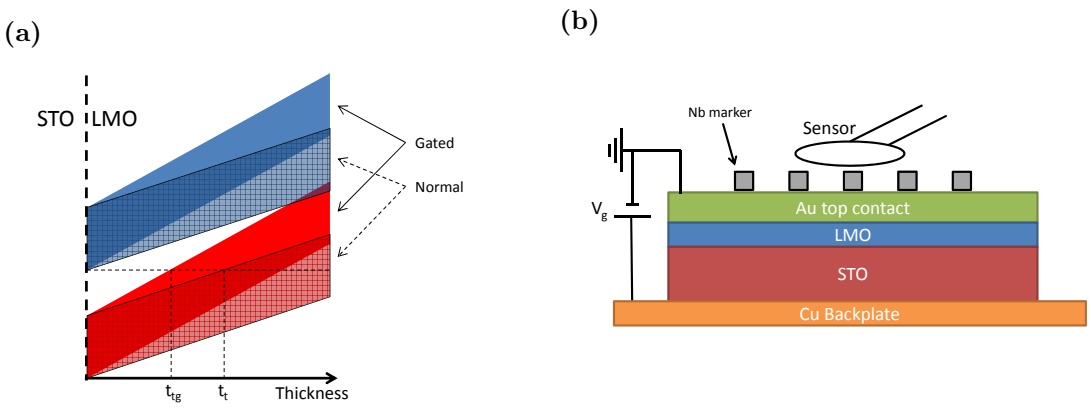

Figure 6.1: a) Influence of a gating voltage on the band structure of LMO, illustrating how electric field gating can cause electron transfer at lower thicknesses. b) Setup for sample backgating with a gate voltage V_g.

During these experiments, new control software was created for the SSM to replace the outdated software. For consistency, all data shown and discussed here is made with the new software. More details about the software can be found in Appendix A.

6.1 Experimental details

To do this, the SSM was equipped with extra wiring and a special sample holder to contain the electronics necessary. This will allow backgating with a gate voltage V_g up to $\pm$ 180 V. The samples were glued onto a copper plate using silver paint, which would function as a back gate. Since LMO is an insulator, the top surface of the LMO was covered with a 2 nm Ti layer followed by 20 nm of Au using sputtering. This would serve as the top gating contact. Finally, Nb markers were added to help during approach and movement. Since superconducting Nb will contain vortices, there will always be a signal present from the markers, regardless of the magnetic state of the LMO film. A schematic overview of the sample can be seen in Figure 6.1b.

Since Au is diamagnetic, we do not expect it will influence the magnetic intensity originating from the LMO underneath much. Furthermore, since this experiment is

aimed at seeing if magnetism can be switched on and off with a gate voltage, the actual value of the magnetic intensity is not relevant: We only need to see a transition between the AF and FM state (i.e., between no signal and any non-zero signal).

The first experiment involved a 6 uc sample prepared as described above. According to Ref. [10], the film should be ferromagnetic. However, when imaged with the SSM, no ferromagnetism was observed (Figure 6.2). One possible explanation is that the PLD parameters we used, which were initially used by the NUSNNI group, do not work with the setup in Twente. For example, a different heater design can cause the actual sample temperature (and temperature gradient) to be different between the two setups. This may lead to a difference in t_c between samples made by the NUSNNI group (Ref. [10]) and samples made ourselves.

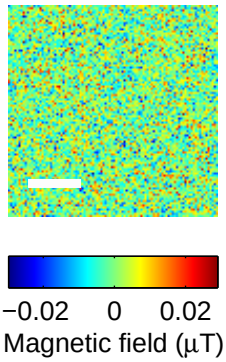

Figure 6.2: SSM image of an Au-capped 6 uc LMO sample.

The next step was an 8 uc sample with the same PLD parameters, which, again, should be ferromagnetic. A VSM measurement was performed first (before adding the Au layer) to verify the presence of the FM state. Figure 6.3a shows the magnetic moment M of the LMO/STO sample as a function of the applied magnetic field H, measured at 10 K. The background signal from the diamagnetic STO substrate has been substracted. In Figure 6.3b we can see M as a function of T. We clearly see the transition to a FM state around 100 K.

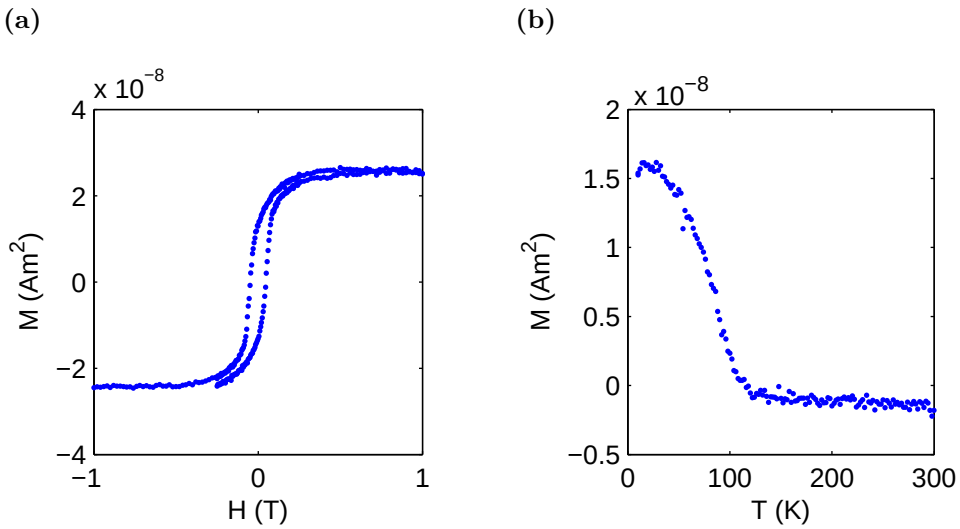

Figure 6.3: a) M versus H measurements of the 8 uc sample at 10 K . b) M versus T measurements of the 8 uc sample, cooled in $H = 1$ T.

From this, we can calculate that the magnetic moment is roughly 2.1 μ_B per Mn ion.

The magnetic signal was also seen by the SSM. However, when the Ti/Au top layer was added, the signal disappeared. This lead us to believe that the Au top layer is somehow influencing the magnetic state of the LMO film.

To confirm, a new 8 uc LMO sample was fabricated. This time, however, it was only partially covered with Au (see Figure 6.4a). This way, in case the Au indeed does suppress the LMO FM state, we should be able to see a clear difference between the part that is covered with Au and the part that is not.

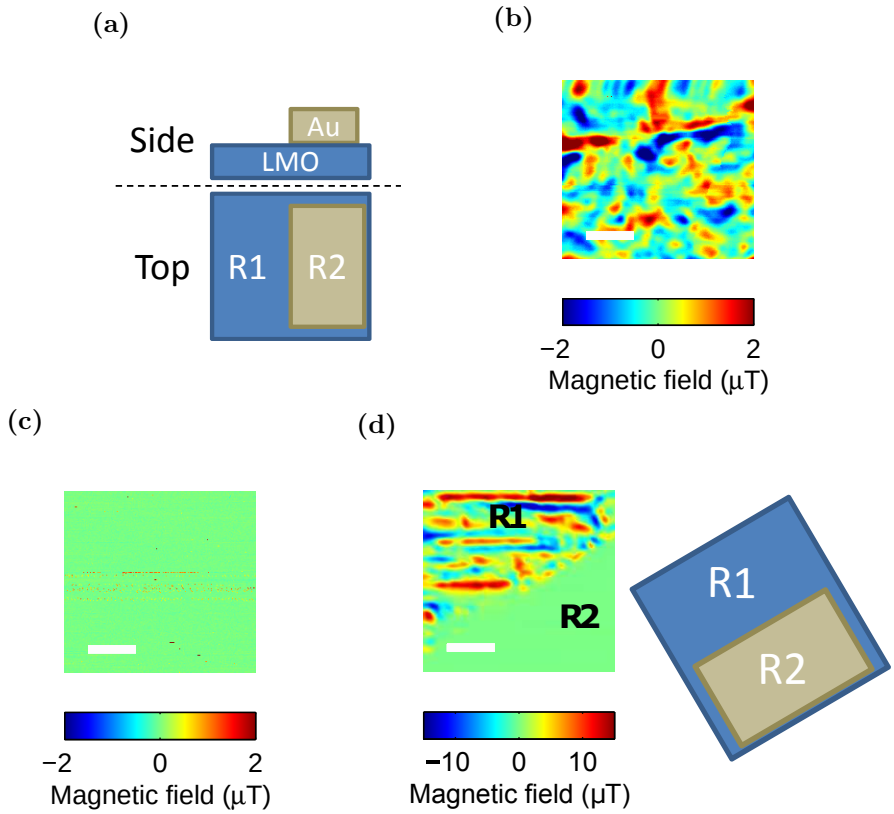

Figure 6.4: a) Schematic layout of the partially covered LMO sample, with regions R1 and R2 indicated. b) Scan of R1, showing the FM state is present. c) Scan of R2, showing no FM signal. d) Scan of the boundary between R1 and R2, with the sample orientation indicated. The scale bars indicate 50 μm.

Figures 6.4b-d show the results of SSM imaging of this sample. The area without the Au top layer (R1, Figure 6.4b) still shows an FM signal, whereas the region with Au on top (R2, Figure 6.4c) shows no magnetic signal. Finally, Figure 6.4d clearly shows the boundary between the two regions. The fact that the transition between the two regions is straight provides further evidence that Au is the cause of the suppression of the FM state.

The question then becomes: what is the mechanism that describes this interaction between Au and LMO? Since Au contains free electrons, one hypothesis is that the basis for this suppression is an RKKY-interaction between the Mn-ions, mediated by the free electrons in the Au layer. However, using Equation 3.1, taking $r = 3.905$ Å and k_m to be the Fermi wavevector k_F of Au ($= 1.2 * 10^{10}$ m^{-1} [93]), the coupling constant suggests FM coupling, which is not what we see.

Another explanation could be that the free electrons in the Au migrate into the LMO, combining with the doped Mn^{4+} ions to turn them back into Mn^{3+}. This way, the double exchange interaction between Mn^{3+} and Mn^{4+} ions is suppressed, which means the FM

order is suppressed as well. This is shown schematically in Figure 6.5.

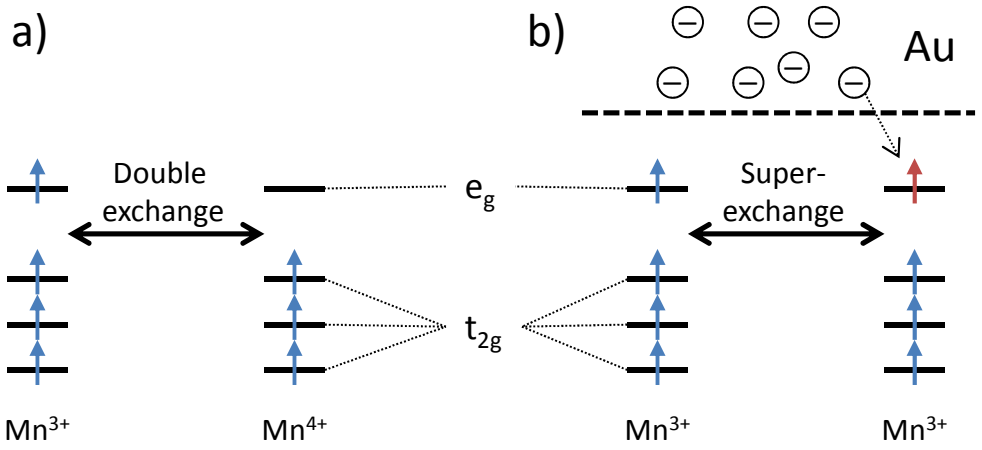

Figure 6.5: a) Double exchange between two mixed valency Mn ions in an LMO film. b) LMO film with a Au layer on top. A free electron from the Au moves into the LMO, leading to two Mn^{3+} ions and superexchange.

A third option is that during the deposition of the Au layer, the LMO film is being damaged. We have seen damage to thin films capped with sputtered Au in other experiments in this group. Those experiments have since moved to lower sputtering rates to reduce the damage done to the film. Creating a new sample this way should be a simple experiment to show if this is the case.

One more thing to note from Figure 6.4 is that the strength of the magnetic signal in R1 seems to decrease away from the boundary between R1 and R2 (i.e., it is higher in Figure 6.4d than in Figure 6.4b). There is a possibility that whatever interaction is causing the suppression of the FM state somehow causes an increase in FM strength at the boundary. However, a more likely and simpler explanation is that the sample was tilted somewhat inside the SSM, causing the sensor to be slightly further away from the sample when scanning R1, leading to a decreased signal.

6.2 Conclusions and Discussion

The original goal of this experiment was to apply gating voltages to LMO thin films to see if they could influence the magnetic state of the film. However, due to interactions between the Au top contact and the LMO film, the FM state disappeared.

Three possible scenarios were suggested to explain the suppression of the FM state. The simplest explanation is that the LMO film was damaged during the Au sputtering process, thereby removing the ferromagnetism. One way to confirm this would be to prepare another sample, but reducing the Au sputtering rate to limit the damage done to the film.

If the film was not damaged and the suppression of the FM state is indeed due to a physical interaction, one option is an RKKY-interaction, mediated by the free electrons in the Au top layer. However, calculating the sign of the coupling constant suggests that such an interaction would lead to a FM coupling between two Mn-ions, not an AF one.

The second hypothesis is that free electrons migrate from the Au into the LMO, lifting the mixed valence state and suppressing FM. The problem lies in determining if this is the case. Simply put, the objective is to measure the valence state of the Mn-ions in the LMO film. Normally, one would be able to do this using photoelectron

spectroscopy methods (such as XPS or UPS). However, due to the Au top layer, these methods are not capable of penetrating deep enough to probe the LMO.

X-ray absorption methods might work, though they require synchroton radiation to perform.TEM combined with EELS could also be an option. However, TEM sample preparation is destructive and therefore not preferable. In any case, creating a sample with lower sputtering rates should be done first to rule out (or confirm) damage to the film as a cause for the loss of FM.

7. Experiments on determining palaeointensity

This chapter contains preliminary results of a collaboration set up with the Paleomagnetic Laboratory Fort Hoofddijk of the Utrecht University. The aim is to determine the strength and orientation of earth's magnetic field by making SSM scans of geological samples, combined with X-ray microtomography (micro-CT). Knowing the history of earth's magnetic field will allow for the creation of better models to predict future behavior of the field. Besides that, a detailed map of earth's field history allows for more accurate magnetostratigraphy, the technique of dating archaeological sites and fossils based on their magnetization.

7.1 Premise

During volcanic eruptions, the molten rock that forms lava can reach temperatures of over 1000° C [117], far above the Curie temperature of $Fe_{3-x}Ti_xO_4$ (Titanomagnetite), a magnetic mineral common in lava [118]. Being above the Curie temperature, the magnetic domains inside the titanomagnetite will tend to align themselves with earth's magnetic field. As the lava cools, this magnetism is frozen in, leaving the mineral with a remanent magnetization known as Thermoremanent Magnetization (TRM). Therefore, measuring the TRM of a sample can yield information of earth's magnetic field strength (palaeointensity) and orientation (palaeodirection) at the time the sample was formed. Although palaeodirectional data is relatively easy to obtain, palaeointensity is notoriously difficult to assess [11].

Classically, the methods for obtaining information about the TRM involves repeatedly heating and cooling the sample and applying external magnetic fields at certain stages [12]. However, apart from being a destructive method of analysis (the original TRM is partially or completely removed during such measurements), it is limited to small, single-domain grains. This, of course, is not nearly true for most real geological samples. Furthermore, the success rate of such methods is low, and even technically successful measurements are not guaranteed to give accurate data [11].

Finding a new method of measuring the TRM in geological samples is, therefore, highly desirable. The ultimate goal of this collaboration is to see if SSM, in combination with other techniques, can provide a way to do this.

7.2 Experiments

Normally, the samples are obtained from lava-deposited rock formations from multiple locations around earth. The timescale of these samples is about 5,000 years (5 ky). Samples from fairly recent lava flows are easily dated, since recent volcanic eruptions are usually well recorded. For older samples, methods such as radiocarbon dating can be used. For these experiments, custom-made samples were used to have more control over the composition of the samples.

As mentioned in Chapter 4, the ferromagnetic particles in these sample will produce a dipole field. The field equations are based on 6 parameters: x_c, y_c and z_c that describe the

location of the particle, and the three components m_x, m_y and m_z of the magnetisation **m**. The three spatial coordinates can be determined with the micro-CT data (see Figure 7.1). With those, the field equations can easily be fitted to the SSM data to obtain **m**, which is then used to get information about the direction of Earth's magnetic field at the time the sample was formed. This model is being developed by the scientists in Utrecht in collaboration with colleagues from the Norgwegian Geological Survey in Trondheim.

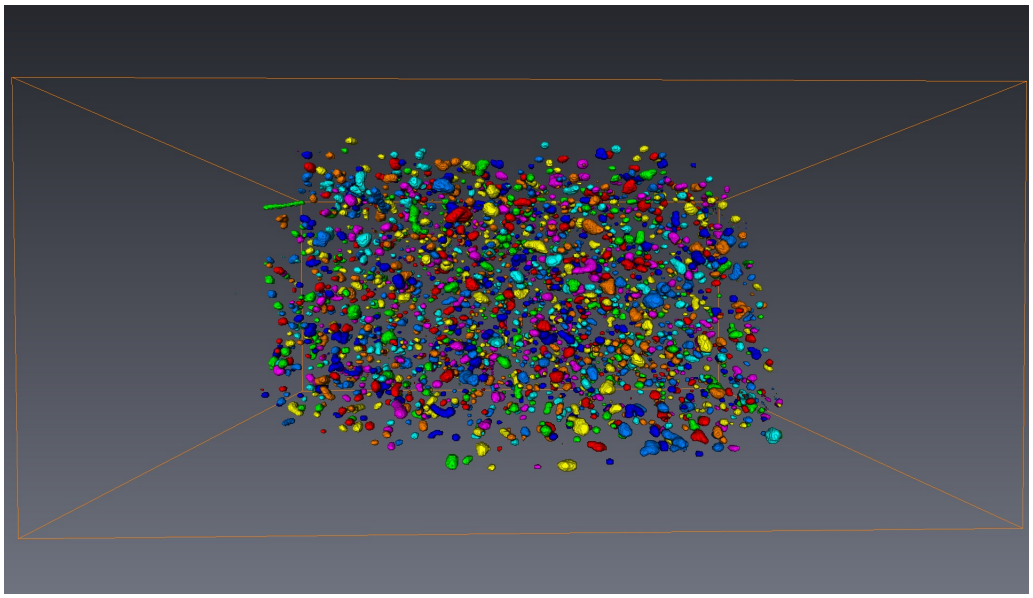

Figure 7.1: Micro-CT scan of magnetite grains embedded in Araldite epoxy. Image courtesy of the Paleomagnetic Laboratory of the Utrecht University.

In the simulations of Chapter 4, we have also seen that not necessarily every single dipole might be visible, its location lost in the total field (Figure 4.12). For modelling, however, it is vital that the right number of dipoles is used to get proper results for the magnetisation of each particle. It is therefore essential that each particle is properly resolved in the micro-CT scans. The micro-CT scans can resolve grains down to roughly 1 μm in size, which has implications for sample fabrication.

The first set of experiments was aimed at determining the magnetic field strength that emanates from such samples, and if the SQUID is able to handle such fields. Earth's magnetic field, which formed the domains in these samples, is roughly 30-60 μT [119]. However, much like an iron core in an electromagnet, the actual magnetic field originating from these domains can potentially be much larger. The samples were made from magnetite grains (1 vol%) embedded in Araldite epoxy, with a diameter of 2 mm and a thickness of 0.5 mm.

These experiments revealed that, under our regular scanning parameters, areas of the surface produced a magnetic field that was outside the measurable range. Because of this, we had to lower the signal strength by decreasing the feedback resistance. Whereas the scans of the LMO on STO samples were done with a feedback resistance of 100 kΩ, it was necessary to lower it to 1 kΩ, leading to approximately a factor 100 reduction in signal strength. Figure 7.2 shows 2 of the initial scans we performed. From the colour bars, one can clearly see the magnetic field strength has a range of up to $\pm$ 10 mT.

From the scans we can clearly see the magnetic field of the grains presenting itself as dipoles. Figure 7.2 shows a region with one particularly strong dipole (near the top of the image), and a collection of smaller ones nearby. The large dipole shows blurring off to the left side, due to the sensor being under an angle.

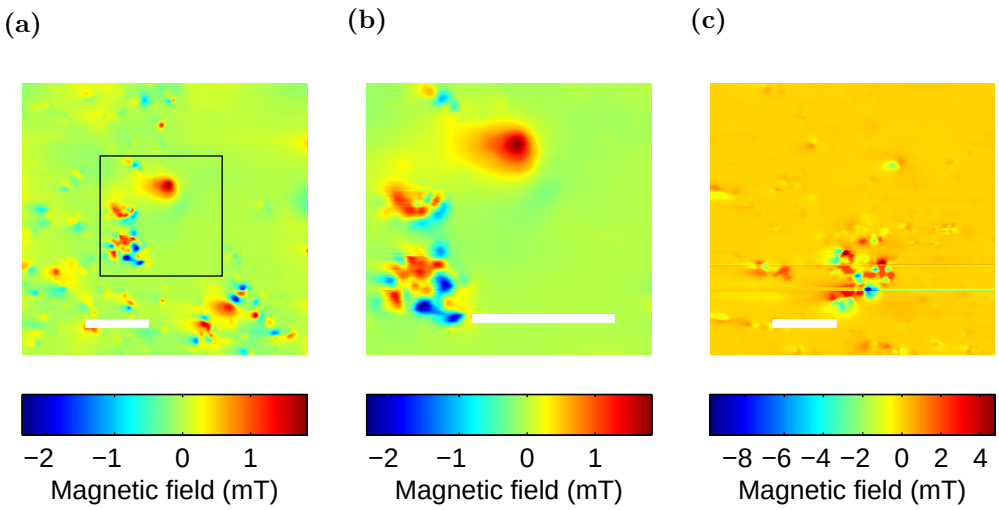

Figure 7.2: a) SSM scan of a geological testing sample. The boxed area is shown in (b). c) Scan of a different area on the same sample. Scale bars indicate 100 μm.

7.3 Outlook

There are still some hurdles to overcome while developing this technique. The scientists from Utrecht will focus their attention on sample preparation, modelling and data fitting, while we work on optimising the SSM. As mentioned, one of the changes we had to make was to change the feedback resistance to allow for the SSM to pick up the large magnetic field emanating from the samples.

The newer samples will be made of magnetite grains with a size of roughly 5-8 μm, mixed with calcite (a polymorph of $CaCO_3$) embedded in Araldite. The grains are mixed with calcite to prevent the grains from agglomerating into larger groups due to their net magnetisation. Calcite is also easily distinguishable from magnetite in the micro-CT scans due to the large difference in density. The magnetite/calcite mixture constitues roughly 5 vol%, the magnetite alone makes up about 0.05 vol%.

Apart from the signal strength, noise is of course also an issue. From simulations done by the Utrecht group, we have seen that at our current noise levels (see Chapter 2), the noise is just low enough to be able to get a proper solution (within a few percent) when fitting the model to the data. One method we will use is to make multiple scans of each area and calculate the average. Another option to reduce the noise some more is adding another low-pass filter with a lower cutoff frequency than the one currently used (5 kHz). The disadvantage of this is that it may impact scanning speed, depending on the exact filter and scanning parameters used. Adding the Nb shield mentioned in Chapter 2 should also give a solid reduction in noise.

Beyond that, the SSM measurements of these samples will have to be combined with the spatial information from the micro-CT scans. This means that we will need to be able to locate and identify certain areas of the surface and match them with the micro-CT data. The best approach for this is probably to deposit an array of Nb markers in such a way that they can be found during scanning and can be uniquely identified (i.e., a scan containing such a marker will give all necessary information about the scans location and orientation). The disadvantage of depositing these markers is that they will cover certain parts of the surface, meaning some information is lost. Furthermore, they may influence the magnetic field close to them due to the Meissner effect.

8. Conclusions and Discussion

8.1 Summary

Over the course of this thesis we have looked at scanning SQUID microscopy in both an experimental and a more analytical manner. The basic SQUID and SSM concepts were laid out in Chapter 2, explaining the basic functionality of the system. In Chapter 3 we discussed the perovskite $LaMnO_3$, the material that was the focus of most of the experimental work done over the course of this project. We looked at the different factors that influence the magnetic properties of LMO.

In Chapter 4 we discussed the spatial resolution of SSM, focusing on two contributions: the scanning height and the diameter of the SQUID pickup loop. Through the use of simulations, we have looked at how each of these influence SSM images both quantitatively as well as qualitatively. We have looked at a few common magnetic features that will be present in most SSM measurements: vortices, dipoles and ferromagnetic domains.

Using the simulated vortices, we were able to discern two regions in the spatial resolution: one where the scanning height is the dominant factor, and one where the pickup loop size is the dominant factor. At high z values, the d_v versus z curves converge on a curve described by $d_v \approx 1.53z$. At low z, d_v saturates to a value equal to d_0 ($= 2r_0$).

Next, we looked at dipoles and what they look like under the SSM. Unlike vortices, who have a field in the out-of-plane direction, dipoles (and particles that behave that create a dipole-like field) can have any 3-dimensional orientation. However, their distinctive shape makes them easily recognisable. We also had a look at clusters of dipoles, which one may encounter when imaging materials containing ferromagnetic particles. We noted that, even with a few dipoles close together, it becomes hard to distinguish each individual dipole. Being able to do so, however, is crucial for analysing scans and fitting data to models.

Finally, we used dipoles as a building block for larger ferromagnetic structures. We saw that some magnetisation directions will yield more information about the structure than others (particularly the out-of-plane direction). Using this technique, we simulated ferromagnetic domains, such as those present on the LMO films we used in our experiments.

Through the ferromagnetic domains, we learned that, as the scanning height increases, the domain structure becomes lost due to the fields averaging out. The same thing happens when we increase the radius of the pickup loop. Because of this, we must conclude that making claims about domain size, structure or orientation is impossible unless the spatial resolution of the SSM is high enough to resolve it on a level shown in Figures 4.15a and 4.16a. Otherwise, one cannot be sure that what is seen in a scan is truly the underlying domain structure, or an average over smaller, sub-resolution structures. We have also seen that the root-mean-square value of the field has a linear relation with the magnetisation. The coefficient between the two is dependent on the direction of the magnetisation.

Finally, we discussed the deconvolution problem and how it relates to SSM imaging. Due to the finite size of the pickup loop, the measured signal is an average over a certain area. Deconvolution techniques can be used to try and reverse this averaging process. Doing this typically requires knowledge of the point-spread function, a mathematical

description of how exactly the system convolutes the signal.

Using an actual scan of a vortex and Matlab's built in deconvolution methods, we have tried to determine the PSF for our own system. To do this, we have to use a theoretical description of a vortex, which raises the issue of not really knowing the scanning height. We typically estimate it to be roughly 2 μm, but having better knowledge of this number will improve any future deconvolution attempts.

We continued looking at deconvolution by applying it to simulated vortices and ferromagnetic domains. We used three different algorithms, and have seen that, in the case of vortices, blind and Lucy-Richardson deconvolution solve the problem nicely. The third algorithm, a regularized method, does well for low z values, but suffers from ringing artifacts more and more as z increases.

Furthermore, we have seen that deconvolution does not necessarily yield a solution representing the original, unconvoluted signal. This was most obvious when applying deconvolution to the ferromagnetic domain simulations. This shows that one must be wary when analysing deconvolved images, as how much they represent reality may vary wildly.

Finally, we looked at noise and its impact on the deconvolution problem. Noise is a problem because it can create large values in the frequency domain at points where the PSF is close to zero. Of course, battling noise is difficult because it is inherently random. We had a look at deconvoluting vortices that had added noise. The blind and Lucy-Richardson algorithms managed fairly well, with the caveat that the blind algorithm produced large spikes at the edges. Naturally, as the noise increases and the signal-to-noise ratio worsens, the end result becomes worse as well.

Chapter 5 describes the experiments performed on LMO thin films deposited at different oxygen pressures on STO substrates. We wanted to investigate how the properties of the films change as a function of deposition pressure, with a focus on magnetic properties. X-ray diffraction measurements show that all films are epitaxially strained, and that the out-of-plane lattice parameter shows a local minimum at $P_{O_2} = 10^{-4}$ Torr. At $P_{O_2} = 10^{-1}$ Torr, the lattice parameter shows a sudden decrease to a value of approximately 3.9 Å, matching the STO substrate both in-plane and out-of-plane.

This behaviour centering around a local extremum is also seen in vibrating sample magnetometer measurements. There, we saw that the magnetisation had a maximum in the field-cooling experiments at $P_{O_2} = 10^{-4}$ Torr. All samples showed a similar Curie temperature of roughly 100 K, apart from the $P_{O_2} = 10^{-1}$ Torr, which had a Curie temperature of about 175 K. This large difference is likely related to the change in lattice parameter observed in the XRD measurements.

The local maximum at $P_{O_2} = 10^{-4}$ Torr can be explained by noting that, from literature, we know that the La/Mn ratio changes as a function of deposition pressure, which causes the Mn^{4+}/Mn^{3+} ratio to change as well. The double exchange interactions becomes dominant over the superexchange interactions as the ratio reaches an optimal value at $P_{O_2} = 10^{-4}$, after which the Mn^{3+} become too sparse and the double exchange interactions decrease.

The M versus H curves measured with the VSM showed that some samples had multiple saturation levels. This is probably due to contamination with magnetic particles. Exchange bias was not observed, since there was no shift of the M versus H curves along the H axis. It could also indicate the presence of other phases, though contaminants are more likely.

The SSM measurements showed that the LMO films have a magnetic domain structure at the surface at all deposition pressures. Due to the reasons stated before, we cannot make any real claims about the domain size or structure due to the limited spatial resolution of our SSM sensors. From what we can see, the domain structure is similar

across the pressure range and across each individual sample as well.

As measured by the SSM, the magnetisation of the films (expressed as B_{RMS}) increases monotonically with increasing P_{O_2}, saturating to a certain value, then suddenly increasing again around $P_{O_2} = 10^{-1}$ Torr. This can be explained by the magnetic anisotropy increasing due to one axis becoming 'easier' (i.e., lower energy) than the others, causing spins to align themselves along that axis. Of course, lowering the energy has its limits, and will not increase spin alignment indefinitely (for example, when it reaches the lowest energy state or becomes balanced by other forces).

The increase in magnetisation with increasing pressure may also be related to a decrease in the bandgap found by another group. This, combined with the possibility of an electronic reconstruction scenario as laid out in Chapter 3, can also cause an increase in Mn^{4+} ions and, consequently, double exchange interactions.

The sudden jump for the $P_{O_2} = 10^{-1}$ Torr might again be related to the behaviour seen in the XRD and VSM measurements. It is possible that the LMO in this film has crystallised in a different phase or structure, altering its properties in a significant way.

Resistivity measurements show similar behaviour from most samples, showing sheet resistances in the MΩ range and increasing with decreasing temperature. The $P_{O_2} = 5 * 10^{-7}$ Torr sample showed very different behaviour: increasing resistivity with increasing temperature. This is something similar to conductivity in reduced STO films, which leads us to believe the STO substrate has been reduced during the sample production, leading to it dominating the resistivity measurements.

Among the other samples, the overall trend was increasing resistivity with decreasing pressure. The $P_{O_2} = 10^{-5}$ Torr showed somewhat lower resistance than the trend would suggest. A contribution from a possibly reduced STO substrate is not likely, since the resistance increases rapidly with decreasing pressure.

Chapter 6 focuses on experiments done with Au-capped LMO thin films on STO substrates. The goal was originally to perform gating experiments and transition from the FM to AF state by applying a gate voltage. However, during the experiments we noticed that depositing the Au capping layer suppressed the FM state. This was confirmed by covering half of one sample with gold and imaging the border region with SSM.

There are some possibilities as to why a capping layer suppresses the FM state. One likely candidate is that the Au sputtering process damages the film, removing the FM state. A second possibility is that the itinerant electrons of the Au mediate an RKKY-interaction between the Mn-ions, though a basic calculation seems to indicate this is not the case. A third option is that electrons from the Au layer move into the LMO layer and combine with Mn^{4+} electrons, decreasing the Mn^{4+}/Mn^{3+} and suppressing double exchange.

Lastly, Chapter 7 outlined a collaboration recently set up with the Paleomagnetic Laboratory of the Utrecht University. The objective is to see if a combination of SSM and X-ray microtomography can replace older methods of determining Earth's magnetic field throughout history. These older methods are complicated, not very reliable and, most of all, destructive measurements.

From a few testing measurements we have seen that the natural samples we are interested in produce large magnetic fields that push the limits of what our setup can handle. This was handled by lowering the feedback resistance of the SSM. We also learned, from models created by the scientists from Utrecht, that the noise levels of the SSM are close to the limit of the model being able to properly fit the data. This can possibly be dealt with by averaging the data over multiple measurements, using a Nb shield and adding additional low-pass filters into the circuitry to suppress high-frequency noise.

8.2 Discussion and recommendations

Starting off with the discussion in Chapter 4, we have seen that simulations are a nice way to try and predict how samples interact with the SSM and what the final image may look like. Currently, the models that were used were fairly simple, and a number of improvements can be made.

One such improvement is trying to include the angle between the sensor and the sample into the equations, and consequently the relevant in-plane components of the magnetic field. Currently, only the out-of-plane component is considered when doing these simulations. However, to more closely predict the behaviour of our own setup, including the angle is a must.

The models can also be improved by using more sophisticated models than the ones here. This mostly concerns the ferromagnetic domains, which at this point contain no information about the domain walls, anisotropy, etc. We currently simply assumed that the domain walls had no thickness (i.e., spins flipped from one site to the next) and that all spins were aligned along one of the three carthesian directions. One can imagine, for example, domains aligning themselves along step edges, creating domains that are elongated along a specific direction. The problem here, of course, is that showing what these various interactions do means working on a smaller scale than was done here. Then the question arises how relevant those results are for our current SSM with its spatial resolution.

Deconvolution is probably the section that has the most work laid out for it. In this thesis we only showed the basic principles of deconvolution to try and show how it applies to SSM. We have seen that deconvolution can be a powerful tool, but one that must be handled carefully. Delving more into the mathematics of deconvolution and try and optimise it for SSM is probably worthwhile. Not much work involving deconvolution for SSM has been done so far, but the potential gains in spatial resolution are something to consider. The downside of deconvolution is that it does change the field values, making those unreliable. Therefore, deconvolution is more relevant to situations where spatial resolution is more important than field resolution.

Of course, the noise issue in deconvolution also deserves attention, since any real experiment will involve noise. We have seen that some of Matlab's basic deconvolution algorithms can deal with added noise decently up to a certain point where the signal-to-noise ratio becomes too small. There are more sophisticated ways to deal with noise, but they again require a solid understanding of the mathematics of signal analysis. Creating proper deconvolution methods for the SSM will have to incorporate some way to deal with the noise for it to be useful.

Moving over to the actual experiments, one of the issues with the samples from the pressure series is that they were not made at the University of Twente, which means we had no control over the production and little information about anything that might have happened during production. These samples were made in Singapore for consistency with earlier experiments. For example, the resistivity showed that one sample had a significant contribution from what is likely a reduced STO substrate. Also the $P_{O_2} = 10^{-6}$ Torr sample showed dipoles on the SSM image, possibly originating from micrometre-sized particles that do not resemble dust or dirt and might have been introduced during fabrication. In future, it would be better to produce the samples here to allow better control over the production process.

One missing piece of information throughout the story was the exact elemental composition of the films. Knowing the La/Mn and Mn^{4+}/Mn^{3+} ratios would definitely improve our understanding of what exactly happens as the deposition pressure is changed. This can be done, for example, with X-ray photoelectron spectroscopy or Rutherford

backscattering spectroscopy.

The general problem with interpreting the results is that the three factors impacting magnetism we discussed (strain, composition and electronic reconstruction) each influence each other as well. Therefore, one cannot pinpoint one exact cause to the effects we have seen here: it is all an interplay between these three factors.

A possible follow-up experiment would be to reduce the film thickness to 5 or 6 uc (i.e., around the critical thickness) and see if changing the deposition pressure can switch the film from FM to AF or vice versa. This can more clearly show the interplay between composition and the possible electronic reconstruction scenario.

In Chapter 6 we saw that the Au-capping layer suppressed the FM state. Attempting Au deposition with a lower sputtering rate can determine if this is due to damage to the film because of the sputtering process. If not, other methods will need to be used to find out what exactly is happening at the interface between the Au and the LMO.

In the case of film damage, and if it can be solved with lower Au sputtering rates, one can go back and attempt the gating experiments again. This experiment can provide evidence about the possibility of the electronic reconstruction scenario. It will also open up avenues to look into magnetic-switching devices created from LMO thin films.

Apart from Au capping layers, other capping layers may be interesting as well. At the time of publication, there are some preliminary experiments underway with an LAO capping layer. LAO, just like LMO, is a polar material. Such an experiment can give information about the electronic reconstruction scenario and if the potential build-up continues across different polar materials, and if it can result in ferromagnetic ordering or possibly a 2-dimensional electron gas (as is the case with LAO/STO). Other capping layers may be of interest as well. For example, an STO capping layer causes a 2DEG to form in LAO/STO at a lower thickness (2 uc [120]). It would be interesting to see if using an STO capping layer on LMO can cause the AF to FM transition to occur at a lower thickness.

Throughout this thesis we have also seen that it can be good practice to have some Nb markers on a sample when designing an SSM experiment. From Chapter 4, we know that we can use the vortices that appear in Nb to get some information about our spatial resolution, and they can be used to determine the PSF for deconvolution purposes. They also provide an effective way to determine the effective area of the pickup loop, since a vortex will always produce 1 Φ_0 of flux. In Chapter 6, we used the markers as a reference to be able to approach the sample in case the sample itself was not ferromagnetic. Finally, for our collaboration with Utrecht University, we will use Nb markers to determine our position and orientation on the sample, to combine the data with that of other experiments.

The idea, then, is to create an array of Nb that would preferably do the following: 1) Each marker should be large enough to be seen by the SSM and contain 1 or more vortices for the SSM to image. 2) The markers should be spaced out enough that they do not obscure the underlying magnetic structure too much, but close enough together that one can be found in a typical SSM scan (400 by 400 μm^2). 3) If possible, each marker should be unique in shape and orientation, so that scanning one marker will immediately yield all the positional and directional information required.

As a long term recommendation, it might be worthwhile to look into upgrading the existing SSM setup or potentially building a new SSM with better spatial resolution. The University of Twente houses advanced deposition techniques that allows for the creation of structures on nanometre scales (focused ion beam milling and electron-beam lithography). Utilising these techniques for the creation of smaller SQUIDs and pickup loops has been delved into a little already in this group (see Ref. [32]), but pursuing nano-scanning SQUID is worthwhile for a number of reasons.

Of course, the improved spatial resolution is relevant as structures and devices become ever smaller, which means measurement instruments must have ever better spatial resolution. Not only that, due to the smaller pickup loop, the system will be less sensitive to external magnetic field noise. The lower field sensitivity is compensated by the fact that, with an improved setup, one can possibly lower the sensor-sample distance from the scale of micrometres into the sub-micrometre range. Due to the $1/r^n$ nature of dipoles and vortices, the magnetic field to be measured will increase drastically.

From more of a business standpoint, putting effort into improving the SSM will keep our group (and by extension, the university) relevant in the field of SSM. With several groups already having created nano-scanning SQUID setups [121,122], one must be careful not to fall behind. Of course, the current SSM setup will still be useful for certain experiments, but as mentioned, objects of interest become ever smaller.

The issue with our current setup is that the wiring connecting the sensor to the outside is on top of the chip containing the SQUID and pickup loop, meaning it limits the distance between sensor and sample. Some recent developments in nano-scanning SQUID have seen a SQUID on a tip, similar to an AFM tip [122]. This change in geometry allows for approaching the sample closer than our current setup can. This also means that the motors currently controlling the movement of the SSM will be unsuitable, and piezoelectric actuators will have to be used instead. For that reason, it might be more practical to create a second setup for nano-scanning SQUID.

A few words of thanks

Although my name is on the cover page, no scientific work is done alone. Whether as a colleague, friend or family member, a lot of people have contributed to this work in their own way, and it is here that I extend my gratitude to you.

First of all, I would like to thank Hans for giving me this assignment and work on something that can only be found in a few places on Earth. Your additional work as dean of our faculty has made it difficult at times to do your work as head of the group in a satisfying manner, but it is all no less appreciated.

Secondly, my thanks go out to Renshaw. You taught me most of what I know about the SSM, and your collaboration and support in the LMO project has been extremely valuable. The guitar still sounds great, hopefully I will have some more time to play it after this! By extension, I want to thank your colleagues of the NUSNNI group of the University of Singapore for preparing the samples.

Next, I want to thank Ankur for being my brother in arms on the battlefield of thin-film-science. Your help doing all the measurements presented here is very much appreciated. The days (weeks, months) of frustration we had over getting our sensors to work were made a little lighter having each other as support.

My thanks also go out to Lennart and Annemarieke. Working with you and applying SSM for palaeomagnetism was a nice and refreshing change from the field of complex oxides. I hope the collaboration between you and ICE will continue and together you will be able to develop this technique to the fullest.

Performing experiments requires good, solid equipment, and two skilled technicians to keep everything running like clockwork. Frank and Dick, not only do you keep all our labs in tip-top shape, you also make sure the social atmosphere is top of the line. And of course extended grattitude to Dick for his help with the SSM setup.

Of course, I thank all my colleagues and fellow students, especially my roommates in Carré 2134 (which, as we all know, is far more enjoyable than the rooms on the bottom floor). Your contributions, discussions and matches of football shall be sorely missed.

Now, not everyone has contributed in the same way. Moral support and friendship are no less important than scientific discussions and collaborations. Although I cannot name you all, you know who you are (and if you don't, then I wonder why you are reading this in the first place) and I thank you. The one I will name is Julia, for confirming the fact that having a Player 2 makes life a lot better.

Finally, but probably most of all, I want to thank my parents. For 24 years I could always count on your everlasting support. Especially the last 12 or so months, both professionally as well as privately, you were there when I needed you, no questions asked.

So thanks to you all, I hope I helped each of you at least as much as you helped me.

$\sim\sim$ Pim

Facts and fiction

42.494 words, 96 figures, 8 chapters, too many sensors. Over 9 GB of harddrive space. Discontinuity, quantitatively and qualitatively are annoying words. The cover image is edge detection performed on one of the domain simulations. I was not kidnapped to Germany. Raisins are good. Psychology is a science. Fact or Fiction is a decent card. Dipoles.

Bibliography

[1] S. Range, *Gravity probe B*, NASA, **2004**.

[2] J. Clarke and A. I. Braginski, *The SQUID handbook*, Wiley-VCH, **2004**.

[3] R. Kleiner, D. Koelle et al., *Superconducting quantum interference devices: State of the art and applications*, Proceedings of the IEEE, Vol. **92**, p. 1534-1548, **2004**.

[4] R. Bradley, J. Clarke et al., *Microwave cavity searches for dark-matter axions*, Reviews of Modern Physics, Vol. **75**, p. 777-817, **2003**.

[5] S. J. Asztalos, G. Carosi et al., *SQUID-based microwave cavity search for dark-matter axions*, Physical Review Letters, Vol. **104**, p. 041301, **2010**.

[6] C. M. Wilson, G. Johansson et al., *Observation of the dynamical Casimir effect in a superconducting circuit*, Nature, Vol. **479**, p. 376-379, **2011**.

[7] B. Cabrera, *First results from a superconductive detector for moving magnetic monopoles*, Physical Review Letters, Vol. **48**, p. 1378-1381, **1982**.

[8] R. McCusker, *The quest for quarks*, Cambridge University Press, **1983**.

[9] R. K. Hobbie and B. J. Roth, *Intermediate physics for medicine and biology*, Springer Science+Business Media, **2007**.

[10] X. R. Wang, C. J. Li et al., *Imaging and control of ferromagnetism in a polar antiferromagnet*, arXiv, p. arXiv:1409.0520, **2014**.

[11] L. de Groot, K. Fabian et al., *Magnetic force microscopy reveals meta-stable magnetic domain states that prevent reliable absolute palaeointensity experiments*, Nature Communications, Vol. **5**, p. 4548, **2014**.

[12] D. Dunlop, *Physical basis of the Thellier-Thellier and related paleointensity methods*, Physics of the Earth and Planetary Interiors, Vol. **187**, p. 118-138, **2011**.

[13] R. C. Jaklevic, J. Lambe et al., *Quantum interference effects in Josephson tunneling*, Physical Review Letters, Vol. **12**, p. 159-160, **1964**.

[14] I. Giaever, *Energy gap in superconductors measured by electron tunneling*, Physical Review Letters, Vol. **5**, p. 147-148, **1960**.

[15] J. Nicol, S. Shapiro and S. P. H., *Direct measruement of the superconducting energy gap*, Physical Review Letters, Vol. **5**, p. 461-464, **1960**.

[16] J. Q. You and F. Nori, *Atomic physics and quantum optics using superconducting circuits*, Nature, Vol. **474**, p. 589-597, **2011**.

[17] P. W. Anderson and J. M. Rowell, *Probable observation of the Josephson superconducting tunneling effect*, Physical Review Letters, Vol. **10**, p. 230-232, **1963**.

[18] F. London, *Superfluids*, John Wiley & Sons, **1948**.

[19] R. Doll and M. Näbauer, *Experimental proof of magnetic flux quantization in a superconducting ring*, Physical Review Letters, Vol. **7**, p. 51-52, **1961**.

[20] B. S. Deaver and W. M. Fairbank, *Experimental evidence for quantized flux in superconducting cylinders*, Physical Review Letters, Vol. **7**, p. 43-46, **1961**.

[21] V. V. Schmidt, *The physics of superconductors*, Springer, **1997**.

[22] W. C. Stewart, *Current-voltage characteristics of Josephson junctions*, Appied Physics Letters, Vol. **12**, p. 277-280, **1968**.

[23] D. E. McCumber, *Effect of ac impedance on dc voltage-current characteristics of superconductor weak-link junctions*, Journal of Applied Physics, Vol. **39**, p. 3113-3118, **1968**.

[24] P. K. Hansma, G. I. Rochlin and J. N. Sweet, *Externally shunted Josephson junctions: Generalized weak links*, Physical Review B, Vol. **4**, p. 3003-3014, **1971**.

[25] A. Barone and G. Paternò, *Physics and applications of the Josephson effect*, John Wiley & Sons, **1982**.

[26] C. J. M. Verwijs, *Fractional flux quanta in high-T_c/low-T_c superconducting structures*, Ph.D. Thesis, University of Twente, **2009**.

[27] C. Ludwig, C. Kessler et al., *Versatile high performance digital SQUID electronics*, IEEE Transactions on Applied Superconductivity, Vol. **11**, p. 1122-1125, **2001**.

[28] J. H. Claassen, *Coupling considerations for SQUID devices*, Journal of Applied Physics, Vol. **46**, p. 2268-2275, **1975**.

[29] J. R. Kirtley and J. P. Wikswo, *Scanning SQUID microscopy*, Annual Reviews, Vol. **29**, p. 117-148, **1999**.

[30] X. Jiang, W. B. Cook and W. S. Hackenberger, *Cryogenic piezoelectric actuators*, Proceedings of SPIE, Vol. **7439**, p. 74390Z, **2009**.

[31] H. Nyquist, *Thermal agitation of electric charge in conductors*, Physical Review, Vol. **32**, p. 110-113, **1928**.

[32] A. G. P. Troeman, *NanoSQUID magnetometers and high resolution scanning SQUID microscopy*, Ph.D. Thesis, University of Twente, **2007**.

[33] R. H. Koch, D. P. DiVincenzo and J. Clarke, *Model for 1/f flux noise in SQUIDs and qubits*, Physical Review Letters, Vol. **98**, p. 267003, **2007**.

[34] R. C. Bialczak, R. McDermott et al., *1/f flux noise in Josephson phase qubits*, Physical Review Letters, Vol. **99**, p. 187006, **2007**.

[35] P. Dutta, P. Dimon and P. M. Horn, *Energy scales for noise processes in metals*, Physical Review Letters, Vol. **43**, p. 646-649, **1979**.

[36] P. Dutta and P. M. Horn, *Low-frequency fluctuations in solids: 1/f noise*, Reviews of Modern Physics, Vol. **53**, p. 497-516, **1981**.

[37] M. J. Ferrari, M. Johnson et al., *Magnetic flux noise in copper oxide superconductors*, Journal of Low Temperature Physics, Vol. **94**, p. 13-61, **1993**.

[38] L. Faoro and L. B. Ioffe, *Microscopic origin of low-frequency flux noise in Josephson circuits*, Physical Review Letters, Vol. **100**, p. 227005, **2008**.

[39] S. K. Choi, D. H. Lee et al., *Localization of metal-induced gap states at the metal-insulator interface: Origin of flux noise in SQUIDs and superconducting qubits*, Physical Review Letters, Vol. **103**, p. 197001, **2009**.

[40] M. Johnsson and P. Lemmens, *Perovskites and thin films - crystallography and chemistry*, Journal of Physics: Condensed Matter, Vol. **20**, p. 264001, **2008**.

[41] J. G. Bednorz and K. A. Müller, *Possible high T_c superconductivity in the Ba-La-Cu-O system*, Zeitschrift für Physik B: Condensed Matter, Vol. **64**, p. 189-193, **1986**.

[42] A. P. Ramirez, *Colossal magnetoresistance*, Journal of Physics: Condensed Matter, Vol. **9**, p. 8171-8199, **1997**.

[43] M. Opel, *Spintronic oxides grown by laser-MBE*, Journal of Physics D: Applied Physics, Vol. **45**, p. 033001, **2012**.

[44] H. Yamada, M. Kawasaki et al., *$LaMnO_3/SrMnO_3$ interfaces with coupled charge-spin-orbital modulation*, Applied Physics Letters, Vol. **89**, p. 052506, **2006**.

[45] J. B. A. A. Elemans, B. van Laar et al., *The crystallopgraphic and magnetic structures of $La_{1-x}Ba_xMn_{1-x}Me_xO_3$ (Me = Mn or Ti)*, Journal of Solid State Chemistry, Vol. **3**, p. 238-242, **1971**.

[46] J. Rodríguez-Carvajal, M. Hennion et al., *Neutron-diffraction study of the Jahn-Teller transition in stoichiometric $LaMnO_3$*, Physical Review B, Vol. **57**, p. R3191, **1998**.

[47] C. Franchini, R. Kováčik et al., *Maximally localized Wannier functions in $LaMnO_3$ within PBE+U, hybrid functionals, and partially self-consistent GW: an efficient route to construct ab-initio tight-binding parameters for e_g perovskites*, Journal of Physics: Condensed Matter, Vol. **24**, p. 235602, **2012**.

[48] J. H. Lee, K. T. Delaney et al., *Strong coupling of Jahn-Teller distortion to oxygen-octahedron rotation and functional properties in epitaxially strained orthorhombic $LaMnO_3$*, Physical Review B, Vol. **88**, p. 174426, **2013**.

[49] C. Aruta, M. Angeloni et al., *Preparation and characterization of $LaMnO_3$ thin films grown by pulsed laser deposition*, Journal of Applied Physics, Vol. **100**, p. 023910, **2006**.

[50] J. A. Alonso, M. J. Martínez-Lope and M. T. Casais, *Evolution of the Jahn-Teller distortion of MnO_6 octahedra in $RMnO_3$ perovskites (R = Pr, Nb, Dy, Tb, Ho, Er, Y): a diffraction study*, Inorganic Chemistry, Vol. **39**, p. 917-923, **2000**.

[51] K. H. Ahn and A. J. Millis, *Effects of uniaxial strain in $LaMnO_3$*, Physical Review B, Vol. **64**, p. 115103, **2001**.

[52] B. R. K. Nanda and S. Satpathy, *Magnetic and orbital order in $LaMnO_3$ under uniaxial strain: A model study*, Physical Review B, Vol. **81**, p. 174423, **2010**.

[53] J. Bland, *A Mössbauer spectroscopy and magnetometry study of magnetic multilayers and oxides*, Ph.D. Thesis, University of Liverpool, **2002**.

[54] J. B. Goodenough, *Theory of the role of covalence in the perovskite-type manganites [La,M(II)]MnO_3*, Physical Review, Vol. **100**, p. 564-573, **1955**.

[55] J. B. Goodenough, *An interpretation of the magnetic properties of the perovskite-type mixed crystals* $La_{1-x}Sr_xCoO_{3-\lambda}$, Journal of Physics and Chemistry of Solids, Vol. **6**, p. 287-297, **1958**.

[56] J. Kanamori, *Superexchange interaction and symmetry properties of electron orbitals*, Journal of Physics and Chemistry of Solids, Vol. **10**, p. 87-98, **1959**.

[57] P. W. Anderson, *Antiferromagnetism. Theory of superexchange interaction*, Physical Review, Vol. **79**, p. 350-356, **1950**.

[58] E. O. Wollan and W. C. Koehler, *Neutron diffraction study of the magnetic properties of the series of perovskite-type compounds [(1-x)La, xCa]*MnO_3*]*, Physical Review, Vol. **100**, p. 545-563, **1955**.

[59] M. Capone, D. Feinberg and M. Grilli, *Stabilization of A-type layered antiferromagnetism phase in* $LaMnO_3$ *by cooperative Jahn-Teller deformations*, European Physics Journal B, Vol. **17**, p. 103-109, **2000**.

[60] Y. Murakami, J. P. Hill et al., *Resonant X-ray scattering from orbital ordering in* $LaMnO_3$, Physical Review Letters, Vol. **81**, p. 582-585, **1998**.

[61] N. Doiron-Leyraud, C. Proust et al., *Quantum oscillations and the Fermi surface in an underdoped high-*T_c *superconductor*, Nature, Vol. **447**, p. 565-568, **2007**.

[62] J. Q. Li and P. Xiao, *Fabrication and characterisation of* $La_{0.8}Sr_{0.2}MnO_3$*/metal interfaces for application in SOFCs*, Journal of the European Ceramic Society, Vol. **21**, p. 659-668, **2001**.

[63] M. Cesaria, A. P. Caricato et al., *LSMO - growing opportunities by PLD and applications in spintronics*, Journal of Physics: Conference Series, Vol. **292**, p. 012003, **2011**.

[64] J. Hemberger, A. Krimmel et al., *Structural, magnetic and electrical properties of single-crystalline* $La_{1-x}Sr_xMnO_3$ $(0.4 < x < 0.85)$, Physical Review B, Vol. **66**, p. 094410, **2002**.

[65] J. A. M. Roosmalen, E. H. P. Cordfunke et al., *The defect chemistry of* $LaMnO_{3\pm\delta}$, Journal of Solid State Chemistry, Vol. **110**, p. 100-105, **1994**.

[66] R. de Renzi, G. Allodi et al., *Phase diagram of low doping manganites*, Physica B, Vol. **289-290**, p. 85-88, **2000**.

[67] K. Kamata, T. Nakajima and T. Hayashi, *Nonstoichiometric behavior and phase stability of rare earth manganites at 1200°: (1).* $LaMnO_3$, Materials Research Bulletin, Vol. **13**, p. 49-54, **1978**.

[68] F. Abbattista and M. Lucco Borlera, *Reduction of* $LaMnO_3$*. Structural features of phases* $La_8Mn_8O_{23}$ *and* $La_4Mn_4Mn_{11}$, Ceramics International, Vol. **7**, p. 137-141, **1981**.

[69] R. Cortés-Gil, A. Arroyo et al., *Evolution of magnetic behaviour in oxygen deficient* $LaMnO_{3-\delta}$, Journal of Physics and Chemistry of Solids, Vol. **67**, p. 579-582, **2006**.

[70] K. J. Choi, M. Biegalski et al., *Enhancement of ferroelectricity in strained* $BaTiO_3$ *thin films*, Science, Vol. **306**, p. 1005-1009, **2004**.

[71] Y. S. Hou, H. J. Xiang and X. G. Gong, *Intrinsic insulating ferromagnetism in manganese oxide thin films*, Physical Review B, Vol. **89**, p. 064415, **2014**.

[72] W. S. Choi, Z. Marton et al., *Effects of oxygen-reducing atmosphere annealing on $LaMnO_3$ epitaxial thin films*, Journal of Physics D: Applied Physics, Vol. **42**, p. 165401, **2009**.

[73] H. S. Kim and H. M. Christen, *Controlling the magnetic properties of $LaMnO_3$ thin films on $SrTiO_3(100)$ by deposition in a O_2/Ar gas mixture*, Journal of Physics: Condensed Matter, Vol. **22**, p. 146007, **2010**.

[74] Z. Marton, S. S. A. Seo et al., *Growth control of stoichiometry in $LaMnO_3$ epitaxial thin films by pulsed laser deposition*, Journal of Crystal Growth, Vol. **312**, p. 2923-2927, **2010**.

[75] Y. G. Zhao, M. Rajeswari et al., *Effect of oxygen content on the structural, transport, and magnetic properties of $La_{1-\delta}Mn_{1-\delta}O_3$ thin films*, Journal of Applied Physics, Vol. **11**, p. 6327-6330, **1999**.

[76] A. Ohtomo and H. Y. Hwang, *A high-mobility electron gas at the $LaAiO_3/SrTiO_3$ heterointerface*, Nature, Vol. **427**, p. 423-426, **2004**.

[77] N. Reyren, S. Thiel et al., *Superconducting interfaces between insulating oxides*, Science, Vol. **317**, p. 1196-1199, **2007**.

[78] A. Brinkman, M. Huijben et al., *Magnetic effects at the interface between nonmagnetic oxides*, Nature Materials, Vol. **6**, p. 493-496, **2007**.

[79] N. Nakagawa, H. Y. Hwang and D. A. Muller, *Why some interfaces cannot be sharp*, Nature Materials, Vol. **5**, p. 204-209, **2006**.

[80] A. Kalabukhov, T. Claeson et al., *Inhomogeneous microstructure and electrical transport properties at the $LaAlO_3/SrTiO_3$ interface*, Japanese Journal of Applied Physics, Vol. **51**, p. 11PG10, **2012**.

[81] P. Perna, D. Maccariello et al., *Conducting interfaces between band insulating oxides: The $LaGaO_3/SrTiO_3$ heterostructure*, Applied Physics Letters, Vol. **97**, p. 152111, **2010**.

[82] J. A. Mundy, Y. Hikita et al., *Visualizing the interfacial evolution from charge compensation to metallic screening across the manganite metal-insulator transition*, Nature Communications, Vol. **4**, p. 3464, **2014**.

[83] S. Thiel, G. Hammerl et al., *Tunable quasi-two-dimensional electron gases in oxide heterostructures*, Science, Vol. **313**, p. 1942-1945, **2006**.

[84] S. Smadici, P. Abbamonte et al., *Electronic reconstruction at $SrMnO_3$-$LaMnO_3$ superlattice interaces*, Physical Review Letters, Vol. **99**, p. 196404, **2010**.

[85] B. R. K. Nanda and S. Satpathy, *Polar catastrophe, electron leakage, and magnetic ordering at the $LaMnO_3/SrMnO_3$ interface*, Physical Review B, Vol. **81**, p. 224408, **2007**.

[86] A. Chainani, M. Mathew and D. D. Sarma, *Electron spectroscopic investigation of the semiconductor-metal transition in $La_{1-x}Sr_xMnO_3$*, Physical Review B, Vol. **47**, p. 15397-15403, **1993**.

[87] J. R. Kirtley, M. B. Ketchen et al., *High-resolution scanning SQUID microscope*, Applied Physics Letters, Vol. **66**, p. 1138-1140, **1995**.

[88] M. Adamo, C. Nappi and E. Sarnelli, *Magnetic dipole imaging by a scanning magnetic microscope*, Measurement Science and Technology, Vol. **19**, p. 015508, **2007**.

[89] D. A. Dikin, M. Mehta et al., *Coexistence of superconductivity and ferromagnetism in two dimensions*, Physical Review Letters, Vol. **107**, p. 056802, **2011**.

[90] J. Bert, B. Kalisky et al., *Direct imaging of the coexistence of ferromagnetism and superconductivity at the $LaAlO_3/SrTiO_3$ interface*, Nature Physics, Vol. **7**, p. 767-771, **2011**.

[91] S. S. Saxena, P. Agarwal et al., *Superconductivity on the border of itinerant-electron ferromagnetism in UGe_2*, Nature, Vol. **406**, p. 587-592, **2000**.

[92] D. Aoki, A. Hugley et al., *Coexistence of superconductivity and ferromagnetism in URhGe*, Nature, Vol. **413**, p. 613-616, **2001**.

[93] C. Kittel, *Introduction to solid state physics*, John Wiley & Sons, **2005**.

[94] J. L. Starck, E. Pantin and F. Murtagh, *Deconvolution in astronomy: A review*, Publications of the Astronomical Society of the Pacific, Vol. **114**, p. 1051-1069, **2002**.

[95] A. F. Carley and R. W. Joyner, *The application of deconvolution methods in electron spectroscopy - A review*, Journal of Electron Spectroscopy and Related Phenomena, Vol. **16**, p. 1-23, **1978**.

[96] A. Levin, Y. Weiss et al., *Understanding and evaluating blind deconvolution algorithms*, IEEE Conference on Computer Vision and Pattern Recognition, Vol. **1**, p. 1964-1971, **2009**.

[97] D. Kundur and D. Hatzinakos, *Blind image deconvolution*, IEEE Signal Processing Magazine, Vol. **13**, p. 43-64, **1996**.

[98] M. Hayashi, T. Kaiwa et al., *On mathematical methods to improve imaging of vortices using scanning superconducting quantum interferometer device (SQUID) microscope*, Physica C, Vol. **468**, p. 801-804, **2008**.

[99] B. J. Roth, N. G. Seulveda and J. P. Wikswo, *Using a magnetometer to image a two-dimensional current distribution*, Journal of Applied Physics, Vol. **65**, p. 361-372, **1988**.

[100] S. Chatraphorn, E. F. Fleet and F. C. Wellstood, *Relationship between spatial resolution and noise in scanning superconducting quantum interference device microscopy*, Journal of Applied Physics, Vol. **92**, p. 4731-4740, **2002**.

[101] R. W. Cole, T. Jinadasa and C. M. Brown, *Measuring and interpreting point spread functions to determine confocal microscope resolution and ensure quality control*, Nature Protocols, Vol. **6**, p. 1021-1941, **2011**.

[102] G. R. Ayers and J. C. Dainty, *Iterative blind deconvolution method and its applications*, Optics Letters, Vol. **13**, p. 547-549, **1988**.

[103] L. B. Lucy, *An iterative technique for the rectification of observed distributions*, The Astronomical Journal, Vol. **79**, p. 745-754, **1974**.

[104] W. H. Richardson, *Bayesian-based iterative method of image restoration*, Journal of the Optical Society of America, Vol. **62**, p. 55-59, **1972**.

[105] M. Piana and M. Bertero, *Regularized deconvolution of multiple images of the same object*, Journal of the Optical Society of America A, Vol. **13**, p. 1516-1523, **1996**.

[106] A. Mosleh, J. M. P. Langlois and P. Green, *Image deconvolution ringing artifact detection and removal via PSF frequency analysis*, Lecture Notes in Computer Science, Vol. **8692**, p. 247-262, **2014**.

[107] Y. L. You and M. Kaveh, *Ringing reduction in image restoration by orientation-selective regularization*, IEEE Signal Processing Letters, Vol. **3**, p. 29-31, **1996**.

[108] R. L. Lagendijk, J. Biemond and D. E. Boekee, *Regularized iterative image restoration with ringing reduction*, IEEE Transactions on Acoustics, Speech, and Signal Processing, Vol. **36**, p. 1874-1888, **1988**.

[109] L. B. Steren, M. Sirena and J. Guimpel, *Magnetic ordered phase in $La_{0.6}Sr_{0.4}MnO_3$ ferromagnets*, Physical Review B, Vol. **65**, p. 094431, **2002**.

[110] G. Koster, B. L. Kropman et al., *Quasi-ideal strontium titanate crystal surfaces through formation of strontium hydroxide*, Applied Physics Letters, Vol. **73**, p. 2920-2922, **1998**.

[111] R. Zhao, K. Jin et al., *The oxygen vacancy effect on the magnetic property of the $LaMnO_{3-\delta}$ thin films*, Physical Review Letters, Vol. **102**, p. 122402, **2013**.

[112] M. J. Aziz, *Film growth mechanisms in pulsed laser deposition*, Applied Physics A, Vol. **93**, p. 579-587, **2008**.

[113] M. R. Ibarrra, J. M. De Teresa et al., *Influence of oxygen content on the structural magnetotransport, and magnetic properties of $LaMnO_{3+\delta}$*, Physical Review B, Vol. **56**, p. 8902-8911, **1997**.

[114] J. Töpfer, J. P. Doumerc and J. C. Grenier, *Investigations on the charge transport in $LaMno_{3+\delta}$ at low temperatures*, Journal of Materials Chemistry, Vol. **6**, p. 1511-1516, **1996**.

[115] Z. Q. Liu, W. M. Lü et al., *Magnetic-field induced resistivity minimum with in-plane linear magnetoresistance of the Fermi liquid in $SrTiO_{3-x}$ single crystals*, Physical Review B, Vol. **85**, p. 155114, **2012**.

[116] B. Kalisky, J. A. Bert et al., *Critical thickness for ferromagnetism in $LaAlO_3/SrTiO_3$ heterostructures*, Nature Communications, Vol. **3**, p. 922, **2012**.

[117] N. Bagdassarov and H. Pinkerton, *Transient penomena in vesicular lava flows based on laboratory experiments with analogue materials*, Journal of Volcanology and Geothermal Research, Vol. **132**, p. 115-136, **2004**.

[118] D. Lattard, R. Engelman et al., *Curie temperatures of synthetic titanomagnetites in the Fe-Ti-O system: Effects of composition, crystal chemistry, and thermomagnetic methods*, Journal of Geophysical Research, Vol. **111**, p. B12S28, **2006**.

[119] D. Griffiths, *Introduction to electrodynamics*, Pearson Benjamin Cummings, **2008**.

[120] R. Pentcheva, M. Huijben et al., *Parallel electron-hole bilayer conductivity from electronic interface reconstruction*, Physical Review Letters, Vol. **104**, p. 166804, **2010**.

[121] N. C. Koshnick, M. E. Huber et al., *A terraced scanning superconducting quantum interference device susceptometer with submicron pickup loops*, Applied Physics Letters, Vol. **93**, p. 243101, **2008**.

[122] A. Finkler, Y. Segev et al., *Self-aligned nanoscale SQUID on a tip*, Nano Letters, Vol. **10**, p. 1046=1049, **2010**.

Appendices

A. Labview software replacement

During the course of this project, new control software for the SSM was written. The old software, while functional, was not user-friendly and prone to errors and crashes. Beyond that, we wanted to create software that would be accessible for other users of the system, and would allow for adding new or extending existing functions easily. An additional advantage would be that complete control of the SSM (which includes calibration of the FLL) could then be done on a single pc instead of two.

The software was created in Labview, a programming environment most experimenters are familiar with. The basic program should be able to do at least two things: approach the sample with the sensor, and perform a scan. Users should be able to set various parameters, such as the size of the scan, the resolution, coordinates, etc. It should also output the data in a format that can be used by data processing software such as Matlab, Origin or Gwyddion. The old software saved the data in a binary file, which required a separate Matlab script to convert into a .txt file before the data could be used.

The first function, approach, allows the user to bring the sensor into contact with the sample surface. The interface (at time of writing) can be seen in Figure A.1. At each step, the program will perform a line scan along the x-direction, displaying the data on-screen. The three buttons allow the user to control the height (z) of the sensor: the *Approach* and *Withdraw* button respectively decrease and increase the sensor-sample distance by an amount equal to *Step Size*. The third button, *Redo line*, will not change z, but instead perform another line scan at the same height. This is useful if the gain has to be changed or if the sensor needs to be calibrated again. *BKLSH* is a buffer added at the start of each line scan to allow the motors to accelerate to the correct speed.

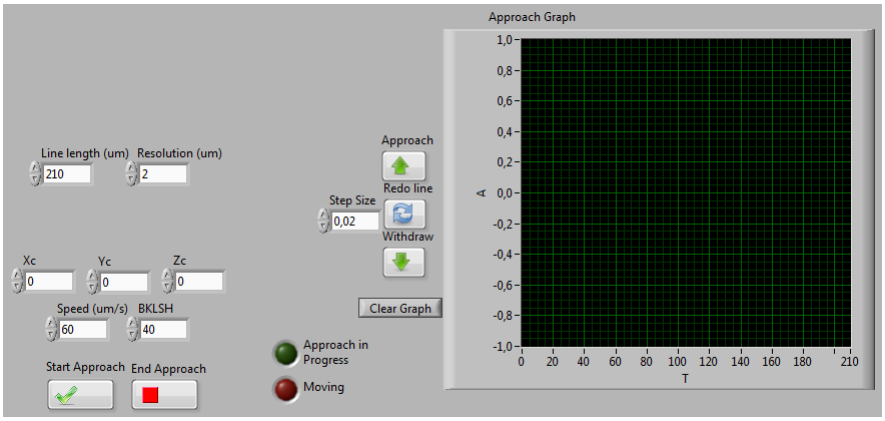

Figure A.1: Interface of the approach function.

The second main feature is, of course, the scanning. The interface for this can be seen in Figure A.2. The user can indicate a file name and location where the data should be saved, set the coordinates and size of the scan, the scan resolution and speed. The left graph will show the current line scan, the graph on the right will display a rough overview of the total scan.

Testing scans were performed to check if the software worked correctly. A scan of $La_{2-x}Sr_xCuO_4$ (LSCO), a high-T_c superconductor, was done to create an image of flux

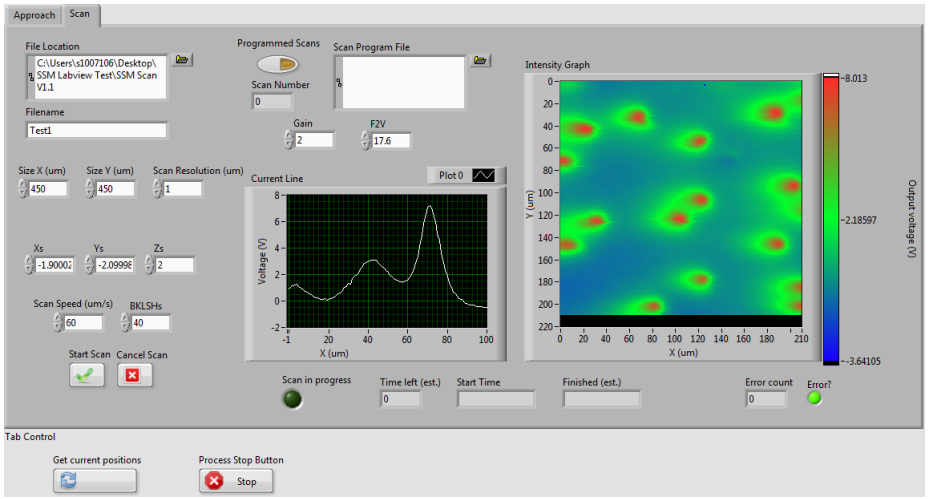

Figure A.2: Interface of the scanning function.

vortices. A flux vortex contains exactly 1 flux quantum (Φ_0), should therefore be a good way to see if the obtained results are accurate. The scan can be seen in Figure A.3.

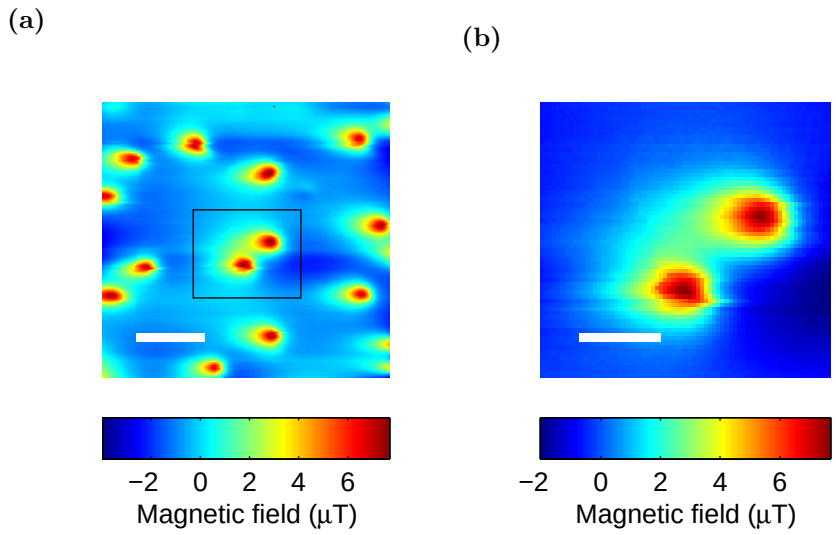

Figure A.3: a) SSM scan of an LSCO surface, showing vortices. b) The two vortices outlined in (a) were selected to analyse.

The individual vortices are clearly visible. By selecting one and summing up the flux of each data point, the total flux should be (as mentioned) 1 Φ_0. For analysis, the vortex pair in the centre of Figure A.3a was chosen, as seen in Fig. A.3b. We expect a total flux of 2 Φ_0: the total measured flux was about 1.90 Φ_0 (or 0.95 Φ_0 per vortex), which, considering the rough analysis and the variation in sensors as mentioned in the main text, leads us to believe the software is measuring properly.

At the end of each scan, the program will write an entry into a log file, with all the settings (size, resolution, scan location, etc.) that were used (see Figure A.4). This is done for two reasons: to keep an overview of who used the system when and how, and to allow for a user to check their settings (or someone else's) at a later time, in case they want to repeat their experiment with the same settings or if they forgot which settings they used.

Another feature allows the user to program a series of scans in advance, which the

Filename	Date	Start Time	End Time	Size x	Size y
LMO 8uc	17-2-2015	1:16 PM	1:27 PM	450	450
ALMO 8uc	17-2-2015	1:28 PM	2:02 PM	210	210
BLMO 8uc(z+0.02)	17-2-2015	2:04 PM	2:38 PM	210	210
BLMO 8uc(z+0.06)	17-2-2015	2:40 PM	3:14 PM	210	210
BLMO 8uc(z+0.1)	17-2-2015	3:22 PM	3:56 PM	210	210

Figure A.4: Screenshot of part of the SSM log file, automatically updated by the new software.

software will automatically perform one after another. The user can create a list of parameters for each scan, which the software will read and execute. The data for each scan is saved in a separate file. This enables the user to keep scanning while absent, for example during the night or weekend.

Now that the SSM control software is written in a more accessible format, adding new features to it should be feasible for most users with some skill in Labview. A possible addition can be to build in control for electric and/or magnetic field sweep measurements.

B. RSM scans for the pressure series

This appendix contains the reciprocal space maps for the other samples in the pressure series from Chapter 5. The RSM data of the 10^{-2} sample can be found in Section 5.2.

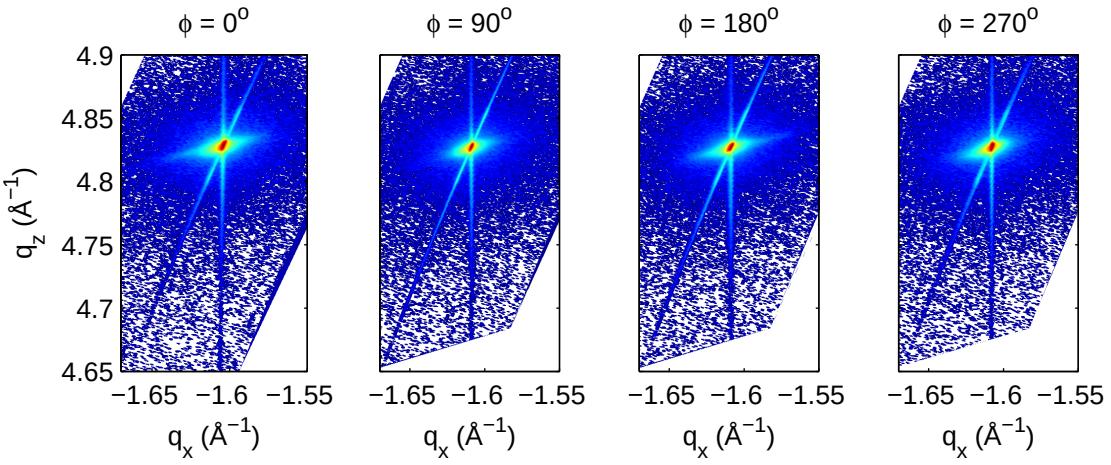

Figure B.1: Reciprocal space map of the $P_{O_2} = 10^{-1}$ Torr sample around the STO(103) peak.

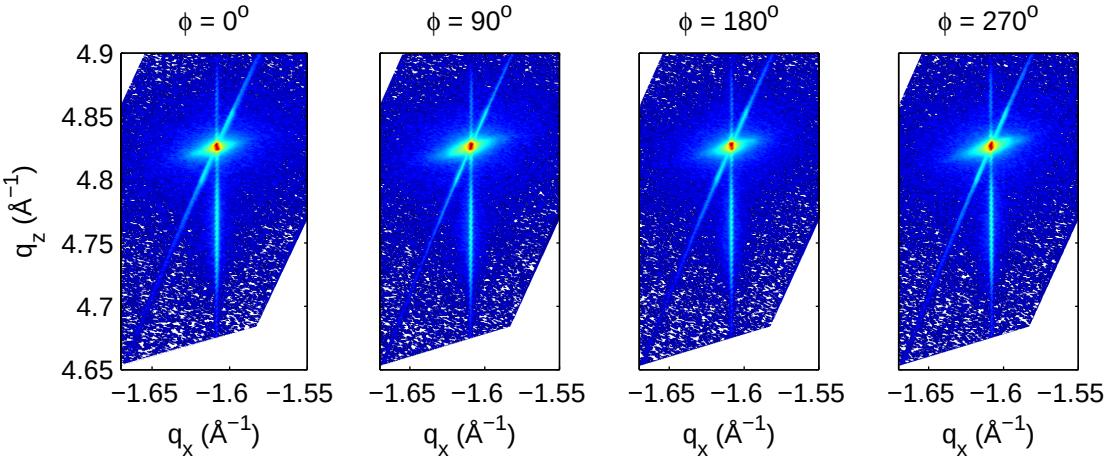

Figure B.2: Reciprocal space map of the $P_{O_2} = 10^{-3}$ Torr sample around the STO(103) peak.

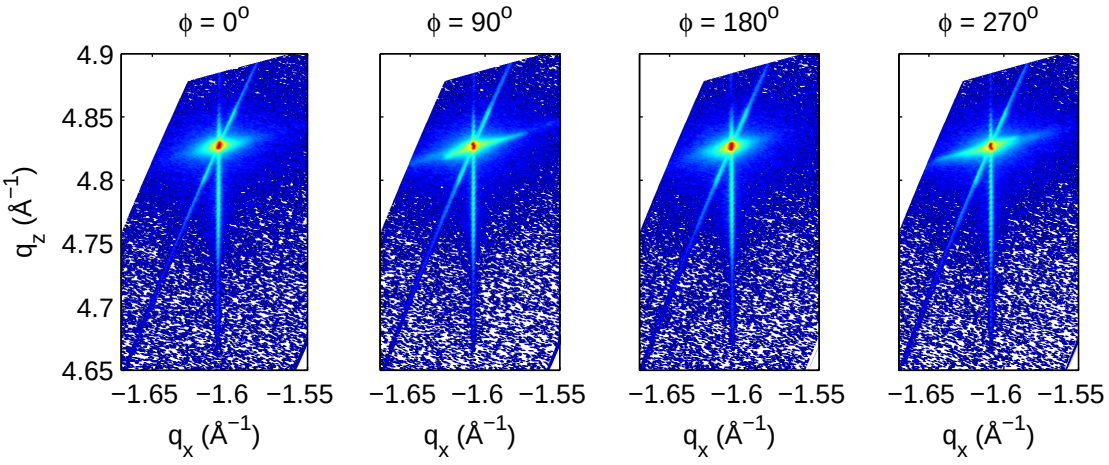

Figure B.3: Reciprocal space map of the $P_{O_2} = 10^{-4}$ Torr sample around the STO(103) peak.

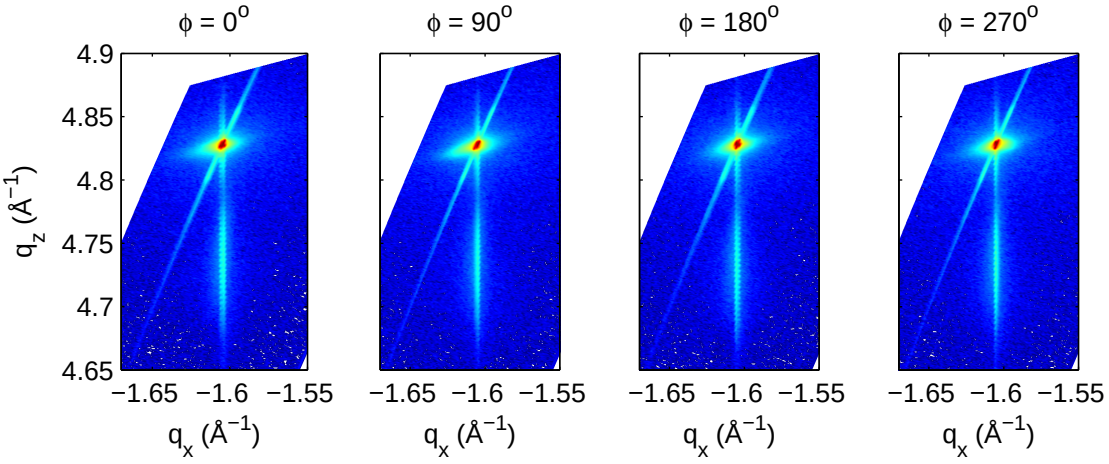

Figure B.4: Reciprocal space map of the $P_{O_2} = 10^{-5}$ Torr sample around the STO(103) peak.

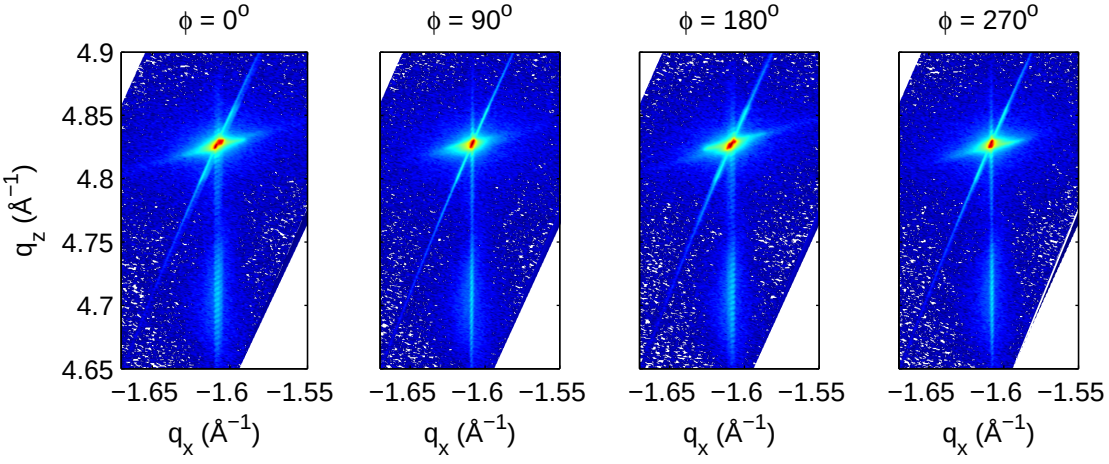

Figure B.5: Reciprocal space map of the $P_{O_2} = 3 * 10^{-6}$ Torr sample around the STO(103) peak.

C. SSM Manual

This appendix contains a manual for the SSM system. The existing manual was out of date, and various useful pieces of information were missing. This manual was written to have all of the basic information necessary to operate the SSM in one place.

ICE SSM Manual

Author: Pim Reith
September 19, 2014

Interfaces and Correlated Electron Systems (ICE)
Faculty of Science and Technology
University of Twente

Contents

Chapter 1

Introduction

This manual is an attempt to create an exhaustive guide to operating the Scanning SQUID Microscope (SSM). This was done as a reaction to all information being spread out over several logbooks, computers, emails and folders. It covers preparing the sensor, mounting the sensor and your sample, and performing SSM measurements and basic data analysis. All basic relevant schematics are also present.

The manual will assume you are familiar with various lab procedures (working with liquid Helium, operating the wire-bonder, using certain chemicals, etc.), and will only cover issues specific to the SSM setup. This includes safety protocols!

Each section has a reserved space to make notes, in case errors are made in this text or things have changed that need mention. This space can also be used to provide extra information users after you might find useful. A digital LaTeXversion can be found on the computer located at the SSM setup, in case any larger scale changes are made to the system. Please try to keep this document updated, if not for yourself then for users after you!

Note that even though it covers most aspects of the SSM, this manual is not sufficient to safely operate the setup, and training by someone with knowledge of the system (be it another user or somebody of the technical staff) is recommended.

1.1 Acknowledgements

The text, data and images in this manual have been compiled from personal knowledge and several existing documents and texts. Most of the credit goes to the following references:

1. C.J.M. Verwijs, *Fractional flux quanta in High-T_c/Low-T_c superconducting structures*, Ph.D. Thesis, University of Twente, 2009

2. A.G.P. Troeman, *NanoSQUID magnetometers and high resolution scanning SQUID microscopy*, Ph.D. Thesis, University of Twente, 2007

3. T. Wijnands, *Scanning superconducting quantum interference device microscopy*, M.Sc. Thesis, University of Twente, 2013

4. R. Bruel and A. Timmermans, *Magnetic flux quanta in High-T_c/Low-T_c superconducting rings with π-phase-shifts*, B.Sc thesis, University of Twente, 2013

Chapter 2

General overview

Scanning SQUID Microscopy (SSM) is a form of Scanning Probe Microscopy (SPM), used to scan the surface of a sample and obtain local magnetic flux data. To do this, it makes use of two parallel Josephson Junctions. This chapter will give a very rough description of the physics behind SSM, and a small overview of the setup. More details and derivations can be found in other works.

2.1 dc SQUIDs

A SQUID (Superconducting QUantum Interference Device) is comprised of two parallel Josephson Junctions. Such a junction is formed when two pieces of superconducting material are separated by a so-called 'weak link', usually an insulator. If this weak link is small enough, the superconducting wave functions can overlap (since they extend outside the superconductor for a region of size of the coherence length), allowing a supercurrent to flow through the weak link. Since the two wavefunctions each have their own phase component, there is a phase difference ϕ across the junction.

One can show that for any superconducting ring, the magnetic flux penetrating that ring has to be quantized. These units of flux, called flux quanta, have a value of $\Phi_0 = h/2e = 2.07{*}10^{-15}\ Tm^2$. When flux passes through a superconducting ring, currents will start flowing in the ring that will create a field of their own, compensating (or enhancing) the field to make sure the flux is quantized. When the ring contains Josephson Junctions, like a SQUID does, these currents can become higher than the critical current (since SQUIDs are typically biased with a bias current, only a small induced current is required for this), causing a voltage to appear. This voltage, then, is a measurement for the amount of flux passing through the ring.

2.2 Flux locked loop

As mentioned, a dc SQUID is usually biased with a bias current. At this point, it has a sinusoidal flux-voltage relation. For very small flux changes (less than approximately Φ_0/π), a SQUID can be biased to the steepest part of the flux-voltage relation to linearize it. For larger value changes, however, it is necessary to create a so-called flux locked loop (FLL).

There are several different methods of creating an FLL, but all involve a feedback circuit and a working point. Whenever the system deviates from the working point (i.e., when the flux through the pickup loop changes), the difference is fed back into the pickup loop via the feedback coil to put the system back at the working point. This ensures

optimal response of the SSM and simultaneously extends the flux range in which the SSM can operate.

2.3 Pickup loop

For SSM, a SQUID is usually extended with a pickup loop. This is formed by two superconducting leads, ending in a small ring, placed in series with the Josephson Junctions. Next, the actual SQUID itself is magnetically shielded (using superconducting material). Since the pickup loop has a well-defined area, and flux can only penetrate the circuitry through the loop, flux can be measured more accurately.

2.4 Experimental setup

A schematic view of the SSM setup at ICE can be seen below. In this setup, the sensor is fixed while the sample moves around. This movement is done through a set of three actuators (one for each of x, y and z) and a lever. A commonly used alternative is by using piezoelectric scanners. The sensor is positioned on a flexible cantilever located underneath the sample. This cantilever also connects the SQUID circuitry on the sensor to the external electronics through the sensor holder.

The whole setup is mounted on a shaft, which allows for it to be lowered into a cryostat cooled with liquid Helium (4.2 K). This is of course done to make sure the superconducting material in the SQUID is in the superconducting state.

The sensor and cantilever have to be prepared and connected by hand. Unfortunately, this can be a long and frustrating thing to do. The sensors are extremely fragile and small, so careful handling is a must. But even then there is no guarantee that your sensor will work. Don't be alarmed if you go for days (or even weeks) without getting a functional sensor. Patience is key.

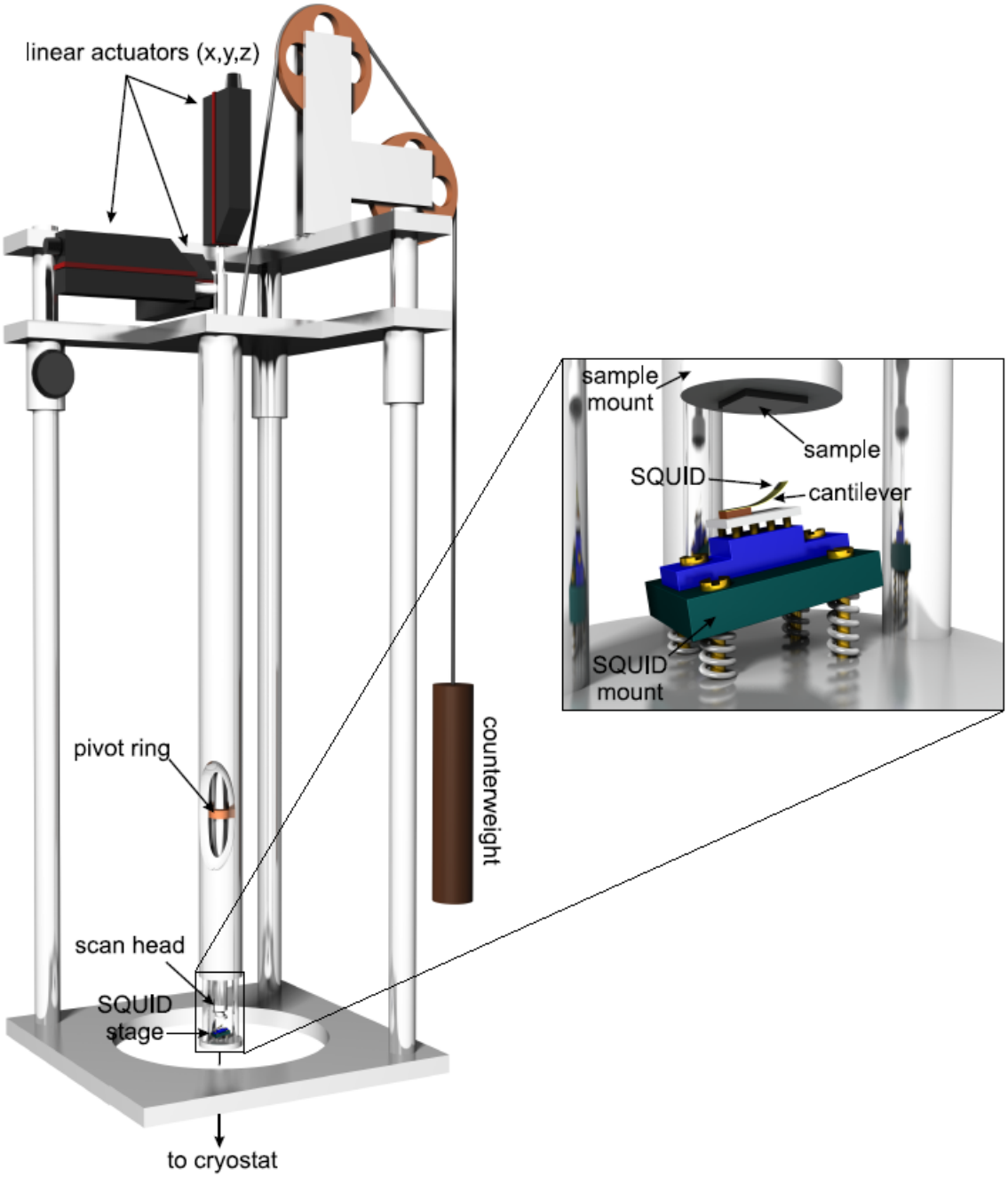

Figure 2.1: Schematic overview of the SSM setup at ICE. The external magnetic field coil is not shown for clarity. Adapted from [1]

Chapter 3

Preparation

This chapter will deal with preparing the cantilever, sensor and sample. This is all done in the sputter lab and the chemical lab in the Nanolab. It concludes with mounting everything on the setup.

3.1 Cantilever preparation

The first step is to prepare a cantilever. Normally a cantilever will last longer than sensors, but will need replacement from time to time. The cantilever is made out of plastic with copper leads deposited onto it. It must be cut (using regular scissors) from a plastic sheet which has several different patterns on it. The correct pattern to use for the cantilever is shown in the photograph below.

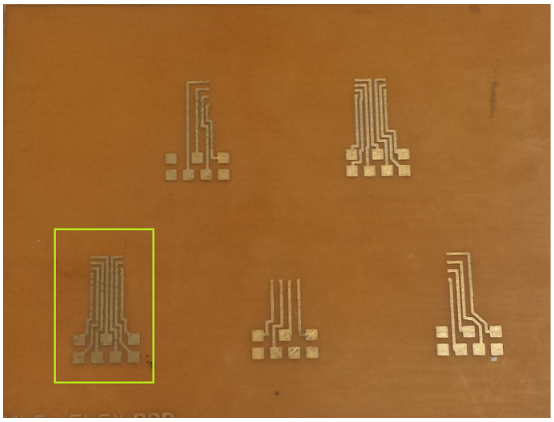

As one can see, the pattern has 7 leads, each connected to a small contact pad. The sensor, however, will only require 6 connections out of these 7. The cantilever should be cut into a specific shape, seen below. This is to minimize the risk of the upper corners coming into contact with the sample during measurement. Be sure to leave enough room below the contact pads to make the holes that will allow the cantilever to be fixed to the holder. Use an old cantilever as an example if you are unsure.

To drill the holes, there should be a small drill bit and a holder in the box. Place the cantilever under the PDMS (the "transparent rubber") and use the guides to drill the holes.

Next, the wires need to be soldered to the cantilever. The wires are made out of copper with a transparent insulation layer. The wires will probably need to be removed

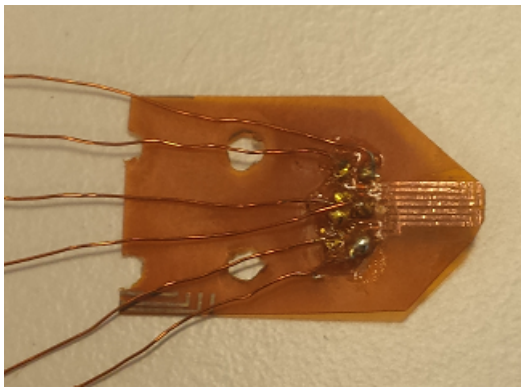

from the old cantilever first if they are not already. They can then be soldered to the new one. Be warned that the heat of the soldering iron can cause the copper to let go of the plastic. Remember that only 6 out of the 7 leads are needed, so there is some room for mistakes.

After soldering, use a multimeter to make sure none of the leads are shorted with another. Also make a note of which of the 7 leads you are not using. Note: never solder while a sensor is bonded to the leads. The soldering iron creates currents that can destroy the sensitive circuitry.

Now the cantilever can be connected to the circuit board on the holder. For this, refer to the images below and the schematic in Appendix A. There are three sets of two contacts: Modulation (M), current (I) and voltage (V). Each set has a positive (+) and negative (-) contact. Labeling the leads from left to right, the standard used is M+, M-, I+, V+, I-, V-. Although the wiring can be done slightly differently, it is best to use this standard to avoid confusion.

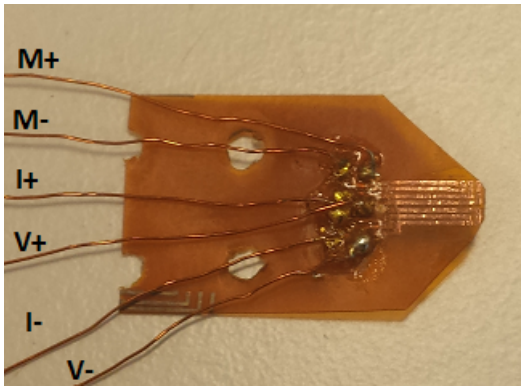

Finally, the last thing to do is to clean the cantilever. The copper leads can be cleaned with the fiber pen (which should be located at the wire-bonder). Then clean the whole cantilever using acetone and ethanol. Having the cantilever, and especially the copper leads, as clean as possible is crucial to wire-bond the sensor later on.

3.2 Preparing the sensor

The sensors, as obtained from the supplier, are not suitable for using in the setup. The circuitry is deposited in the center of a small rectangular substrate, which means there will be a significant amount of space between the pickup loop and the edge of the

substrate. The whole sensor is also covered with photoresist, to protect it against dirt and scratches. Since we want to have the pickup loop as close to the sample as possible, it is necessary to polish the sensor. The sensor will be polished to a point to make sure the distance between pickup loop and sample is as small as can be. See the image below for a sensor after polishing.

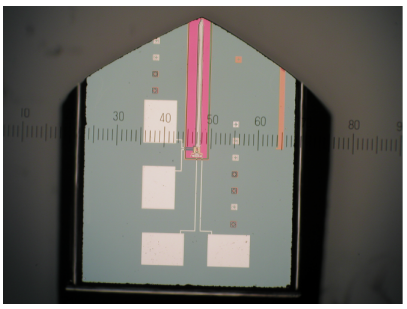

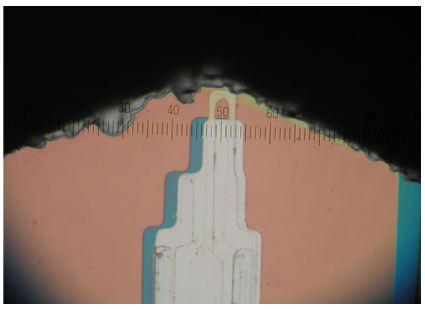

The polishing is done using a Dremel power tool, which is fastened to the table using a clamp. Since the sensor is so small, it is held in an alligator clip ("krokodillenbekje") which in turn is mounted onto a holder (see image below). Since the circuitry is sensitive, the sharp teeth of the clip are covered with PLD target glue to smoothen the surface.

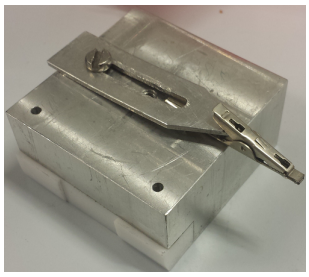

Make sure that when the unpolished sensor is in the clip, it extends far enough so that it can be grinded properly, yet is in deep enough so it will move as little as possible. After this, cover the bottom and sides of the sensor and clip with wax. Since the polishing process will generate a lot of heat, the wax is used to dissipate this. The wax will also reduce the risk of the sensor moving around while polishing.

Position the Dremel underneath the overhead microscope and make sure it's set to the lowest speed. Before starting the tool, check that you can see both the sandpaper and the sensor (especially the pickup loop). Although the vibrations caused by the Dremel will make it impossible to keep the sensor in focus, you should still be able to see the pickup loop during polishing.

While polishing, use a tapping motion instead of holding the sensor to the sandpaper. This is to minimize the buildup of heat, which can cause the wax to melt and the sensor to move. It is likely that polishing debris (wax, sensor) will end up on top of the sensor, obscuring your vision. If this happens, use a tissue and some water to clean it. If this doesn't help, you can also use acetone, but remember that using acetone will remove the protective photoresist layer, leaving the circuitry exposed.

Check your progress regularly, it is very easy to polish too much and destroy the pickup loop. If you are getting close, consider switching to fine sandpaper (grade p4000) and polishing the last bit by hand. In case too much wax is removed or the wax shatters, simply remove the remains and put on some new wax.

Once the polishing is done, remove the sensor from the clip using acetone. Remember

that at this point, the pickup loop is very close to the edge, so be extra careful the edges of the sensor don't collide with anything. The next step is to clean the sensor and prepare it for wire-bonding. First, clean the sensor with acetone and ethanol to remove the top photoresist layer. Next, glue the sensor to the top of the cantilever using GE varnish (which can be found in the refrigerator in the chemical lab). Remove any excess varnish using acetone, then bake it out to harden the glue.

The final step is to wire-bond the sensor to the cantilever. To do this easily, stick the cantilever to one of the plates at the wire-bonder using double-sided tape. You can make the tape less sticky by going over it with a finger several times. This will reduce the force needed to remove the cantilever later, and therefore reduce the risk of breaking the bonds. Make sure the cantilever is stuck properly. The cantilever is made to be flexible, and if it is loose, it will absorb the vibrations the wire-bonder uses to make the bonds, making it impossible to wire-bond.

Since the holder is attached to the cantilever through the copper wires, you will probably need to raise the holder by placing it on a small box so you don't have to hold it while bonding. Be careful when rotating, since if you don't rotate the holder with it, you might put too much stress on the wires.

The connections to be made with the wire-bonder are depicted in Appendix A. It is preferable to make two bonds per contact, as a safety precaution. Typical settings for the wire-bonder are a power between 4 and 5, and duration of 7 for both bonds, though you might find it necessary to play around with these values. Bonding can be done from sensor to cantilever or vice versa.

Keep in mind that the contacts are quite small. In case you are having trouble wire-bonding, you could run into the problem of having no more room to make bonds. This is especially the case for the I-V contact pads, since they require twice the amount of bonds. For those, a last resort option is to instead bond the two copper leads on the cantilever together (see image below). However, this will increase the resistance, so this is not preferable.

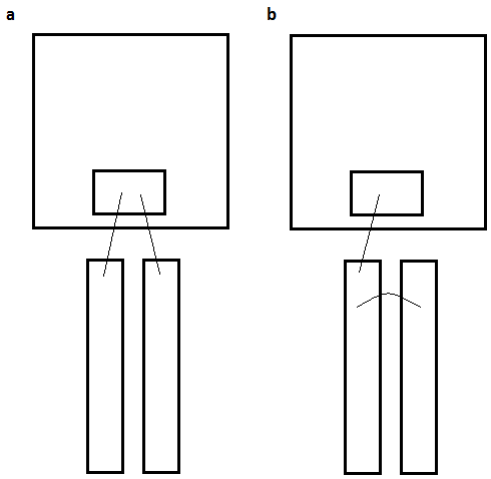

Figure 3.1: Scematic representation of two leads and a single I-V contact pad on the sensor. a) typical wire-bond connections. b) alternative connections.

Once all bonds are set, carefully remove the cantilever. To make sure all bonds are done properly and the sensor is still good, check all connections using a multimeter. Set the multimeter to the highest range (10 MΩ), otherwise you will destroy the sensor circuitry. In this range, the resistance values should be as found in Table 1 in Appendix

A in the row “After mounting”.

If the above is not the case, check the bonds if they are ok visually. If so, it is highly likely that the sensor is broken. This can happen during the polishing process, although it does happen that the sensor is already broken when brought in from the supplier. If all is well, fix the cantilever to the holder using the screws.

3.3 Preparing sample

Samples can simply be glued onto the sample holder using GE varnish. On the underside of the sample holder is a straight edge with which the sample should preferably be aligned. If your sample can withstand it, bake out the varnish, otherwise leave it to dry in air.

You preferably want to have the sample in the middle of the sample holder, though this may depend a bit on the shape of the cantilever, mostly its length.

3.4 Mounting sample and holder

Mount the holder before the sample, to minimize the risk of the sensor and/or the sample colliding with anything. The holder is connected to the setup using three screws. When tightening these screws, keep in mind that the screws and the screw holes have slightly different thermal expansion coefficients. This means that when you tighten the screws too much, they might get damaged when cooling and warming up again.

After fastening the holder, connect the cables to the circuit board. There are four cables: two with red connectors, and two with black ones (one male, one female). The two red connectors need to be connected to the holder. The two black ones are for the magnetic field coil, connect them together if you are going to apply a field during measurement. If not, tape the male connector to the holder using Teflon tape. Don’t leave it hanging loose, there are small openings on the inside of the cryostat where it might get stuck.

After mounting and connecting the holder, but before mounting the sample, make sure you retract the sensor a fair distance to give yourself enough room to mount the sample. To do this, power on the Newport Universal Motion Controller and move the z-axis in the positive direction. Positive z-values will increase the distance between sensor and sample. Keep this in mind when the setup is inside the cryostat.

To mount the sample holder, use the metal clip and a pair of angled tweezers. It should fit easily. After this, you can center the sensor x and y-axes above your sample (see the image in Appendix A for the directions). Try to keep the motors close to the middle of their range of motion. Since the setup is moved using a lever, the movement actually follows a circular path, which you will see in your images if you scan too close to the motor limits. In a worst case scenario, you can move the motors beyond the range of motion of the lever, causing the connection between the motor and the lever to be lost.

Note: do not lower the setup into the cryostat yet, there are a few things that need to be done outside the cryostat for your measurements.

3.5 Notes

Chapter 4

Measuring

This chapter describes how to perform a measurement, and includes cooling down the system, applying an external magnetic field, calibrating the sensor and some basic data processing.

4.1 Room temperature approach

The first step is performing a room temperature approach. Since the cryostat will block your vision and there aren't any microscopes or cameras, we need to do a rough approach outside the cryostat to prevent wasting a lot of time doing it later inside the cryostat.

To do this, use the Newport Controller to approach the sensor. Use the high-speed button for the large distance at first, then slow down once you get close. Be careful you don't crash the sensor into your sample!

Once you feel you are close enough, check the z-axis value on the Newport Controller and write it down. Then retract the sensor again a small distance. While lowering the setup, the cantilever might vibrate, causing the sensor to hit your sample if you do not retract. The z-value you wrote down is later used to put the sensor back close to the sample before doing the true approach.

This is also the last moment you can check the sensor before lowering the setup into the cryostat. Once the setup is inside the cryostat, you can use the PCI connector to check the sensor, using the image and table in Appendix A.

If you are not going to apply a magnetic field during your measurement, you can use the Nb shield to reduce the external noise. Using the shield, the field resolution will increase by roughly a factor of 2-3.

To mount the shield, you will have to raise the setup as far as possible. Then, carefully, move the setup a few centimeters in any direction. You need the little extra wiggle room to fit the shield. Next, open the cryostat, then carefully lower the shield into it before fitting it onto the wooden top part using the 3 brass screws.

4.2 Lowering and cooling

If the cryostat is not yet cold, you can opt to lower the setup before cooling, to save you from opening the cryostat later to lower it, saving a bit of Helium. If the system is already cold, lowering will work the same way.

First, before opening the cryostat, lower the lid on the shaft. This will let you close the cryostat faster, saving Helium. The lid is quite tight, so it will require a bit of force to get it down.

Next, open the cryostat, making sure the rubber ring remains in place. Then loosen the screw up on the shaft and slowly start lowering the setup into the cryostat. The setup is balanced by a counterweight, so you won't be able to accidentally let it fall down. You will feel it starting to vibrate if you move too fast. If it does, slow down or stop until it stops shaking, then continue. Once lowered, close the cryostat with the clamp and tighten the screw again.

The setup is relatively high up in the cryostat now, this is on purpose. Lowering the sensor too quickly into the liquid Helium will cause a thermal shock. The sensor is built up from several different layers of insulating material and Nb shielding. These expand and contract differently. If they do this too fast, it can damage the sensor. Lowering the setup further into the cryostat should therefore be done slowly.

If the system isn't cold or needs refilling, you should do that now. There is a Helium level meter which will indicate (in percentages) how full the cryostat is. However, there is some discrepancy: if the level meter indicates 0%, there is still Helium left in the cryostat, it instead indicates the lowest level the sensor can reach. The level meter will drop below zero to indicate a completely empty cryostat.

The Helium will evaporate at a rate of approximately 0.3% per hour if the setup is outside the cryostat, and approximately 1.2% per hour if the setup is inside (the shaft acts as another heat conduit). Having the Helium level meter on will increase the evaporation rate (from 0.3% to about 1.0% per hour). A warm cryostat will take about 75 L to cool and fill to a reasonable level (about 60%).

Depending on the Helium level, you may need to lower the sensor more to make sure it's cooled below 9 K (the T_c for Nb). You will see numbered markers on one of the shafts: having the setup at 5 should usually be sufficient.

As soon as you hit the Helium, it will start evaporating into the Helium return piping, which will become cold and form droplets of water or even frost. Use this as a sign to know how far you are.

4.3 Tuning the sensor

The next step is to 'tune' the sensor. This will calibrate the modulation and bias currents to put the SQUID at the most sensitive part of the flux-voltage relation. First, connect the Star Cryoelectronics PCI connector to the setup and switch it on. Also turn on the function generator, the oscilloscope, the amplifier and, of course, the pc.

Make sure the amplifier gain is set to 1. On the function generator, the waveform should be 'ramp', the frequency 137 Hz, the amplitude 1.8 V, the offset 0 and the symmetry 50%. Make sure to turn on the output.

Next, load up the PCS100 Control Software on the pc (shown below). This is the program used to find the correct calibration values. Click 'TUNE', and turn on the Test Signal. The other values should be left as is, just make sure the Feedback is at 100 kΩ. Change the BIAS, MOD and PHASE values a few times until you can see the signal on the oscilloscope starts responding (moving up and down); hitting REFRESH should do the same. If it does not, check the connections and restart the program or the pc. If it still will not respond, it most likely means the sensor is broken and needs replacement. If you are using the Nb shield, remember that it needs to fill up to cool the sensor and only has a small hole in the bottom, so it might take a minute to fully cool.

Tune the sensor by adjusting the MOD, BIAS and PHASE values. The goal is to have the signal look like the sine-like shape in the image below. Keep changing the values until the amplitude is maximized (you can switch between COURSE and FINE to change

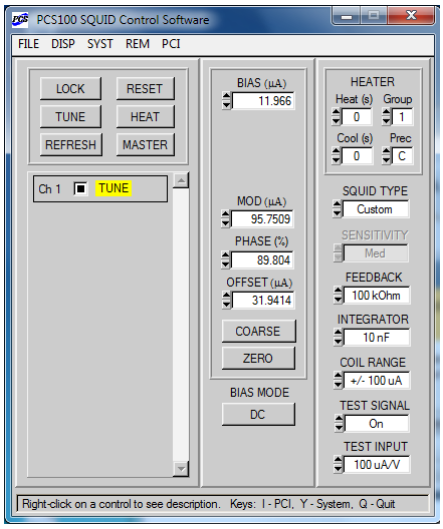

the step size). Typically, this means the BIAS will be between 10 and 20 μA, and the MOD will be somewhere in the 90 μA range. If the sine-like shape will not appear, you may need to lower the setup some more (it means the SQUID is not superconducting). If that doesn't fix it, it means the sensor is broken.

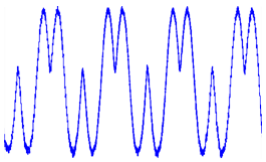

Now, click 'LOCK' to lock in these calibration values. You will see the output signal change from the shape above to a triangular shape. Change the OFFSET value to center the output signal, then write down the peak-to-peak voltage. This value is the conversion factor from voltage to flux, and is usually around 17.6.

Finally, turn off the Test Signal. All you should see now is noise. Center it again by changing the OFFSET value, then write down the noise peak-to-peak value, usually between 10 and 20 mV (you will have to zoom in a few steps on the oscilloscope). This will give you an indication of how much noise there is in the system during your measurements.

4.4 Approaching the sensor

The last step before measuring is to approach. For this, set the amplifier gain to 10.

Approaching and scanning is done using a Labview program, which should be located on the desktop if it's not already running. The two functions (approach and scan) each have their own tab. The approach tab looks like the figure below:

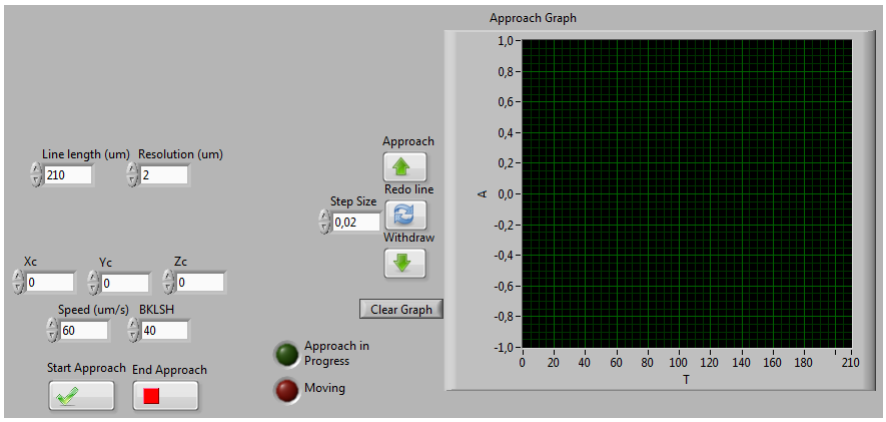

X_c, Y_c and Z_c are the starting coordinates. While approaching, the z-value will be changed first (by an amount equal to *step size*), and then a line scan will be made along the x-direction, with X_s as the centrepoint, with a length equal to *line length*. *Speed* is self-explanatory, and *BKLSH* is a small section added at the beginning of each line to allow for the motors to accelerate to the correct speed.

Z_s should be set to the value you wrote down before lowering the setup into the cryostat. X_c and Y_c can be copied from the Motion Controller display (since you centered it beforehand). After this, click *Start Approach*. The sensor will now move to the beginning of the first line. After this, you can use the up and down-arrow buttons (on-screen) to approach or withdraw respectively, or you can rescan the same line if you wish. The step size can be changed after every step. It's usually set to 0.02 μm, once you get closer you can change it to a smaller value.

Once you are close enough, you should see an obvious signal. Small wiggles on the lines are normal noise, the actual signal from your sample is very obvious. As you get closer, the amplitude of the signal increases, until the sensor comes into contact with the sample. At that point, the signal will move from left to right, but not change in amplitude. See the image below for a visual explanation.

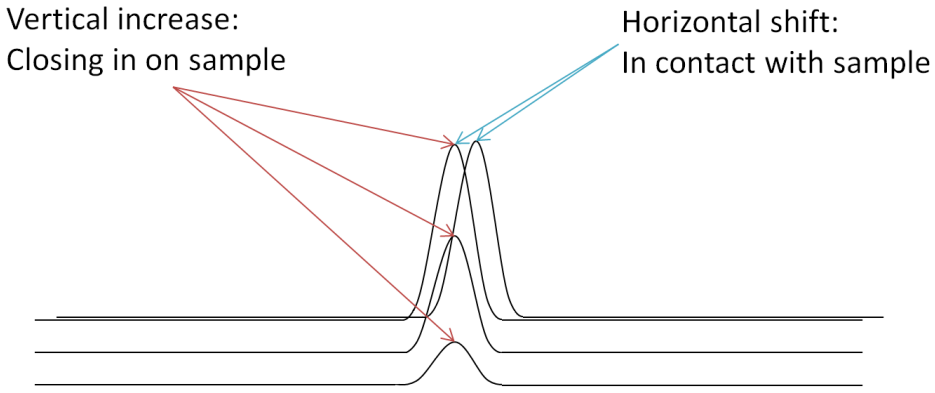

If the signal becomes too large (it gets cut off at the top), lower the amplifier gain. It is possible that even at the lowest gain value (1), the signal is still too large for the setup to measure. If this is the case, you can opt to change the feedback resistance (via the PCS100 software) from 100 kΩ down to 10 kΩ. This will decrease the output signal even more, but you will lose some sensitivity. If you do this, you will need to change the integrator capacitance from 1 nF to 10 nF to maintain the same RC-time. In extreme cases, the same holds for going down to 1 kΩ. Changing the feedback resistance will

change the flux-to-voltage ratio, so be sure to check its value.

If, after some time, you still do not see a signal appear, it might be that the sensor is broken (the other option being that there is no magnetic signal at all). Depending on how close your room temperature approach was, you will need to approach a larger or smaller distance. Note, however, that due to the low temperature, the cantilever will contract, which can change the actual distance between the sensor and the sample. Distances up to 1.5 mm have been experienced.

Once you are done, you can click *Stop Approach* to end the approach procedure. You do not need to stop the program itself.

4.5 Applying an external magnetic field

The SSM setup comes with a magnetic field coil connected to a current source to apply external fields to your sample during measurements. The coil has a diameter of 57.0 mm, is approximately 200 mm long and has 700 windings with a total resistance of approximate 61 Ω. Approximating the field using the field of an infinite coil, this would give a field of $4.4 * 10^{-3}\ T/A$. Calibration measurements have shown that at the center of the coil, the actual field is $4.2 * 10^{-3}\ T/A$. Positive currents will give a field pointing away from the earth's center, negative currents will give a field pointing towards it. The full calibration curve can be found in Appendix A.

To compensate for earth's magnetic field (in the z-direction), the applied field should be approximately -2.7 μT, corresponding to a current of -0.65 mA. The largest current that can be applied is about 6 A.

Applying a field can be done before cooling down (i.e., outside the cryostat), or after, depending on the specifics of your experiment.

4.6 Doing an electric field gating experiment in the SSM

To do an electric field gating experiment in the SSM, you can use the special sample holder (shown below) which can be connected to an external voltage source. Fix your sample to the holder, then wirebond the connections you need, then fix the holder to a regular sample holder in order to fix it to the SSM setup. The three-pin connector can be connected to its female counterpart which leads to an outside connector. Make sure the white markings on the pin line up. The outside connector is a five-pin connector, which can be connected to your voltage source.

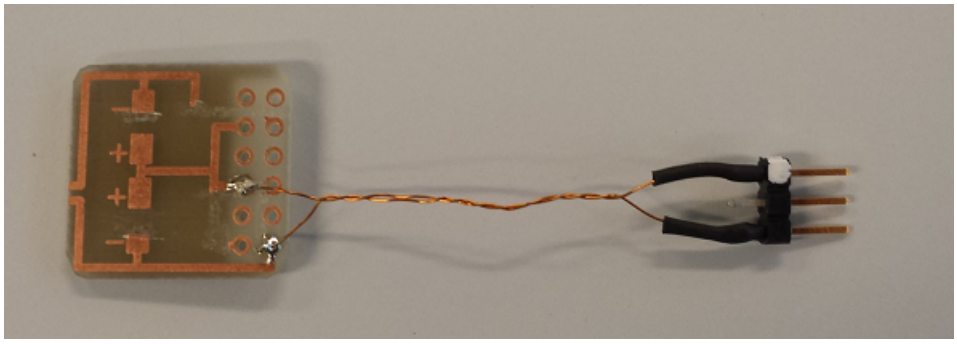

The cables running on the inside can handle a maximum voltage of about ±180 V.

4.7 Performing a measurement

Once the approach is done, it is time to do a measurement. Switch to the Scan tab in Labview, which looks like the image below:

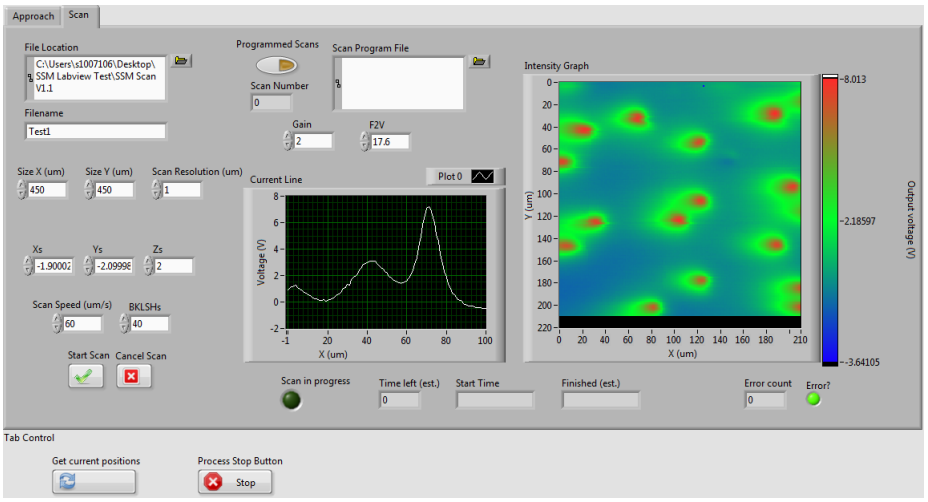

You can click the *Get Current Positions* button at the bottom to update the current motor positions, or you can copy the values from the Motion Controller display manually. Be extra careful you have the correct z-value. X_s and Y_s indicate the centre of the area you want to scan. *Size X* and *Size Y* are the dimensions of your scan, and *Scan Resolution* is the size of each pixel. Keep in mind that the actual spatial resolution is limited by the diameter of the pickup loop.

By clicking *Start Scan*, the system will automatically scan the indicated area. The program will also give an indication of how long the scan will take. Make sure you write down all the relevant data of your scan (such as the gain, the voltage-to-flux ratio, the dimensions and resolution, etc.). You will need these later when processing the data, and it is generally good practice!

A SSM log file is located in the same folder as the Labview program, and will automatically update itself after your scan is done. It contains all details of your scan, such as filename and location, scan size, resolution, etc. If you replace the sensor/cantilever, manually add a new line in the log to reflect this, to make it clear to all users when sensors are replaced.

The Labview program will automatically generate a simple image of the total scan. This will give you a rough idea of what the area you scanned looks like. The data presented there are raw voltages, not flux or magnetic field strength, nor has any other processing (background substraction, etc.) been done to it. It is the same data you will find in the data file.

If at any point the program fails to finish the scan or you interrupt it manually, the data up to that point should still be saved in the data file, should you need it.

In case you want to reposition the sensor on your sample, remember that movement is done through use of a lever, which has a 2:1 ratio. That means that when you move the x or y-motor by some value c, the actual movement across the sample surface is $c/2$. Or vice versa, if you want to move a distance c across the sample surface, you will need to change the motor position by $2c$. This is the only case where you need to keep the lever ratio in mind, the software incorporates the factor of 2 during normal scanning procedures.

Keep in mind that the SQUID is extremely sensitive, enough to pick up communication signals from phones and laptops. Therefore, it is best to turn these devices off, put them to flight mode or just leave them in your office. Since there will still be people walking around outside the lab, there will always be some noise coming from those sources. If you really want to make a precise scan, you will want to do it either in the evening or during the weekend, when fewer people will be about. Don't hesitate to remind other lab users to switch off their phones.

4.8 Programming a series of measurements

If you want to make multiple scans one after another without having to manually set up everything inbetween each scan, you can enable the *Programmed scans* function. Then create a small excel or text file, which has the formatting as shown in the image below:

Scan #	X	Y	Z	dX	dY	RES	BKLSH	Speed	Field	Gate V
1	-2	-3	2	100	100	1	40	60	0	0
2	-1	-3	2	100	100	1	40	60	0	0
3	-1	-2	2	100	100	1	40	60	0	0
4	-2	-2	2	100	100	1	40	60	0	0
5	-2	-2	2	100	100	1	40	60	0	0

For each scan you want the program to make, add a line with the parameters of the scan (make sure you include the top row with the column titles!). Then save your file as a .csv file. Then go back into the labview program and select your file there. Also make sure to still specify a saving location and a filename. Then simply press the *Start scan* button, and the program will do the rest. It will save the data of each scan with the name you specified, appending it with the number of the scan.

4.9 After measuring

Once you are done with your measurements, withdraw the sensor from the cantilever. Next, disconnect the PCI connector from the setup. If you did not pump down the system to go to lower temperatures, then simply remove the clamp closing the cryostat, loosen the screw and pull up the setup (again being wary of vibrations). As soon as the holder is clear of the cryostat, close it again.

In case you did pump down the system, the order of operations is simply reversed. First, close the Vacuum valve completely. Then, very slowly, open the Helium return valve (if you go too fast, you can simply close it to stop the venting process). Again, approximately every 150 mbar, remove one counterweight (check the table in Appendix A). Once you reach 1000 mbar, replace the last counterweight with the regular one. Then, at the pump, close the input line valve, and turn off the pump. The small exhaust valve should be left open! Close the doors and return the key to the cupboard. Now you can remove the setup as normal.

Since the setup is cold, it will create frost once outside. You can thaw this using a hairdryer and dry it with some tissue. Any remaining moisture will freeze again the next time you cool down the setup, which can damage the sensor, your sample or parts of the setup. In rare cases, frost can form on the pivot ring inside the shaft. If this happens, it blocks the movement (primarily in the z-direction) of the motors, so that you will not be able to scan. In this case, warm up the setup, and let nitrogen flow through the shaft (it is open on the bottom, right above the sample) to completely dry it.

4.10 Data processing

The software will give the voltage data in a .txt file. You can open this file with Gwyddion (or any other software for analysing scanning probe microscopy measurements) to remove scanning artifacts or substract a background, if you wish. There is a small header before the actual data starts: this is to allow Gwyddion to interpret the data correctly.

Then, to convert the voltage values into magnetic field values, use a second Matlab script named "ColormapBfield". Depending on which version you have, it will either give you a prompt to ask for several values, or you will need to enter them manually into the script. You will need to know the flux-to-voltage ratio, the gain and the resolution. The data in the .txt files are digital values of the output votlage V_L. To convert these digital values N back into actual flux values Φ, we use the following formula:

$$\Phi = \frac{1}{F * G} \frac{A_p}{A_s} * V \tag{4.1}$$

In this equation, F is the flux-to-voltage ratio, a characteristic of the FLL. G is the gain applied to the voltage signal before it's picked up by the computer. Finally, A_p is the area of one 'pixel' on the sample (defined as the resolution squared), and A_s is the effective area of the pickup loop after considering the angle and effects such as flux focusing.

This program will output a colormap image with the x and y-axes in meters, and the colorscale in μT. It will also save this image as a Matlab figure file in the same folder. The data can be found in the variable "Phi_B" (which is in Tesla). If you prefer, the flux data can be found in the variable "Phi_p", which is in units of Φ_0.

4.11 Final note on Labview software

This program was newly written to replace the old software that was created by Dr. J. Kirtley. The old software, even though it did what it should, was not user-friendly and often gave errors or crashed. A Labview replacement was made in November 2014 by Dr. A. Rastogi and P. Reith. Since Labview programming is easy to learn and known by most scientists, this software would allow users to easily add or extend functions if they so desire, something that would have been a lot harder to do with the old software. That said, it is always possible that errors or bugs can appear while using the program, which may or may not be critical enough to require fixing. If you do decide to change anything in the software, be sure to make a backup first, in case you need or want to revert to it later.

4.12 Notes

Appendices

Appendix A

Schematics

This appendix contains some useful schematics to refer to when performing various steps. Even once you feel comfortable with all the steps outlined in the manual, these will be a quick and easy reference.

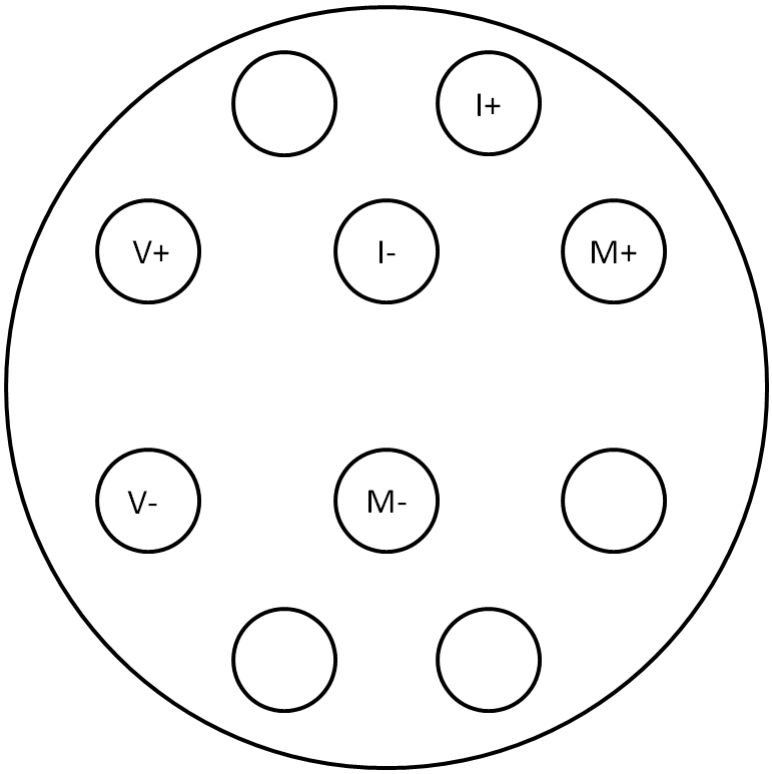

Figure A.1: Schematic of the 6 connection points on the female PCI connector

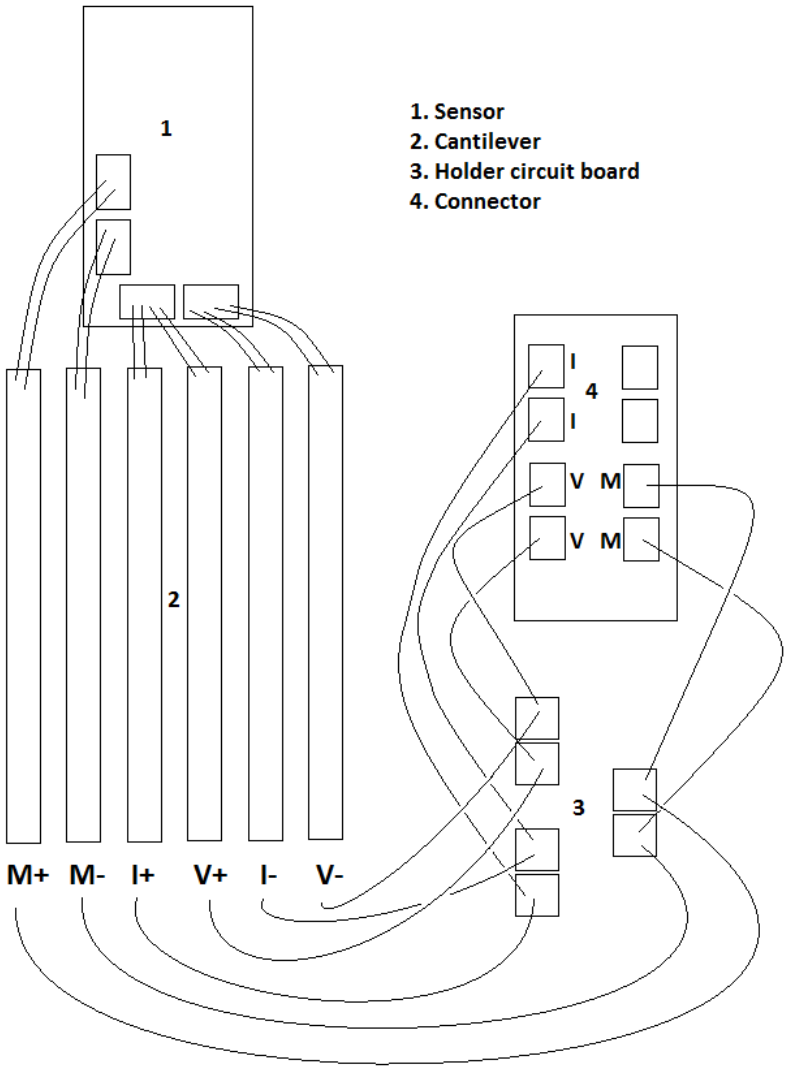

Figure A.2: Schematic of the connections from sensor to cantilever, and from cantilever to the holder

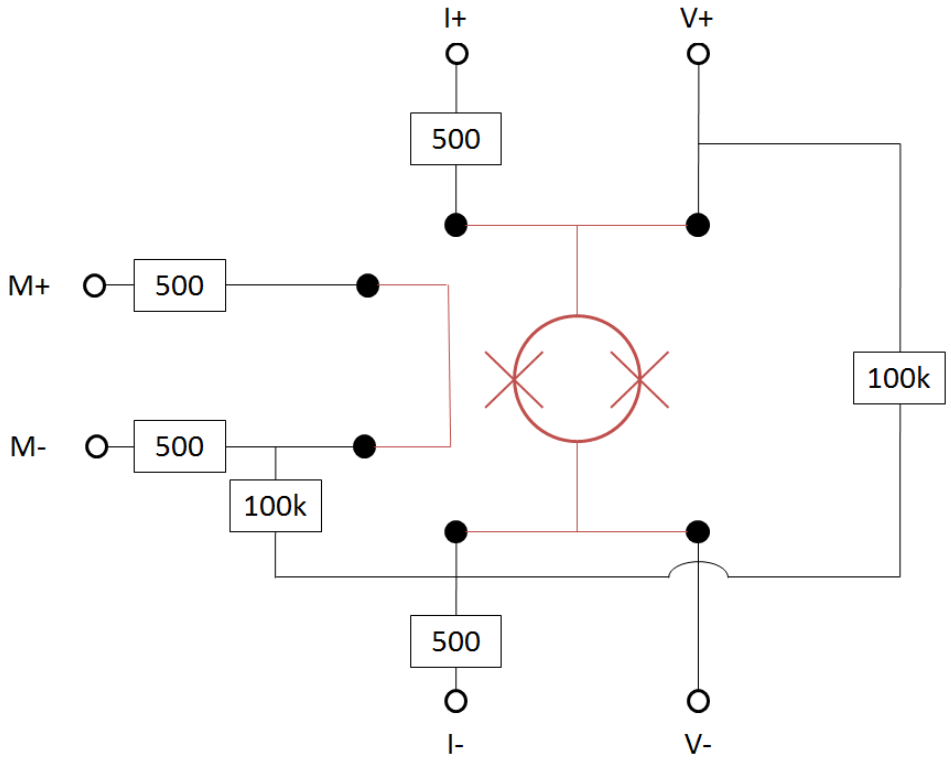

This image details the various connections and resistances of the complete circuit. The black lines are the connections on the circuit board, the red lines are connections on the sensor. The numeric values indicate resistances (in Ω). The open circles are the connection points on the red connector on the circuit board, the closed circles are the 6 soldering points on the circuit board.

Table 1 also shows the resistances between several points (in Ω). Since the multimeter must be used in the 10 MΩ range, the lower resistance values are denoted as 0 (since that is what you will read on the multimeter), instead of their actual values. Before mounting shows the values you should see if you want to check the sensor before polishing by bonding once to each of the four contact pads. After mounting are the values you should see when your sensor is fully prepared for measuring. The 100 kΩ values can be a little higher or lower (90-120 kΩ), this is normal.

	M+ to M- I+ to I- V+ to V-	I+ to V+ I- to V-	any M to any I	any M to any V
Before mounting	0	0	Open	Open
After mounting	0	0	100k	100k

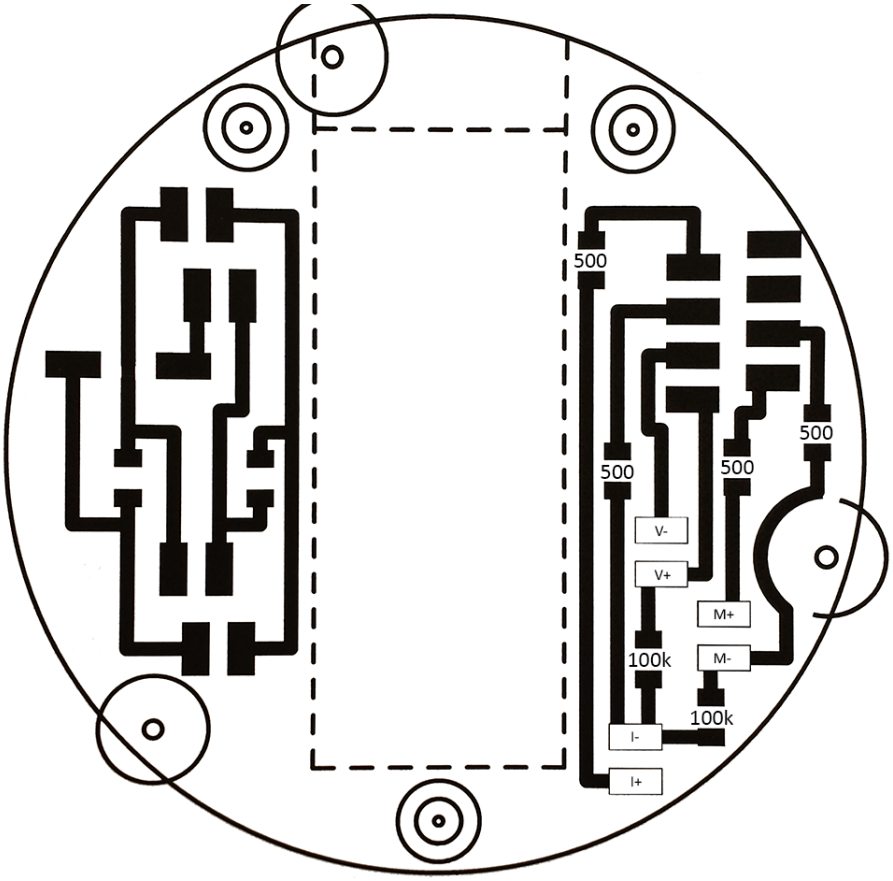

Figure A.3: Schematic of the pc board on the holder. The numbers indicate the resistance values at those locations (in Ω). The labeled rectangles are the 6 soldering points.

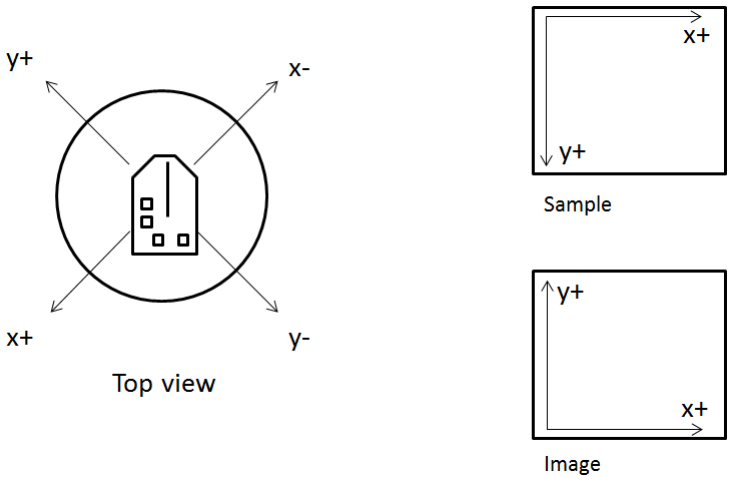

Figure A.4: Directions of the x and y-axes with respect to the setup, the sample and an image of the sample made with WINIMAGE

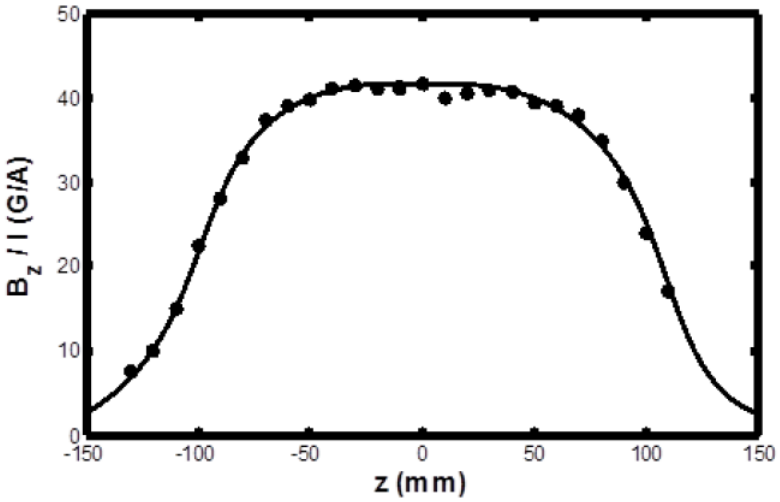

Figure A.5: Calibration graph of the magnetic field coil. Z is the position along the coil's central axis, with the center being at z=0.

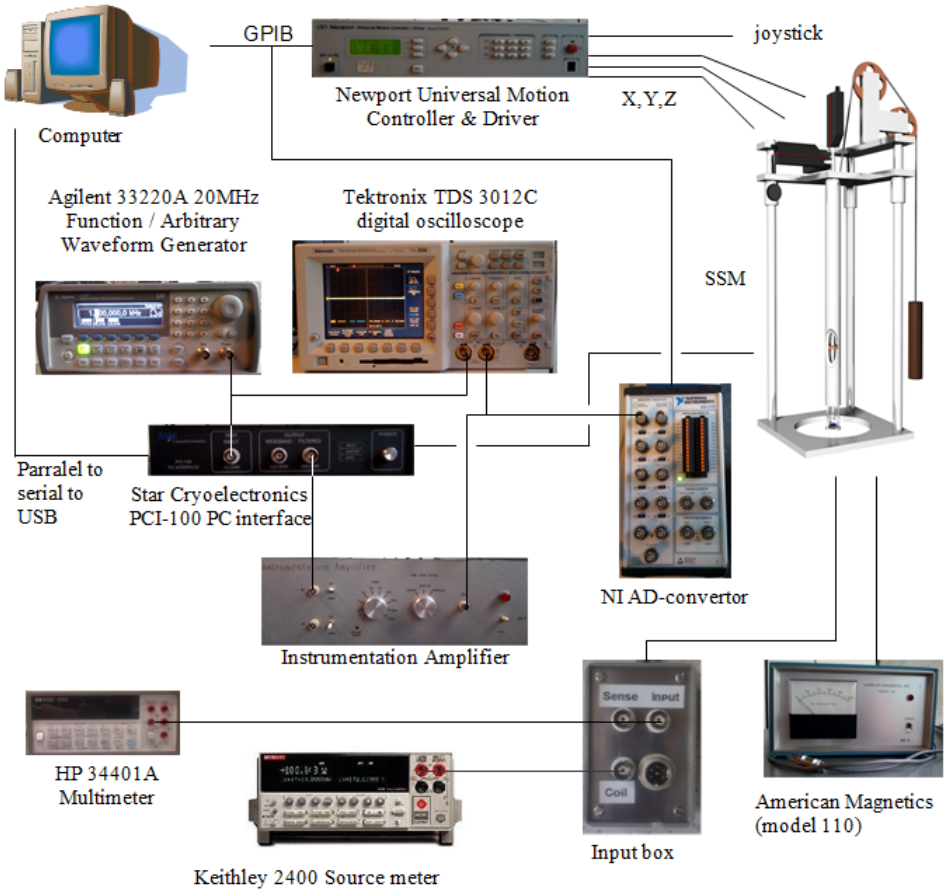

Figure A.6: Schematic of the external electronic connections

These tables describe the needed pressure to reach certain temperatures when pumping the system to go below 4.2 K, and the amount of counterweights needed to compensate for that pressure.

Counterweight #	Add at pressure (mbar)	Cumulative weight (kg)	Actual compensating pressure (mbar)
0	1000	0	0
1	1000-850	4.02	147
2	850-700	7.91	289
3	700-570	11.8	431
4	570-430	15.69	573
5	430-300	19.58	716
6	300-150	23.47	858
7	150-0	27.36	1000

Pressure (mbar)	Pressure (Torr)	Temperature (K)
1000	750	4.2
750	562.5	3.91
500	375	3.54
250	187.5	3.02
150	112.5	2.7
100	75	2.48
50	37.5	2.16
40	30	2.08
30	22.5	1.97
20	15	1.85
10	7.5	1.74